Summer 2012

Modeling, Identification, Validation and Control of a Hybrid Maglev Ball System

Ahmed Elhussein E. Mekky
Old Dominion University

MODELING, IDENTIFICATION, VALIDATION AND CONTROL OF A HYBRID MAGLEV BALL SYSTEM

by

Ahmed Elhussein E. Mekky
B.Sc. August 2007, University of Khartoum, Sudan

A Thesis Submitted to the Faculty of
Old Dominion University in Partial Fulfillment of the
Requirements for the Degree of

MASTER OF SCIENCE

AEROSPACE ENGINEERING

OLD DOMINION UNIVERSITY
August 2012

Approved by:

Thomas E. Alberts (Director)

Brett Newman (Member)

Colin Britcher (Member)

Robert L. Ash (Member)

ABSTRACT

MODELING, IDENTIFICATION, VALIDATION AND CONTROL OF A HYBRID MAGLEV BALL SYSTEM

Ahmed Elhussein E. Mekky

Old Dominion University, 2012

Director: Dr. Thomas E. Alberts

In this thesis, the electrodynamics of a single axis hybrid electromagnetic suspension Maglev system was modeled and validated by applying it to a single axis hybrid maglev ball experiment. By exploring its linearized model, it was shown that the single axis hybrid Maglev ball has inherently unstable dynamics. Three control scenarios were explored based on the linearized model; (1) Proportional, Deferential (PD) control, (2) Proportional, Deferential, Integral (PID) and (3) PID controller with pre-filtering. This thesis has shown that a PID controller with a pre-filtering technique can stabilize such a system and provide a well-controlled response.

A parametric system identification technique was applied to fit the theoretically derived model to a single axis hybrid maglev ball experiment. It is known that the identified model has different model parameters than the theoretically "derived" parameters. This thesis has examined and discussed the deviation from the theoretical model. Importantly, it was shown that such a system can be identified by estimating the values of two parameters instead of five to increase the accuracy.

A Numerical nonlinear simulation was developed for the experiment based on the theoretically derived and experimentally identified model. This simulation was validated by real-time experiment outputs.

This thesis is dedicated with love and respect to my parents and family.

ACKNOWLEDGEMENTS

I would like to thank all those who helped me directly or indirectly to accomplish this research.

Firstly, I would like to thank with gratitude and appreciation Dr. Thomas Alberts, my adviser, for his endless help, guidance and support during my research.

I would like to thank all of my professors who have prepared me for my master journey, without their teachings, it would be impossible to reach the end. I would like to specifically thank Dr. Brett Newman, Dr. Colin Britcher and Dr. Robert Ash for being my committee members and reviewing my research harvest.

I would like to thank Pierrick Bordes, Paul Leborgne and Jeremy Roadcap for their help in modifying the conventional Maglev ball experiment (electrical magnet only) to a hybrid system (contains permanent and electric magnets).

I would like to thank Mazin Abuharaz and his wife for being my family in this country and for their continual support and help. I also would like to thank my friends who have supported me and given me excessive care, while being thousands of miles apart. I would like to especially thank Suha Abbas, Ahmed Ali, Abdu-Rahman and Mohammed Fared.

Finally, I would like to acknowledge my parents, brothers, sister and my future wife Ruaa for their emotional support, endless encouragement and love. Without them I would not pass through hard times and achieve my graduate study. This thesis is dedicated to them.

NOMENCLATURE

A_g, A_p	Air gap and permanent magnet cross sectional areas, m^2
B	Magnetic flux density, $Tesla$
μ_0	Magnetic permeability of the free air, H/m
μ_p	Magnetic permeability of the permanent magnet, H/m
$\Re$	Magnetic reluctance, A-turns/Weber
Φ	Magnetic flux, Weber
H_c	Permanent magnet coercive force, A/m
l_p	Permanent magnet thickness, m
N	Number of turns of the electric coil wire, turns
$I(t)$	Excitation current, Amperes
$z(t)$	Air gap length, m
V	Volume, m^3
$F(I,z)$	Hybrid magnet attraction force, N
g	Gravitational acceleration, m/s^2
m	Suspended object mass, Kg
$v(t)$	Amplifier voltage, volts
R	Electric circuit resistance, Ohm
L	Hybrid magnet inductance, Henry
K_a	Amplifier gain, (No Units)

I_c Command current, Amperes

a_1, a_2 Permanent magnet equivalent current and reluctance, (No Units)

K_f Attraction force constant, $H.m - turn^2$

K_l Inductance constant, $H.m - turn^2$

η_ϕ Effective flux constant, (No Units)

η_g Effective gap cross sectional area, (No Units)

K_p Proportional gain, (No Units)

K_d Derivative gain, (No Units)

K_I Integral gain, (No Units)

TABLE OF CONTENTS

Page

Page

Page

Page

LIST OF FIGURES

Page

Figure

LIST OF TABLES

Page

Table

CHAPTER 1

INTRODUCTION

1.1 INTRODUCTION

Electromagnetic suspension of objects is the foundation for magnetic levitation (maglev) technology which has been shown to have promise in many applications. The origin of maglev systems traces back as far back as 1864 [1]. However, maglev suspension continues to be a challenging field of endeavor.

Maglev technology is valued or highly regarded for eliminating friction due to mechanical contact and the associated noise, decreasing maintenance costs, and achieving high-precision positioning [2]. Therefore, it is widely used in various applications, such as high-speed trains, magnetic bearings, vibration isolation systems, wind tunnel levitation and photolithography steppers [2].

Generally, maglev systems can be classified into two categories: electrodynamic suspension (EDS) and electromagnetic suspension (EMS). EDS systems are commonly known as "repulsive levitation". In those systems, magnets are used to repel the suspended object from the base as shown in Figure 1. Superconductive magnets or permanent magnets are always used as the levitation source. However, the repulsive magnetic poles of superconductive magnets cannot be reacted at low speed so that they are only suitable for long-distance and high-speed train systems [2]. EDS trains are normally equipped with wheels to carry them to the levitation speed; however, there are some proposed EDS systems that can levitate at a stand-still, such as the Korean HTSC system which levitates at zero speed by using AC superconducting magnets (as proposed to be analogous to DC magnets). Basically, the magnetic levitation force of EDS is "partially" stable and it allows large air gaps [2]. Nevertheless, the production process of superconducting magnetic materials is relatively complex and expensive [2].

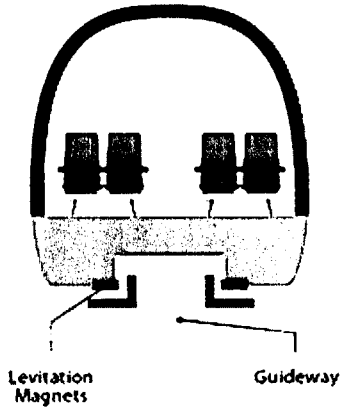

Figure 1: Electrodynamic suspension concept

On the other hand, EMS systems are commonly known as "attractive levitation". In those systems magnets are used to attract the suspended object towards the base as shown in Figure 2, and the magnetic levitation force is inherently unstable so the control problem is more challenging.

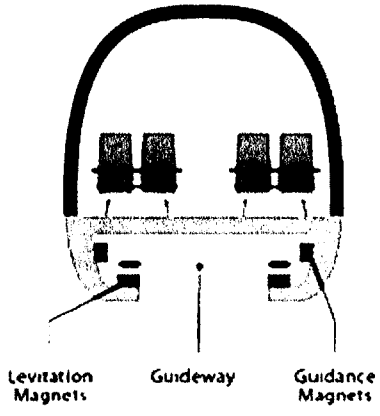

Figure 2: Electromagnetic suspension concept

Generally speaking, the manufacturing process and cost of EMS are lower than EDS, but more electric power is required to achieve the same levitation gap. In order to merge the merits of these two kinds of levitation systems, a hybrid maglev system is introduced in which a combination of an electromagnetic magnet and a permanent magnet are used [2]. The magnetic force generated by the additional permanent magnet is used to alleviate the power consumption for levitation (i.e. the levitation force is primarily produced by the permanent magnet and the electromagnet is used to control the dynamics of the suspended object about the required air gap).

Because the EMS system has inherently unstable and nonlinear behavior, it is difficult to build a precise dynamic model for it. In previous research studies, mathematical models for many kinds of hybrid maglev systems have been proposed, but there still exist uncertainties in practical applications [2-8].

In this thesis, a simple step-by-step mathematical model for the dynamics of a single axis hybrid maglev system was developed. Also, due to uncertainties associated with the parameters of the model, the derived model was identified to fit a single axis hybrid maglev ball experiment based on experimental measurements. Furthermore, a numerical nonlinear simulation for the experiment was built to validate the derived model. Moreover, some other verification strategies were provided. Given an accurate-enough model to predict the dynamic behavior of the single axis hybrid maglev ball, a control system was designed based on the linearized model. Three control scenarios were explored to find a most suitable control for this type of applications, and it was applied to the nonlinear simulation and the experiment.

In this chapter, a brief introduction of maglev technology, its types and concepts, is provided. The literature pertaining to this research is briefly discussed, focusing on EMS systems, hybrid maglev and dynamic system identification and control. The motivation for and the scope of this research are provided, and the objectives of this study are addressed.

In chapter 2, a step-by-step derivation of the dynamic model for a single axis hybrid maglev system is provided. A cylindrical hybrid magnet was used to derive the magnetic

attraction force and excitation current expressions starting from the basic laws and theories of electromagnetism.

Chapter 3 focuses on a single axis hybrid maglev ball experiment. The dynamic model derived in chapter 2 is used to identify a single axis hybrid maglev ball experiment following the parametric method for systems identification based on experimental measurements.

Chapter 4 aims to validate the identified model. A nonlinear simulation using Matlab/Simulink® software is built to simulate the single axis hybrid maglev ball experiment based on the identified model in order to check the validity of the identified model and to run tests and collect results for the system without running the actual experiment. In addition to model validation, theoretical model deviation is investigated to determine the exact reason for the differences between the identified and theoretical models.

In chapter 5, a simple control system design is provided for the single axis hybrid maglev ball experiment based on the linearized model. Taylor series expansion technique was used to linearize the dynamic model for the experiment, and Routh stability criterion was followed to design the control system. Three control scenarios have been investigated, PD, PID and PID with pre-filtering, and then, the most feasible controller is applied to the nonlinear simulation and the experiment to check the reliability of the chosen control.

In chapter 6, conclusions that can be drawn from this research work are presented. Furthermore, recommendations for future work are provided.

1.2 MAGNEMOTION INC. M3 MAGLEV

The M3 Maglev system is one of the ongoing research applications that applies hybrid maglev technology [9]. It was originally developed as part of the U.S. Urban Maglev Project as an alternative to classical urban transportation means. Development is now focused on demonstrating operation on an existing guideway at Old Dominion University. In this application, permanent magnets are used to provide most of the suspension and

guidance forces. In addition, coils wound around the magnets are excited so as to stabilize the suspension and control the air gap. Hybrid magnets are arranged along the vehicle so that it passively provides lateral guidance. The same magnetic field that produces suspension and guidance forces interacts with current in the guideway to produce propulsive force. The use of permanent magnets in M3 allows doubling the suspension gap and more than an order of magnitude reduction in onboard power requirements for suspension [9]. Currently, this vehicle is in the operation demonstration phase on the Old Dominion University guideway.

1.3 LITERATURE REVIEW

The early history of magnetism is shrouded in antiquity. The word *magnetism* is derived from the Greek word *magnes*, applied by Euripides to an iron ore (*magnetite*) that displayed a selective attraction for iron [10]. It appears, from the writings of Lucretius, that Greeks and Romans were aware that the magnetic iron ore could imbue ordinary iron in contact with it with its own peculiar property. The science of magnetism made little progress until the development of the mariner's compass, possibly invented in China in the latter part of the eleventh century. William Gilbert (c1540-1603), physician to Elizabeth I, collected in his *De Magnete (1600)* all that was then known concerning magnetism, including many of his own observations. From his observations, Gilbert inferred that the earth itself acts as a huge magnet with poles almost, but not quite, coinciding with its geographic poles [10].

The magnetic effect of an electric current was discovered in 1819 by Hans Christian Oersted (1777-1851), Danish physicist and chemist. He found that a compass needle placed under an electric current takes up a direction perpendicular to that of the current [10]. This observation, which initiated the subject of electromagnetism, was confirmed by Andre Marie Ampere (1775-1836), a French physicist and mathematician who rapidly explored, both theoretically and experimentally, many of its implications [10].

In 1864, James Clerk Maxwell published *A Dynamical Theory of the Electromagnetic Field*, in which he accomplished two formidable tasks: summarizing, in a concise

mathematical manner, the diffuse understanding of electricity and magnetism, and extending that understanding to predict the existence of electromagnetic waves that propagate through space. At the time, electrostatics and magnetostatics were more or less distinct disciplines, each with its own system of measurement and its own definitions and standards. Furthermore, the classical teachings held that electric and magnetic changes took place instantaneously at all distances, without the aid of any intervening mechanism. This referred to as Action at a Distance [11].

The relevant literature to Electromagnetic Suspension dynamics modeling and control has been studied in order to conduct this research, focusing on hybrid maglev systems. The following is a brief overview of the most related literature on the topic:

1.3.1 Electricity and Magnetism

Coren [11] provides the fundamentals of electromagnetics from an engineering perspective. In this book, he provides a simple, fundamental and logical development for electromagnetic properties (i.e. field, flux, energy, force, etc.) in a way that provides an insight into the theory without being overwhelmed by the complexity of electromagnetism details. The magnetic circuit analogy is described in a simple way in [11], which is a very useful tool to derive electromagnetic attraction force for any arrangement of magnets.

Practical issues in the use of neodymium, iron, and boron (NdFeB) permanent magnets in different applications have been provided by Marc T. Thompson [12]. In his study, he provides an analytical approximate modeling of NdFeB systems besides other practical issues concerning such magnets. The most relevant part of his work to this research study is the modeling part in which he provides a general way to develop an approximation for the magnetic flux density and the magnetic flux for NdFeB permanent magnets. He used the magnetic circuit analogy in order to develop the former properties neglecting the fringing effect and the wasted flux assuming a small gap between the magnet and the suspended object.

1.3.2 Electromagnetic Suspension

Sinha [3] provides the mathematical modeling of a one degree of freedom mass levitation system. In this book, he provides the mathematical derivation of the fundamental equations that govern the electromagnetic attraction force and the excitation current using only an electromagnet for levitation. In addition, it provides the linearization, stability analysis and control of such an EMS system.

Model realization and control of magnetic ball levitation has been studied by Omran, Hanasoge and Alberts [13]. In this work, a model, simulation and experimental validation of a magnetic ball suspension system have been provided. The nonparametric system identification method was followed to estimate the attraction force for an electromagnet of a single axis maglev ball experiment as they applied various expressions to estimate the attraction force until they finally developed a similar formula as provided in [3] to closely model the attraction force. In their study, they apply the linear least square method for parameters estimation. Furthermore, they design a simple PID controller and a gain scheduling PID controller for the system based on its linearized model.

1.3.3 Hybrid Maglev System

A new maglev system for a magnetically levitated carrier system has been presented by Mimpei, Teruo, Shuji, Noburu and Toyohiko [8]. In this paper, they introduced a zero power control system for a hybrid maglev carrier. Their main idea is to let the desired (or the command) levitation gap change in accordance with the carried load in order to maintain zero-power levitation. The command gap is specified according to the gap attraction force profile for the permanent magnet, i.e. the permanent magnet attraction force balances the carried load at the specific gap, in addition to the permanent magnet they use an electromagnet to control and maintain the stability of the maglev. In their work, they emphasized the fact that permanent magnet attractive force is inversely proportional to the gap squared, supporting that by experimental results. They generated the dynamic model for a hybrid maglev carrier, linearized the model and applied the zero power control technique to the model and an experimental system. The importance of

their work to this study comes from the detailed derivation for the system dynamics which follows the magnetic circuit analogy, the linearization and control of the hybrid maglev system. However, their derivation is somewhat complex.

Zero-power control of magnetic levitation vehicles with permanent magnets has been worked out by Chang-Hyun, Han-Wook, Jong-Min, Hyung-Suk, Bong-Seup and Dong-Sung and presented in the International Conference on Control, Automation and Systems 2010 [5]. In their work, they mainly carried out the notion that had been previously proposed in [8] and applied it to a hybrid maglev tester. They developed the attraction force for the hybrid magnet by simply adding the permanent and the electromagnet attraction force expressions, i.e. they developed the attraction force for an electromagnet without the presence of the permanent magnet and derived the attraction force for the latter in the absence of the former and added the two expressions to represent the attraction force for the hybrid magnet that contains both electrical and permanent magnets. The expression produced following this method of derivation is invalid for negative current. They linearized the hybrid maglev system and designed a feedback control for an experiment besides building a simulation and providing some simulated results.

A study for a simple controlled permanent magnet suspension system has been done by David L. Atherton [14]. In this paper, the lift, current and dissipated power for a block of permanent magnets between two thin iron pole pieces around which the inductor is wound have been provided. He derived the attraction force for the hybrid magnet considering only the air gap reluctance and neglected the fringing effect; therefore he calls it the "best case" model. He proves that the use of a different variety of permanent magnets on maglev systems can substantially improve the potential performance of the systems; however, he added that the use of very small control powers may severely limit the stable dynamic operating range. This paper gives an insight on the derivation of the attractive force for hybrid maglev systems.

A model of a U-shape hybrid maglev system using permanent and electromagnets has been identified by Xiao Zhung [4]. In this paper, the magnetic force and the excitation

current expressions derived in [3] have been provided with some modification to govern the dynamical behavior of hybrid maglev systems and the parameters of the expressions have been identified experimentally. He follows the parametric systems identification method using the linear Least Square estimation method for an experimentally collected data from a hybrid maglev system. However, he identifies a simple linear model for the excitation current in his work to minimize the complexity of the hybrid maglev system identification process. The identification signal used by [4] covers only a range of almost 0.6 mm using five sinusoidal signals added to each other as the identification signal. Furthermore, he does not provide sufficient validation to the identified model.

A linear feedback control for a hybrid maglev system is worked out by Liming Shi and Haibo Zhang [7]. In their study, they represent a model for a hybrid maglev system including the dynamical model and the electrical model. In addition, they provide a design for state feedback control for the system based on the linearized model. Furthermore, they applied the designed control system to an experimental hybrid maglev vehicle for validation.

1.3.4 Dynamical Systems Identification

P.P.J. van den Bosch and A. C. van der Klauw provide a very systematic method of systems identification in their book Modeling, Identification and Simulation of Dynamical System [15]. In their book, they give an in-depth introduction on the fields of modeling, identification, simulation and optimization. They classified modeling of dynamical system into three categories, i.e. the white, black-box and gray systems modeling. White models can be derived from prior knowledge of the physical behavior of the system, i.e. developed based on the physical, electro-technical, mechanical or chemical laws that describe the dynamical behavior among the variables of the system. If insufficient knowledge is present, a model can be built based on measurements of the system and in such a case the model is called black-box modeling. Gray modeling is an intermediate grade between white and black-box modeling, i.e. prior knowledge of physical laws covers only part of the dynamical relations of the system and other relations are obtained based on system measurements.

Two types of parameter estimation were given in [15]: parametric and nonparametric system identification methods. The parametric type is applied to white and gray models and the nonparametric type is followed for black-box systems, embedded in each system identification type there are many parameter estimation methods. The importance of model validation is emphasized in [15] and some general ways for model validation are presented. Dynamical systems simulation is discussed in a separate chapter; however, for this thesis, prior knowledge is used to simulate the single axis hybrid maglev ball experiment.

1.3.5 Dynamical Systems Control

Ogata [16] provides a very comprehensive treatment of the analysis and design of control systems. This book covers a wide range of control systems analysis in both theoretical and numerical aspects. For this thesis, only the Routh stability criterion discussed in chapter five of [16] is followed to design the control system for the single axis hybrid maglev ball experiment. Furthermore, this book provides a deep insight into the consequences of applying different control scenarios, which was found very useful for the controller design phase of this study.

1.4 MOTIVATION AND SCOPE

Upon reviewing the literature relevant to this research, it can be seen that many references provide dynamical models for the single axis hybrid maglev system; however, the attractive force expressions are not consistent and, in addition, some of the references over-simplify the model in order to reduce the complexity of the dynamical analysis and the control design for the system. As a result, extra adjustment is required to cover the dynamics deviations between the theoretical model and the actual system. In this thesis, a step by step derivation for a single axis hybrid maglev system is worked out and the nonlinear dynamical model is identified to produce as close a model as possible to the real application.

Some of the reviewed studies follow the nonparametric identification method to come up with a valid and satisfactory model for conventional maglev systems, i.e. using

only electromagnets for levitation; however, this method for identification is more time-consuming and less insightful on the physical significance of the model compared to the parametric method for system identification. Therefore, for system identification the parametric systems identification method is followed to model the single axis hybrid maglev ball in this research.

Most of the reviewed literature avoids or does not provide a rigorous validation of the provided model by comparing experimental and simulated results. Consequently, when they design the control system based on the provided model and apply the controller to the real system, they come up with different results than they expected. Here, a rigorous validation is made for the derived model by providing experimental results alongside the simulation results. Furthermore, the designed control based on the model is applied directly to the experiment and the nonlinear simulation without adjustments and the results are represented in an overlay fashion.

As mentioned previously, EMS systems are essentially unstable and, as a result, designing a control system is a substantial issue for those systems. Most of the reviewed studies on the control of hybrid maglev systems use a state feedback control method which requires the availability of all the states for control. However, in this study, a simple PID with pre-filter is found quite satisfactory for such an application.

CHAPTER 2

HYBRID ELECTRO-MAGNETIC FORCE AND EXCITATION CURRENT MODELING

2.1 INTRODUCTION

Modeling is the art of creating mathematical descriptions of physical, chemical or electrotechnical phenomena. These descriptions have to be relatively simple, yet accurate enough to serve the purpose of the modeler (Kheir, 1990) [15].

In this chapter, mathematical models for the attraction force and the excitation current for a single axis hybrid magnetic levitation system are developed in detail. Although some of the references provided models for such systems, the models are not consistent nor are they supported by detailed derivation.

Electromagnetism is a complex field of study, and it is associated with uncertainties and nonlinearities; however, in this chapter, a simple approach to estimate the magnetic attraction force for a single axis hybrid magnetic levitation is developed.

2.2 THEORETICAL MODELING

Hybrid magnets consist of an electromagnet and a permanent magnet to provide the levitation force for the suspended object. The suspension force is primarily provided by the permanent magnet; however, its magnetic flux is not controlled. Therefore, the electric magnet is used to control the dynamics of the suspended object about the desired levitation gap.

Generally, the magnetic attraction force depends directly on the produced magnetic flux density; consequently, to estimate the magnetic attraction force for hybrid magnets, the magnetic flux density for hybrid magnets should be estimated first.

The excitation current model for the single axis hybrid maglev system is derived to account for the presence of the permanent magnet. The effect of the permanent magnet on

the electrical circuit appears in the induced electrical potential due to the rate of change of the magnetic inductance and the excitation current.

2.2.1 Magnetic Flux Density For Permanent Magnets

Rough order-of-magnitude modeling of the amplitude of the magnetic field produced by a high-strength permanent magnet can be done by using magnetic circuit modeling in cases where air gaps are relatively small [12]. Using magnetic circuit modeling, magnetomotive force (MMF) is analogous to voltage, flux (Φ) is analogous to current, and the proportionality constant relating MMF and flux is magnetic reluctance. The magnetic circuit model of a permanent magnet of length (l_m) and cross-sectional area (A_m) is shown in Figure 3 below. The MMF source is ($H_c l_m$), where (H_c) is the coercive force of the magnet. The magnetic reluctance ($\Re_m$) inside the magnet is given by [12]:

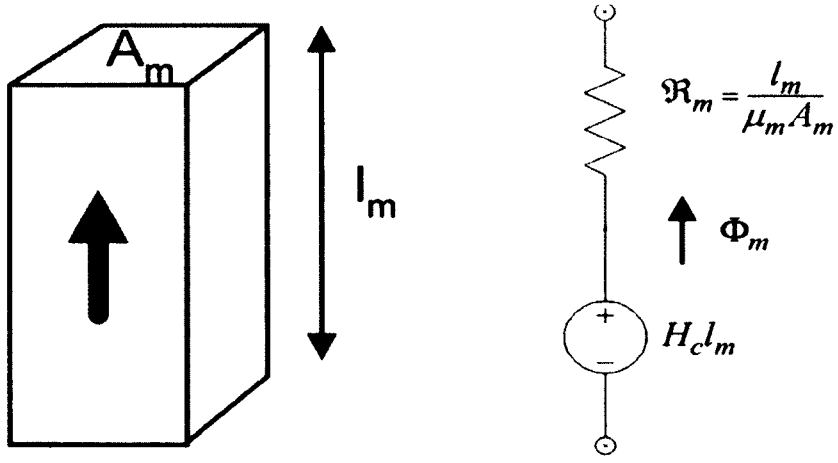

Figure 3: Magnetic circuit model for the permanent magnet

$$\Re_m = \frac{l_m}{\mu_m A_m} \qquad (2-1)$$

where μ_m is the permanent magnet permeability. In general, the magnetic reluctance may be expressed as follows:

$$\Re = \frac{Path\ length}{(\mu)(Cross - sectional\ area)} \qquad (2-2)$$

The magnetic flux (Φ_m) and the air gap flux density(B_m)for the permanent magnet can be approximated as follows:

$$\Phi_m \approx \frac{H_c l_m}{\sum \Re} \qquad (2-3)$$

$$B_m \approx \frac{\Phi_m}{A_g} \qquad (2-4)$$

where A_g represents the air gap cross-sectional area. This approximation method ignores the leakage flux and the three-dimensional end effects, i.e. assuming a uniform flux, but is useful for a rough estimation of flux density [12].

2.2.2 Magnetic Flux Density For Electromagnets

MMF for electromagnets is found by $NI(t)$ [3], accordingly, the same analogy used for the permanent magnet can be used to approximate the flux density (Φ_e) and the air gap flux (B_e) for the electromagnet as follows [3]:

$$\Phi_e \approx \frac{NI(t)}{\sum \Re} \qquad (2-5)$$

$$B_e \approx \frac{\Phi_e}{A_g} \qquad (2-6)$$

where N is the number of turns of the electrical coil and $I(t)$ is the instantaneous current that passes through the coil and generates the magnetic flux.

2.2.3 Attraction Force For Single Axis Hybrid Magnets

Starting with Maxwell-Faraday's law that relates electrical and magnetic fields, i.e. the curl of the magnetic field vector $\boldsymbol{E}$ is equal to the negative rate of change of the corresponding magnetic flux vector, as follows:

$$\nabla \times \boldsymbol{E} = -\frac{\partial \boldsymbol{B}}{\partial t} \qquad (2-7)$$

Applying Stokes's theorem [11] to equation $(2-7)$ yields:

$$\int (\nabla \times \boldsymbol{E}).\boldsymbol{n}ds = \oint \boldsymbol{E}.\boldsymbol{\tau}dl = -\frac{\partial}{\partial t}\int \boldsymbol{B}.\boldsymbol{n}ds \qquad (2-8)$$

where $\boldsymbol{\tau}$ is a unit vector tangent to the path l -that bounds the surface area S -at each point, and $\boldsymbol{n}$ represents the normal unit vector to the surface area S.

The term on the middle of equation $(2-8)$ is the line integral of $\boldsymbol{E}$ which represents the voltage, or energy per unit charge, or the potential change between the limits of the integral[11]; accordingly, equation $(2-8)$ can be written as:

$$v = -\frac{d}{dt}\left(\int \boldsymbol{B}.\boldsymbol{n}ds\right) \qquad (2-9)$$

The field strength within a long solenoid shown in Figure 4 is given by [11]:

$$H = nI = \frac{N}{l}I \qquad (2-10)$$

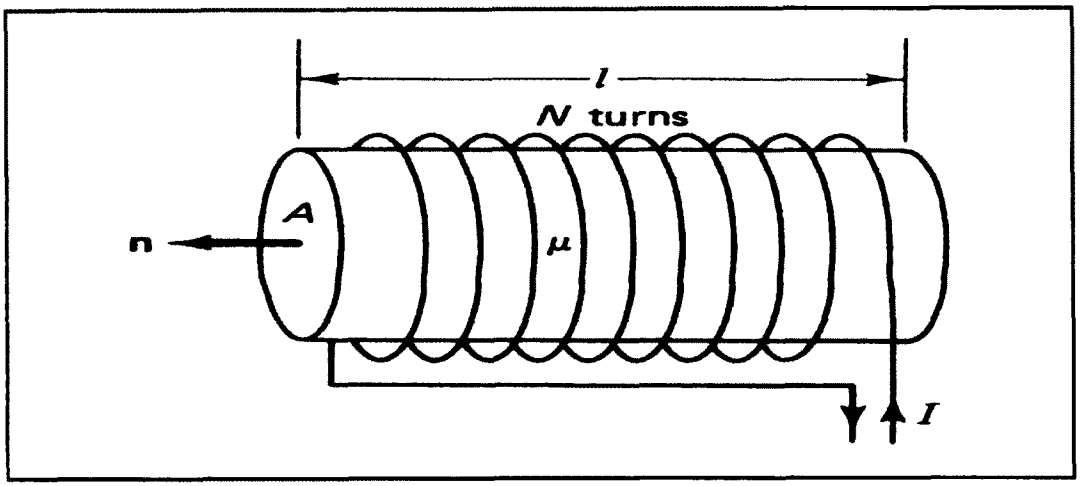

Figure 4: Long solenoid (electromagnet)

In increasing this current from zero to its final value necessary for the specific H field, the changing flux induces an opposing Electromotive Force (EMF) according to the Faraday-Lenz law, which must be overcome. By considering only the magnitude, from equations $(2-8)$ and $(2-9)$:

$$v = N\frac{d}{dt}(BA) = NA\frac{dB}{dt} \qquad (2-11)$$

The factor N in this expression is due to the fact that Faraday's law describes the voltage generated in a single loop. If N turns are in series, the total voltage is the sum of their individual voltages.

From equations $(2-10)$ and $(2-11)$, the power expended by the current source is [11]:

$$P = \frac{dW}{dt} = vI = NA\frac{dB}{dt}.\frac{Hl}{N} = VH\frac{dB}{dt} \qquad (2-12)$$

since the volume enclosed by the windings is $V = Al$. It follows that the rate of change of magnetic energy density, $U_m = W/V$, is:

$$\frac{dU_m}{dt} = \boldsymbol{H}.\frac{d\boldsymbol{B}}{dt} \qquad (2-13)$$

In the linear case, $\boldsymbol{B} = \mu\boldsymbol{H}$, so equation (2-13) can be written as follows:

$$\frac{dU_m}{dt} = \mu\boldsymbol{H}.\frac{d\boldsymbol{H}}{dt} = \frac{d}{dt}\left(\frac{1}{2}\mu H^2\right) \qquad (2-14)$$

Integrating equation $(2-14)$ with respect to time yields the magnetic energy density:

$$U_m = \frac{1}{2}\mu H^2 = \frac{1}{2}\boldsymbol{H}.\boldsymbol{B} \qquad (2-15)$$

Integrating this magnetic energy density, equation $(2-15)$, over a volume containing a magnetic field gives the total magnetic energy in the volume.

$$W = \int \frac{1}{2} \boldsymbol{H}.\boldsymbol{B} dV = \frac{1}{2} \boldsymbol{H}.\boldsymbol{B} V \qquad (2-16)$$

In the case of a magnetic circuit collection, this integral becomes a sum over the various circuit component volumes:

$$W = \frac{1}{2} \sum \boldsymbol{H}_i.\boldsymbol{B}_i V_i \qquad (2-17)$$

When the parameters change in a magnetic circuit, there is an energy change, and, as a result, the constraining force, F_x, which opposes the change of the circuit parameter x is given by:

$$F_x = \frac{dW}{dx} = \frac{1}{2} \frac{d\boldsymbol{H}.\boldsymbol{B} V}{dx} \qquad (2-18)$$

If the changing parameter is the distance, as in our case, equation $(2-18)$ becomes:

$$F_l = \frac{1}{2} \frac{d\boldsymbol{H}.\boldsymbol{B} V}{dl} = \frac{1}{2} \boldsymbol{H}.\boldsymbol{B} A = \frac{1}{2} \frac{B^2 A}{\mu} \qquad (2-19)$$

where A is the cross-sectional area that the magnetic flux passes through normally, and μ denotes the magnetic permeability of the medium.

Accordingly, for single axis hybrid magnets, i.e. the changing parameter in the magnetic circuit is the air gap, the magnetic attraction force at any instant of time is given by [3, 11]:

$$F(I, z) = \frac{B^2 A_g}{2\mu_0} \qquad (2-20)$$

where B is the overall air gap flux, A_g is the air gap cross-sectional area and μ_0 is the air magnetic permeability.

For the experiment configuration in which the permanent magnet is placed in the iron core of the electromagnet as shown in Figure 5, the attraction force is derived using the equations developed previously in this chapter as follows:

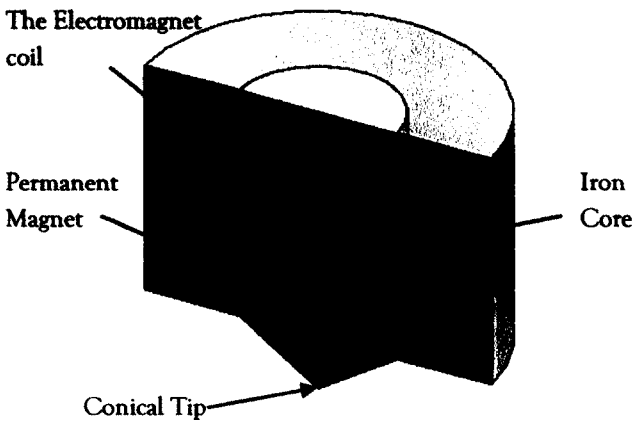

Figure 5: Electrical and permanent magnets arrangement for the study system

For the permanent magnet:

$$\sum \Re = \Re_p + \Re_g = \frac{l_p}{\mu_p A_p} + \frac{z}{\mu_0 A_g} = \frac{1}{A_g \mu_0}\left(\frac{A_g \mu_0 l_p}{A_p \mu_p} + z\right) \qquad (2-21)$$

$$\Phi_p \approx \frac{A_g \mu_0 H_c l_p}{\left(\frac{A_g \mu_0 l_p}{A_p \mu_p} + z\right)} \qquad (2-22)$$

$$B_p \approx \frac{A_g \mu_0 H_c l_p}{A_g\left(\frac{A_g \mu_0 l_p}{A_p \mu_p} + z\right)} = \frac{\mu_0 H_c l_p}{\left(\frac{A_g \mu_0 l_p}{A_p \mu_p} + z\right)} \qquad (2-23)$$

Here z is the air gap length and the subscript (p) is used to refer to the permanent magnet. In this configuration, cross-sectional areas for the permanent magnet (A_p) and the

air gap (A_g) appear to be equal as shown in Figure 5 ; however, because of the effect of conical tip, as will be discussed in Chapter 4, they cannot be equated [13].

For the electromagnet:

$$\sum \Re = \Re_p + \Re_g = \frac{l_p}{\mu_p A_p} + \frac{z}{\mu_0 A_g} = \frac{1}{A_g \mu_0}\left(\frac{A_g \mu_0 l_p}{A_p \mu_p} + z\right) \qquad (2-24)$$

$$\Phi_e \approx \frac{A_g \mu_0 N I(t)}{\left(\frac{A_g \mu_0 l_p}{A_p \mu_p} + z\right)} \qquad (2-25)$$

$$B_e \approx \frac{A_g \mu_0 N I(t)}{A_g\left(\frac{A_g \mu_0 l_p}{A_p \mu_p} + z\right)} = \frac{\mu_0 N I(t)}{\left(\frac{A_g \mu_0 l_p}{A_p \mu_p} + z\right)} \qquad (2-26)$$

Now, the overall flux density which is produced by the hybrid magnet in the air gap is given by:

$$B = B_e + B_p = \frac{\mu_0 N I(t)}{\left(\frac{A_g \mu_0 l_p}{A_p \mu_p} + z\right)} + \frac{\mu_0 H_c l_p}{\left(\frac{A_g \mu_0 l_p}{A_p \mu_p} + z\right)} = \frac{\mu_0 N\left(\frac{H_c l_p}{N} + I(t)\right)}{\left(\frac{A_g \mu_0 l_p}{A_p \mu_p} + z\right)} \qquad (2-27)$$

Then the attraction force for the hybrid magnet is found by substituting equation $(2-27)$ into equation $(2-20)$ as follows:

$$F(I,z) = \left[\frac{\mu_0 N\left(\frac{H_c l_p}{N} + I(t)\right)}{\left(\frac{A_g \mu_0 l_p}{A_p \mu_p} + z\right)}\right]^2 \frac{A_g}{2\mu_0} = \frac{\mu_0 A_g N^2}{2}\left[\frac{\left(\frac{H_c l_p}{N} + I(t)\right)}{\left(\frac{A_g \mu_0 l_p}{A_p \mu_p} + z\right)}\right]^2 \qquad (2-28)$$

Equation $(2-28)$ is very similar to the expression for the attraction force using only the electromagnet assuming that the electrical current passing through the coil is a combination of a constant current (representing the permanent magnet) and a time varying current (representing the electromagnet). Following this methodology, it is convenient to express the attraction force for the hybrid magnet as [7]:

$$F(I,z) = \frac{\mu_0 A_g N^2}{2}\left[\frac{I_{eq}}{z_{eq}}\right]^2 \qquad (2-29)$$

where I_{eq} is the equivalent current that produces the overall magnetic flux, and z_{eq} is the equivalent air gap.

Notice that the reluctance of the air gap between the suspended object and the top pole of the hybrid magnet was not modeled since it is classified as big air gaps reluctance and it is very complex to derive its expression. However, the purpose of this derivation was to develop a mathematical structure that can be identified to fit the actual system. Therefore, identification process will correct this expression to encounter for that reluctance.

2.2.4 Electrodynamics Modeling

The electrical model for the electrical circuit consisting of an inductance and resistance, as shown in Figure 6, has already been provided by [3], but it has been derived for single axis maglev system using only an electromagnet. However, it can be adjusted to govern the hybrid system as follows.

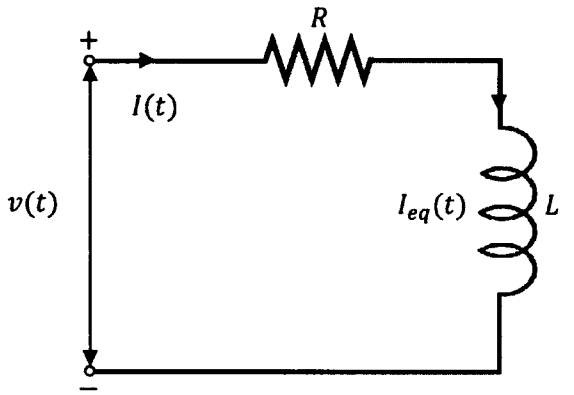

Figure 6: Electrical circuit model for the hybrid magnet

Applying Kirchhoff's law to the electrical circuit shown in Figure 6, the instantaneous voltage across the magnet winding $v(t)$ is given by:

$$v(t) = RI(t) + \frac{d}{dt}\left[L(z_{eq}, I_{eq})I_{eq}(t)\right] \qquad (2-30)$$

where R is the total resistance of the inductor, and $L(z_{eq}, I_{eq})$ is the hybrid magnet inductance as a function of the equivalent air gap and the equivalent current. The current amplifier is modeled simply as constant gain (K_a) with the current feedback loop as follows:

$$v(t) = K_a(I_c - I) \qquad (2-31)$$

The second term on the right hand side of equation $(2-30)$ can be expanded as follows:

$$\frac{d}{dt}\left[L(z_{eq}, I_{eq})I_{eq}(t)\right] = I_{eq}(t)\frac{d}{dt}\left[L(z_{eq}, I_{eq})\right] + L(z_{eq}, I_{eq})\frac{d}{dt}\left[I_{eq}(t)\right] \qquad (2-32)$$

The equivalent current (I_{eq}) is the sum of two currents (I_p) which is constant and a time varying current (I). Therefore, the time derivative of the equivalent current is simply the time derivative of the instantaneous current as shown below:

$$\frac{d}{dt}\left[I_{eq}(t)\right] = \dot{I}(t) \qquad (2-33)$$

The magnetic inductance for the single axis hybrid magnet is derived as shown in the following steps [3, 11]:

According to Lenz-Faraday's law, the voltage induced by the changing magnetic field is given by [11]:

$$v_L = -N\frac{d\Phi}{dt} = -\frac{dLI}{dt} \qquad (2-34)$$

Applying the chain rule to equation $(2-34)$ yields:

$$N\frac{d\Phi}{dt} = N\frac{d\Phi}{dLI} * \frac{dLI}{dt} = \frac{dLI}{dt} \qquad (2-35)$$

Equating the middle and the right terms on equation $(2-35)$:

$$N\frac{d\Phi}{dLI} = 1 \Rightarrow Nd\Phi = dLI \qquad (2-36)$$

Integrating both sides of equation $(2-36)$ and solving the resulting equation for L produces:

$$L(z_{eq}, I_{eq}) = \frac{N}{I_{eq}}\Phi_T \qquad (2-37)$$

where $\Phi_T = \Phi_p + \Phi_e$ is the total magnetic flux. The reluctance of the iron core is assumed to be negligible compared with the reluctance of the air gap [3]. Substituting equations $(2-3)$ and $(2-5)$ into $(2-37)$ to produce the inductance of the hybrid magnet:

$$L(z_{eq}, I_{eq}) = \frac{N^2 A\mu_0}{I_{eq}}\left[\frac{\frac{H_c l_p}{N} + I(t)}{\left(\frac{A_g \mu_0 l_p}{A_p \mu_p} + z\right)}\right] = \frac{\mu_0 N^2 A_g}{z_{eq}} = L(z_{eq}) \qquad (2-38)$$

Then, applying the chain rule to equation $(2-38)$, the first time derivative of the magnetic inductance can be expressed as follows:

$$\frac{d}{dt}[L(z_{eq})] = \frac{\delta L(z_{eq}, I_{eq})}{\delta z}\frac{\delta z}{\delta t} = -\frac{\mu_0 N^2 A_g}{z_{eq}^2}\dot{z} \qquad (2-39)$$

where $\dot{z}$ is the first time derivative of the displacement. Equations $(2-31)$ through $(2-39)$ are substituted into $(2-30)$ so that the electrodynamic model for the hybrid system become as follows:

$$K_a(I_c - I) = RI(t) + \dot{I}(t)\frac{\mu_0 N^2 A_g}{z_{eq}} - I_{equ.}(t)\frac{\mu_0 N^2 A_g \dot{z}}{z_{eq}^2} \qquad (2-40)$$

Equation (2 – 40) describes the electrodynamic behavior of a single axis hybrid maglev system. It can be noticed that equation (2 – 40) is similar to the electrodynamic model for the conventional maglev system (using only an electromagnet for levitation) provided by Sinha [3] except for the inductance voltage terms, which have been affected by the presence of the permanent magnet in the electrical circuit.

CHAPTER 3

SINGLE AXIS HYBRID MAGLEV BALL SYSTEM IDENTIFICATION

3.1 INTRODUCTION

The construction of a valuable model requires a thorough understanding of the process under study and, additionally, of modeling techniques. The modeling process consists of several consecutive steps, as illustrated in Figure 7.

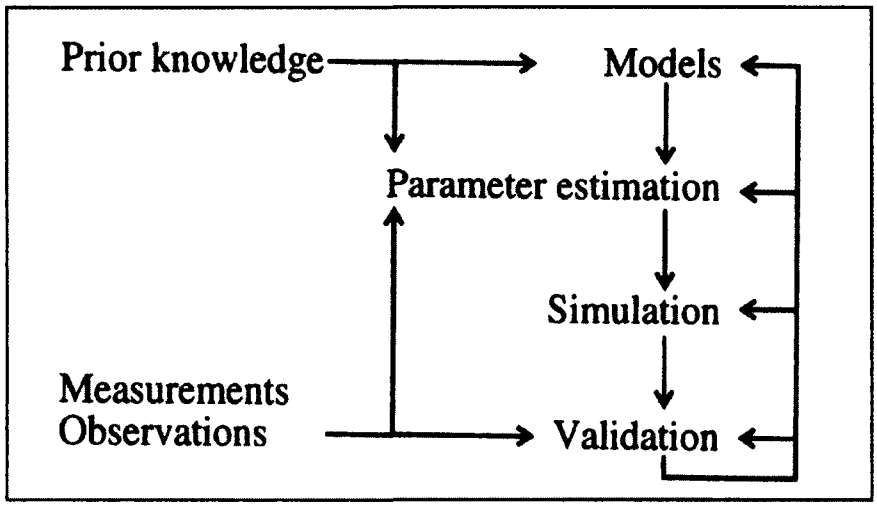

Figure 7: Modeling, parameter estimation and simulation process

Generally, there are two model identification methods: the nonparametric and the parametric identification methods. The nonparametric method identifies the system only based on its inputs and the corresponding outputs; this type of modeling is employed when there is not enough knowledge about the mathematical models to describe the behavior of the process. The parametric method identifies the system, based on a model structure derived from the theory, and the parameters in the structure are obtained based on the inputs and outputs for the actual system. In this study, the parametric method was

employed, assuming that sufficient knowledge related to the mathematical formulation was available to describe the system behavior.

The "qualitative" model represented by equations $(2-29)$ and $(2-40)$, which was derived in Chapter 2, is used to describe the dynamic characteristics of the process. Such a model describes the relations between physical quantities of the hybrid electromagnetic attraction force on a suspended object as a function of the excitation current and the suspended object position. Usually, a "quantitative" model is required. However, generally, the nonlinearities and uncertainties associated with these quantitative variables limit our ability to come up with an accurate quantitative model by directly applying the qualitative model. Consequently, parameter estimation schemes have to be used to obtain proper values for model parameters.

There are two main bases for the deviation of the actual single axis hybrid maglev ball system from the theoretical equations. These are the relatively wide operational air gap, which leads to a considerable fringing effect, and the conical shape of the hybrid magnet core tip, which leads to considerable magnetic flux leakage.

An experiment using the actual system was executed to generate the raw data for the identification using a suitable input signal which is one of the main factors that affect the identification accuracy. The linear Least-Square method is implemented to estimate the unknown parameter.

3.2 EXPERIMENTAL SETUP

The single axis hybrid maglev ball experiment consists of a copper coil that has 493 turns, a cylindrical piece of a neodymium-iron-boron (Nd-Fe-B) permanent magnet with a 1 in $(0.0254$ m$)$ thickness and a 3 in $(0.0762$ m$)$ diameter was placed inside an iron cylinder with a conical tip as shown in Figure 8. The iron piece with the permanent magnet was fitted and fastened inside the coil to form a hybrid magnet when the current passes through the copper coil. The current is sent into the coil through a Pulse Width Modulated (PWM) power amplifier. The object to be suspended is a steel ball with diameter of $0.0635\ m$. Attached to the ball there is an aluminum leg with a target at its

end, to be located using a laser sensor to determine the position of the ball. The weight of the suspended object is $1.1\ kg$. A combination of two sensors was used to determine the position of the ball because of the wide operating gap; both sensors were laser based position sensors (Sunx LA 511 and L-Gage). A switching algorithm was developed to switch the imported reading between the sensors to cover the operating air gap.

An 8-pole Butterworth filter is used for anti-aliasing, and a digital low-pass filter incorporated in the control code is used to filter the noise in the position signal. A National Instruments data acquisition card is connected to a PC104-Plus computer, both of which are used for data acquisition and control. The data acquisition system is operated through Matlab/Simulink ®, using the xPC target environment. The sample rate is 14 kHz.

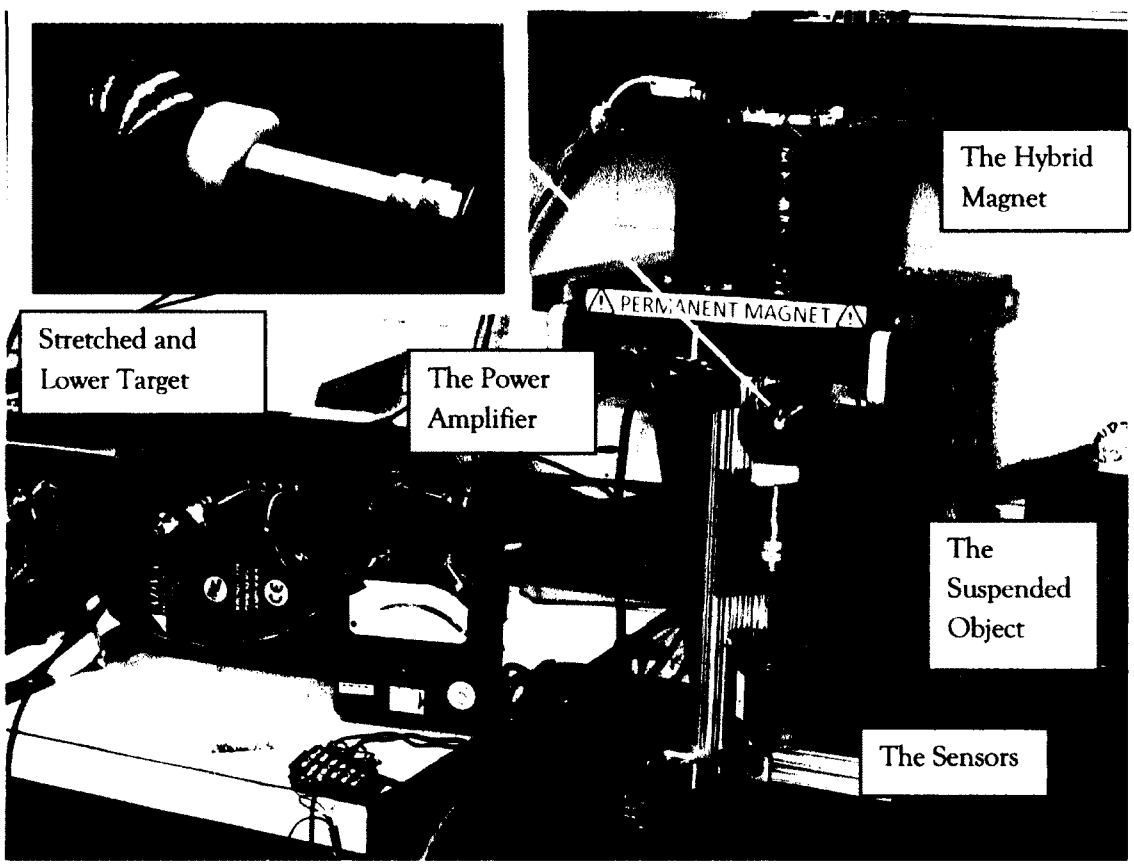

Figure 8: Experimental set up

3.2.1 The Permanent Magnet

The permanent magnet is a neodymium-iron-boron (NdFeB) material, which is an important component of powerful contemporary magnets. Neodymium is element number 60 on the periodic table, one of the so-called "rare earth" elements [17]. Neodymium itself actually is not very rare and is more plentiful in the earth's surface than more familiar elements such as lead and tin. However, it is relatively difficult to separate from its ore, making it fairly expensive [17].

This type of magnet was first introduced in 1983 as a new generation of rare-earth magnets by Sumitomo Special Metals and General Motors [12]. Throughout the years, significant improvements have been made in the magnetic strength and thermal stability of these permanent magnet materials [12], opening up new applications in large-scale systems such as motors, bearings, maglev and eddy-current brakes as well as other transportation applications such as hybrid vehicles. The reasons behind its widespread use are its large attraction force, thermal stability and resistance to demagnetization.

The permanent magnet has the following approximate physical properties:

Table 1: Physical properties of the NdFeB magnet

Property	Description	value
H_c	Coercive Force	$873.344 * 10^3\ A/m$
B_r	Remenant Magnetic Flux Density	$1.253\ T$
ρ	Density	$7400\ m^3$
μ_r	Relative Recoil Permeability	1.05

The magnetic flux density of the permanent magnet used, while it is assembled inside the electrical coil, was measured experimentally throughout the operating gap and the attraction force was estimated using equation $(2-7)$ as shown in Figures 9 and 10:

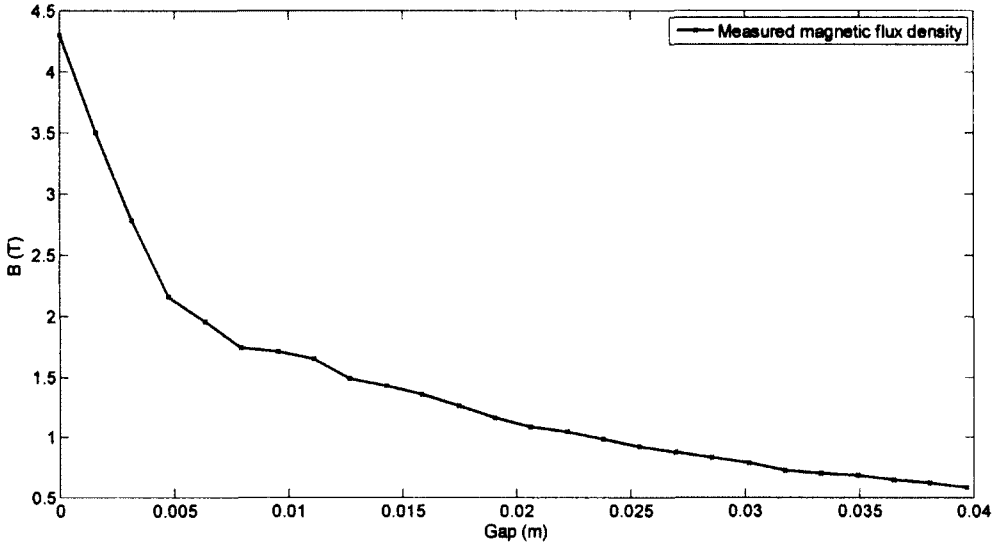

Figure 9: Measured magnetic flux density for the permanent magnet vs. air gap

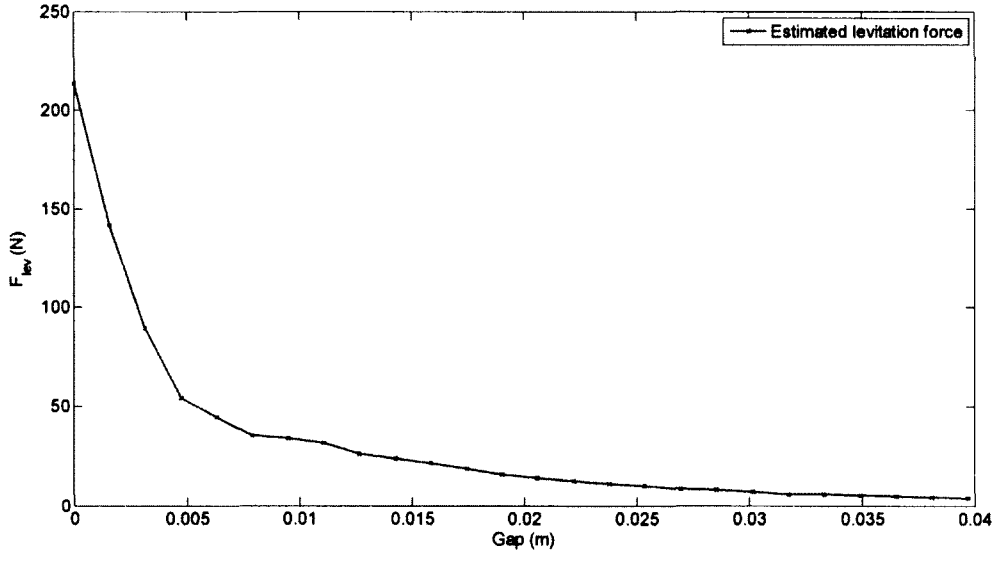

Figure 10: Calculated levitation force for the permanent magnet vs. air gap

Upon placing the permanent magnet in the system, a constant current was sent to the electrical coil to make sure that the polarity of the permanent and electromagnets agrees, and it was found that they do not agree due to the direction of the applied current;

consequently, the electrical input to the coil was reversed, i.e. the negative output from the Power Amplifier was connected to the positive side of the coil wire, which lead to a reverse current through the coil. This modification will require some changes in equation (2 – 40) when applied to the electrical circuit.

3.2.2 Sensors Switching Algorithm

To increase the operating gap for the experiment as a requirement of the permanent magnet addition, two laser based sensors are used, one of them senses the upper surface of the ball and the other senses the lower target of the leg. To guarantee a smooth switching between the sensors, a switching algorithm was implemented in the operating module in MatLab ® using Simulink xPC Target (as shown in Figure 11).

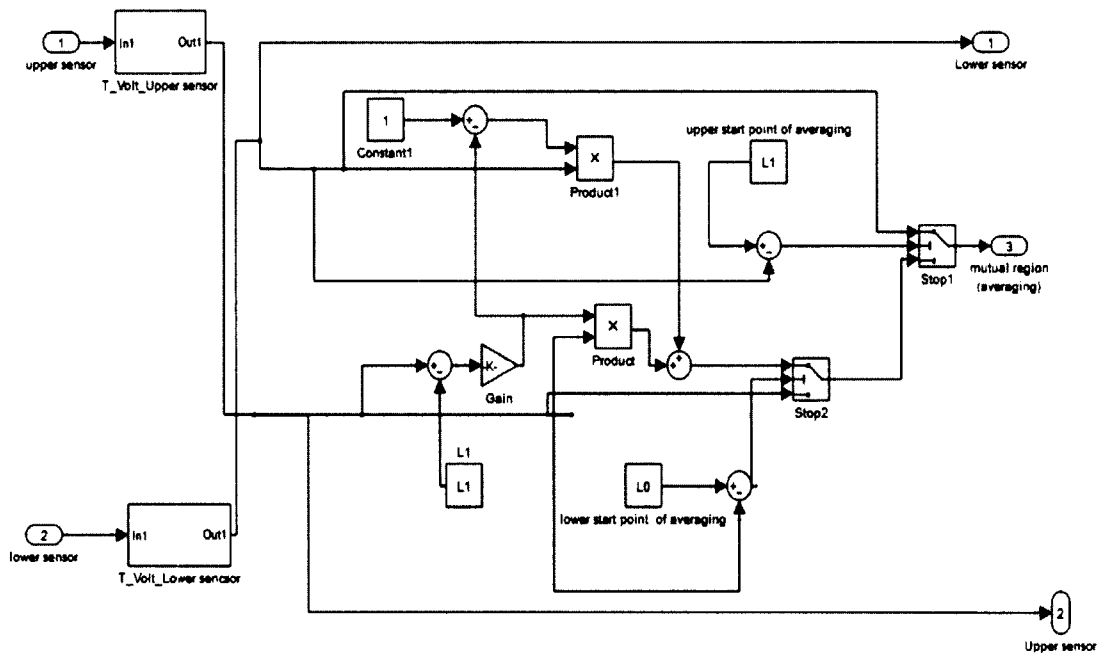

Figure 11: Simulink ® model of the sensors switching algorithm

The algorithm applies a weighted average in the mutual region and gradually switches between the sensors to become fully targeted by the lower sensor when the object is out of range of the upper sensor and vice versa. The mutual region is adjusted carefully to avoid blind spots and to achieve smooth operation.

3.3 MODEL IDENTIFICATION

The parametric system identification process begins by forming the model structure. Equations $(2-29)$ and $(2-40)$ that were derived in Chapter 2 will be used to describe the system's dynamic behavior. The iron core tip of the hybrid electromagnet was designed to have a conical shape so that the contours of the magnetic flux, shown in Figure 12 between the sphere and the cone lead to more lateral stability. However, this pattern of the magnetic flux violates the assumptions that are considered to derive the dynamical equations (uniform flux and no fringing effect). As a result, the theoretical equations cannot be applied to the system directly and it would be simpler to identify them experimentally [13].

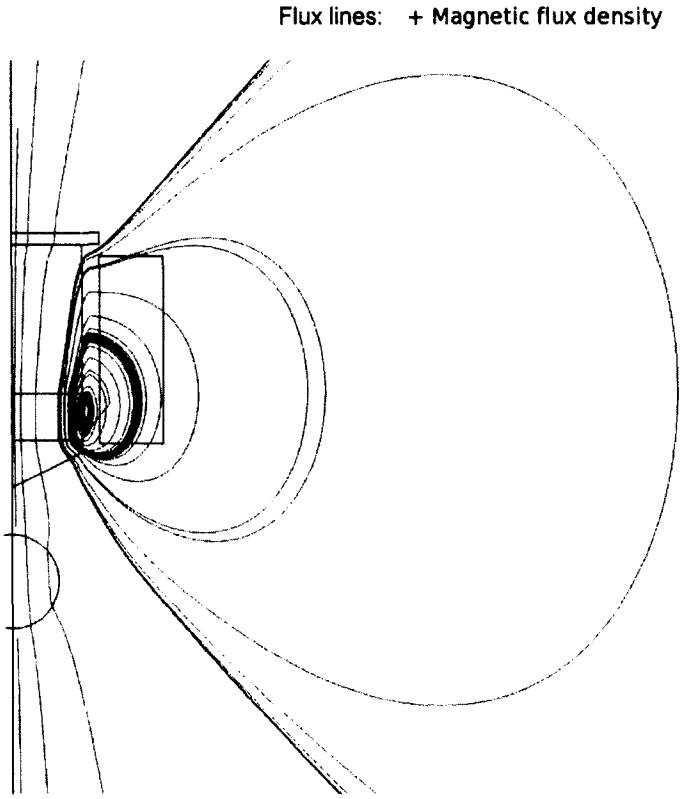

Figure 12: Magnetic flux lines for the Hybrid magnet arrangement with zero current

The method that was followed to identify the system [4, 13] is as follows:

- A simple controller is manually tuned to stabilize the system. Simple PD controllers were found to be satisfactory for stabilizing single axis maglev systems, and their effectiveness has been proved in the literature [4, 13]. As a result, a simple PD controller was manually tuned for the single axis hybrid maglev ball system.
- A suitable identification signal that covers a wide gap and maintains the stability of the system was chosen and the corresponding output was recorded. The input signal should be chosen carefully because it is a main factor controlling the accuracy of the identified model.
- The command current and the current output were recorded in order to identify the electrodynamic system.

- A suitable dynamic response was recorded separately to be used for the identification. In addition, the corresponding ball position, command current and the output current were recorded.
- The curve fitting toolbox in MatLab ® was used to generate smooth curves for all the recorded properties in order to estimate the unmeasured states.
- The generated curve for the output ball position was used to generate the instantaneous velocity and acceleration of the ball.
- The generated curve for the output current was used to generate the instantaneous time derivative of the current.
- Newton's Second Law was applied to the suspended object to estimate the parameters of the magnetic force equation.
- Kirchhoff's law, i.e. the electrical model derived in Chapter 2, was applied to the electrical circuit to estimate the parameters for the excitation current equation.
- The linear Least Square technique was followed to identify the unknown parameters.

3.3.1 Controller Tuning

Since electromagnetic suspension systems are highly unstable [4] especially when they use hybrid magnets for levitation [8], it has been a requirement to use a controller to stabilize the system in order to be able to identify its governing equations. After the experiment was set up, a PD controller was manually tuned to stabilize the system but not necessarily to produce a well-controlled response. The chosen PD parameters are $K_p = -2500$ and $K_d = -42.5$.

3.3.2 Identification Signal

Many signals were applied to the experiment in order to identify the system, but the best one was found to be a simple sinusoidal signal; the signal and the corresponding response for the experiment are shown in Figure 13. The amplitude of the sinusoidal signal is adjusted to cover a wide air gap range about the equilibrium position of the suspended object, i.e. the position in which the permanent magnet can hold the suspended object

independently without any excitation current (zero current position). The advantage of using such signal is that it maintains the system in the dynamic state without breaking its stability. As a result, the identification signal period can be extended enough to increase the accuracy of the identification.

There was significant noise in the experimental measurements, as it appears in Figures 13, 14 and 15; this noise was mostly 60 Hz. Accordingly, it was believed to be caused by a grounding issue. However, the frequency of the associated noise was out of the bandwidth of the targeted dynamics. Therefore, it will not affect model identification.

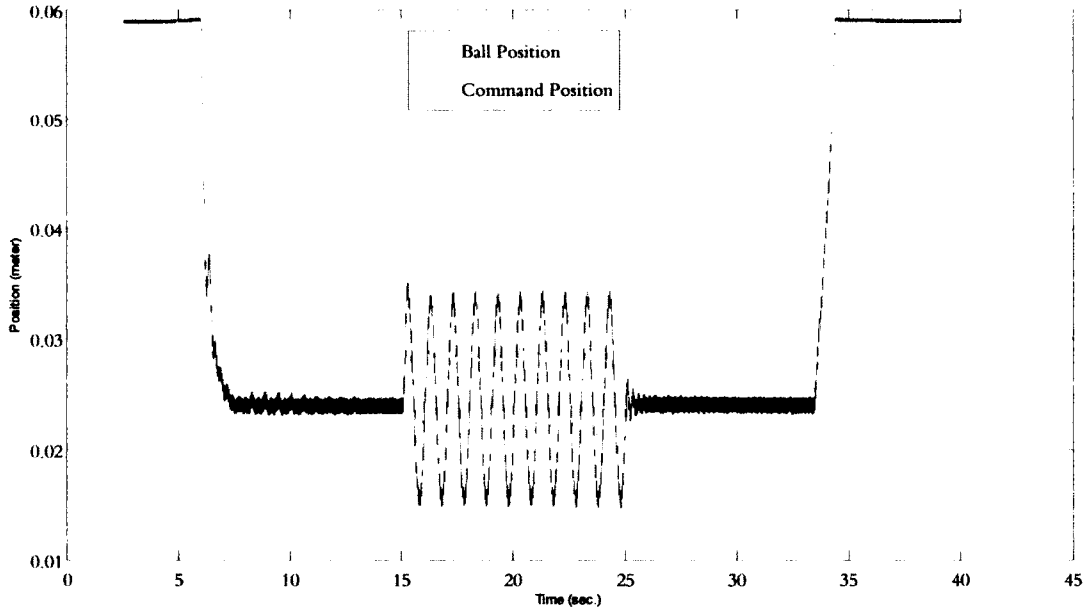

Figure 13: Identification signal and the system response

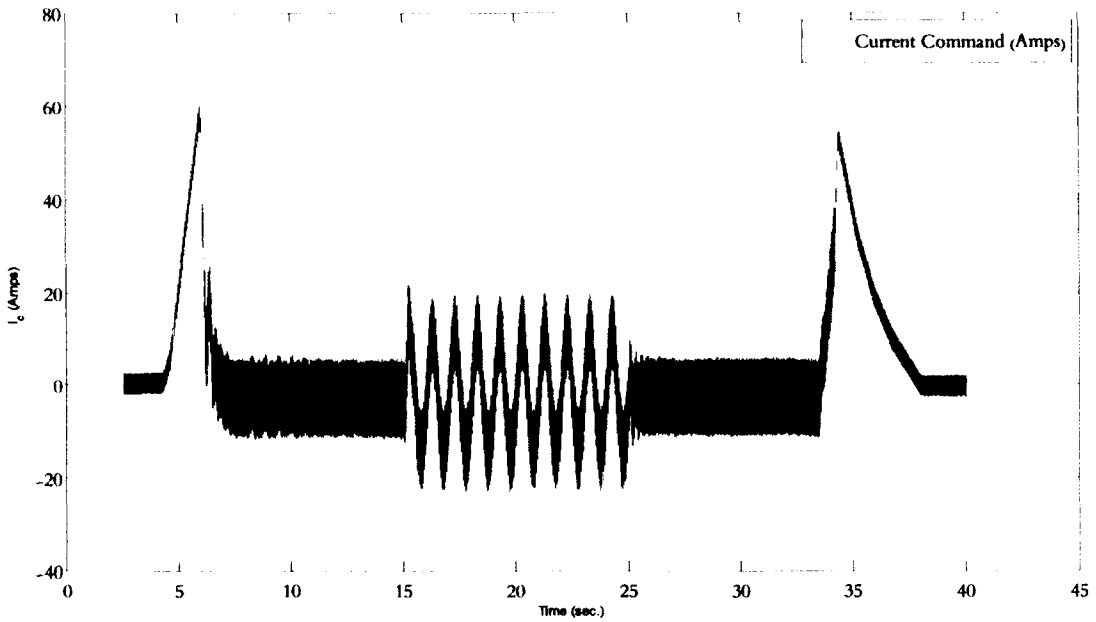

Figure 14: Current command for the identification signal

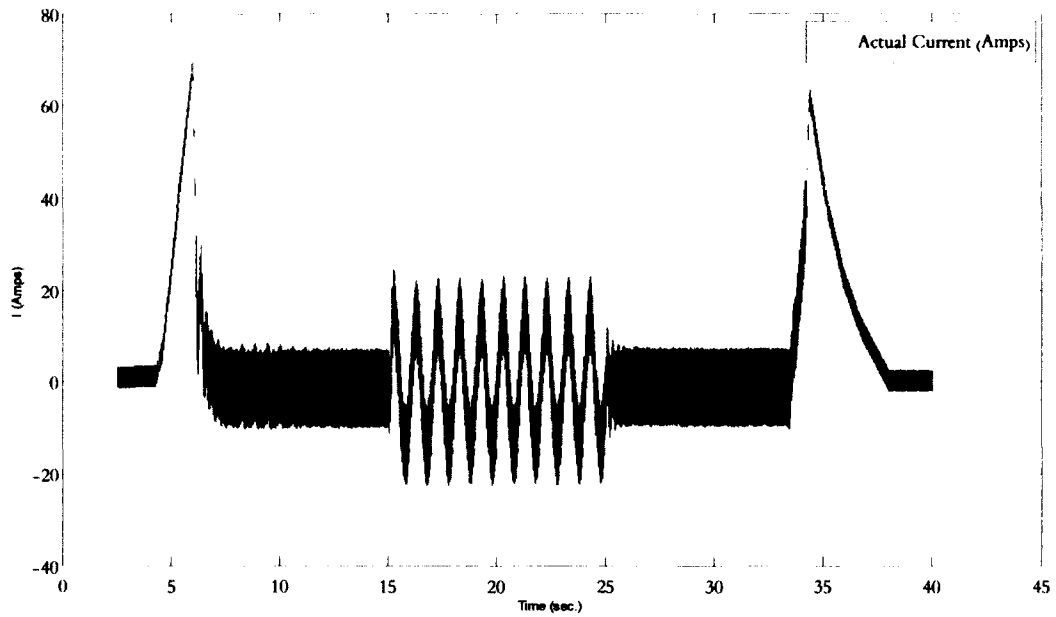

Figure 15: Output current for the identification signal

3.3.3 Chosen Identification Data and The Fitting Curves

A period of six seconds was chosen as an identification window, which is relatively long compared with data from the literature [4]. The chosen outputs are shown in Figures 16, 17 and 18. The curve fitting toolbox in MatLab® was used to fit the chosen signals and the corresponding outputs; the fitted curves are shown in Figures 16, 17 and 18.

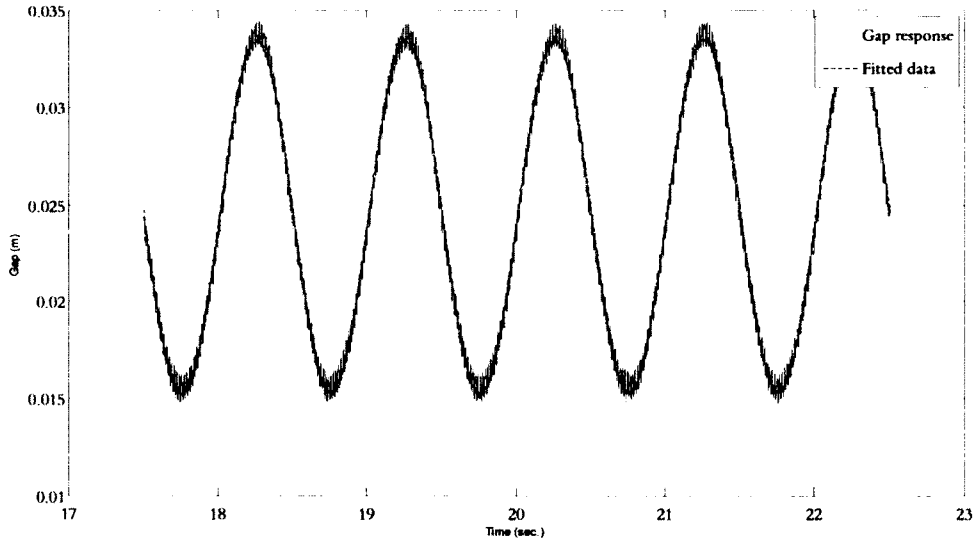

Figure 16: Gap output and its fitted curve for the chosen period

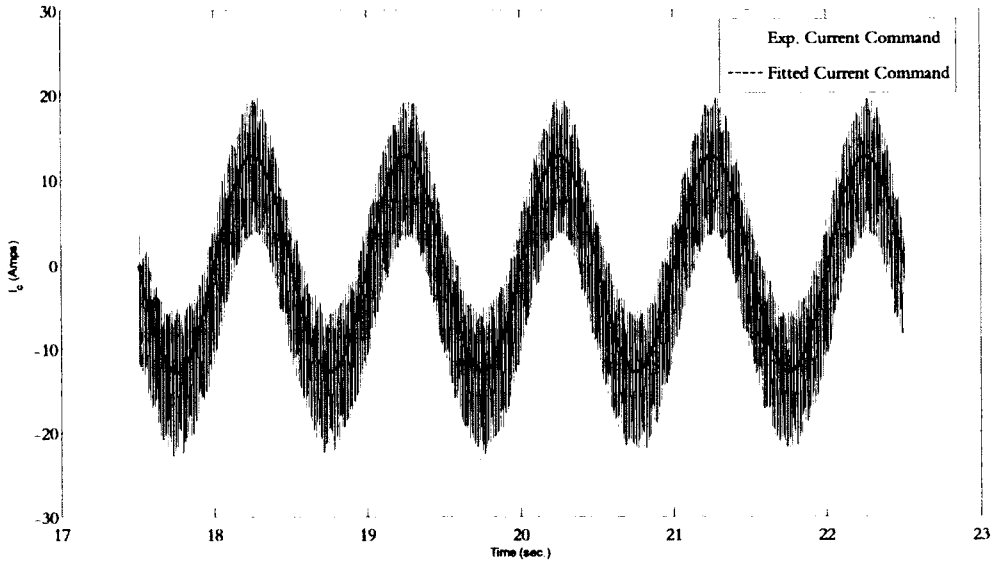

Figure 17: Current command and its fitted curve for the chosen period

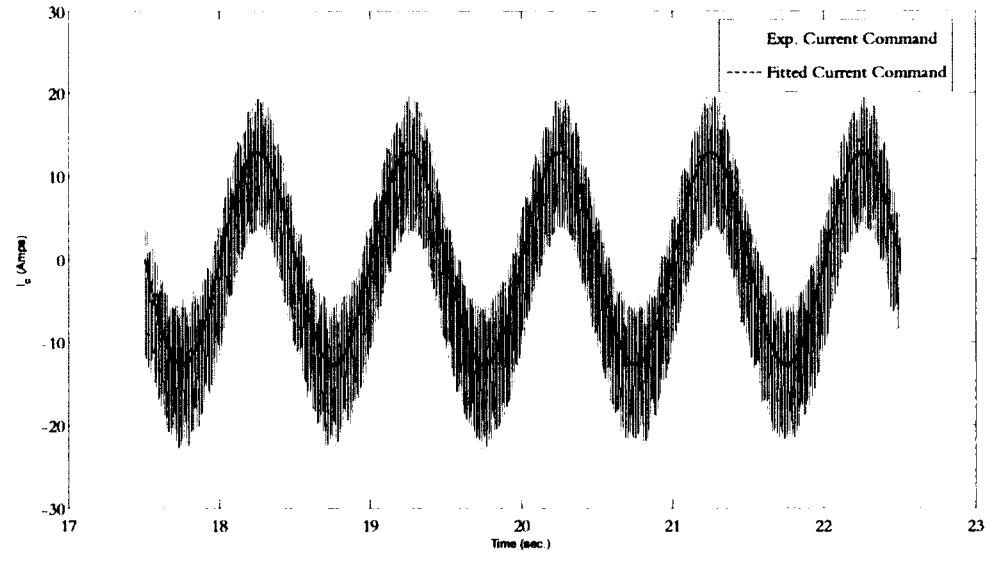

Figure 18: Current output and its fitted curve for the chosen period

3.3.4 Estimated Inputs

For the governing equations used for the dynamical system identification, the first and the second time derivatives of the gap alongside with the first time derivative of the

output current are considered as inputs. Although those states are not measured, making use of mathematics, the time derivatives may be estimated geometrically by calculating the slopes of the fitted curves. The estimated time derivatives are shown in Figures 19, 20 and 21.

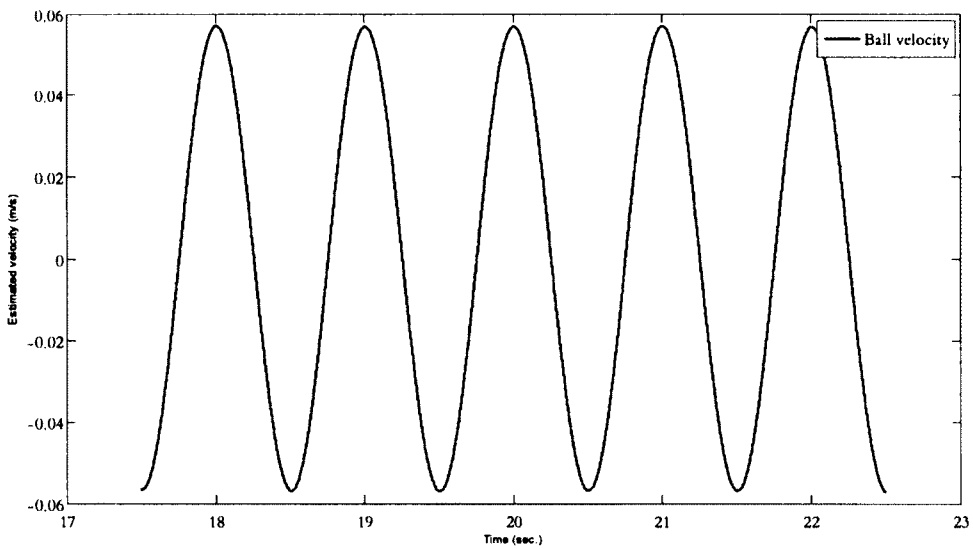

Figure 19: Estimated velocity of the Ball

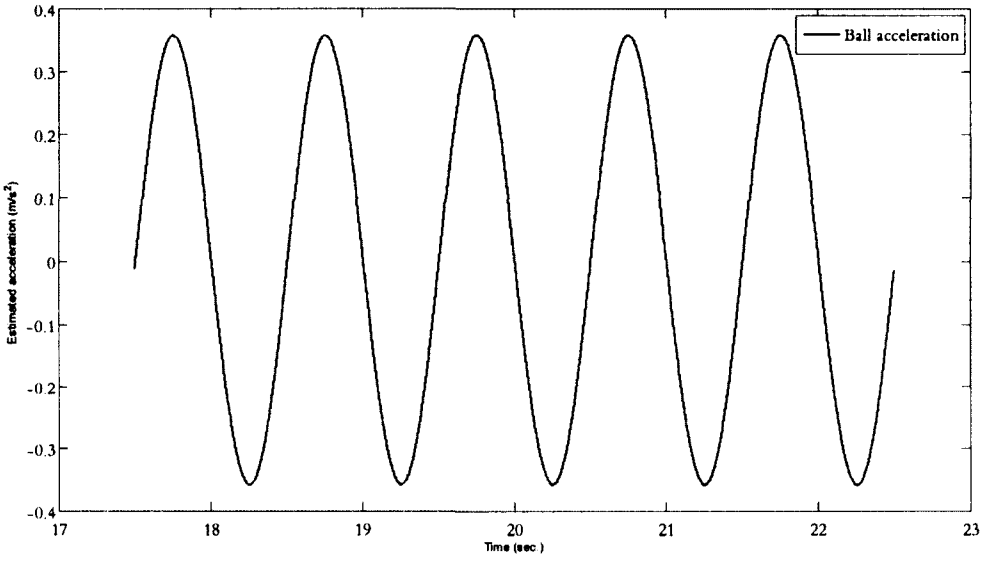

Figure 20: Estimated acceleration of the Ball

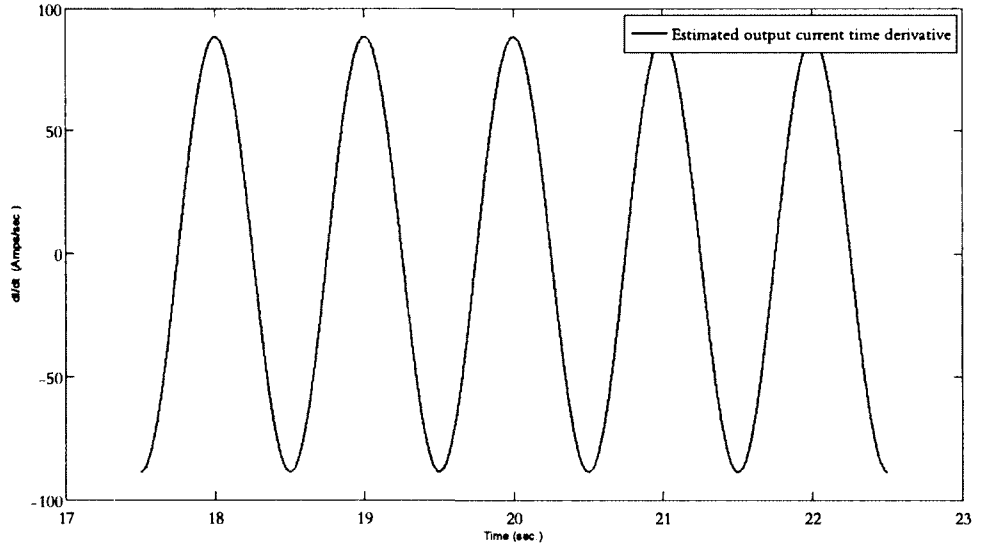

Figure 21: Estimated first time derivative of the output current

3.3.5 Identification Equations

The system to be modeled consists primarily of two sub-systems which both have to be modeled to mimic the behavior of the hybrid magnetic suspension system under study. The mechanical sub-system describes the motion of the suspended object and the forces acting upon it. This sub-system will be described by simply applying the Newton's second law on the suspended object. The other sub-system is the electrodynamic system, which describes the electrical circuit and the excitation current for the hybrid electromagnet.

3.3.5.1 Dynamics Equation

The hybrid electromagnetic attraction force equation $(2-29)$, which was derived in Chapter 2, is applied to the single axis hybrid maglev ball system in order to describe the system's dynamics as follows:

$$F(I,z) = \frac{\mu_0 A_g N^2}{2}\left[\frac{I_{eq}}{z_{eq}}\right]^2 \qquad (2-29)$$

where:

$$I_{eq} = \frac{H_c l_m}{N} + I(t) \qquad (3-1)$$

$$z_{eq} = \frac{A_g \mu_0 l_m}{A_m \mu_m} + z \qquad (3-2)$$

Applying Newton's second law, the dynamics of the single axis hybrid maglev ball system shown in Figure 22 could be derived as follows:

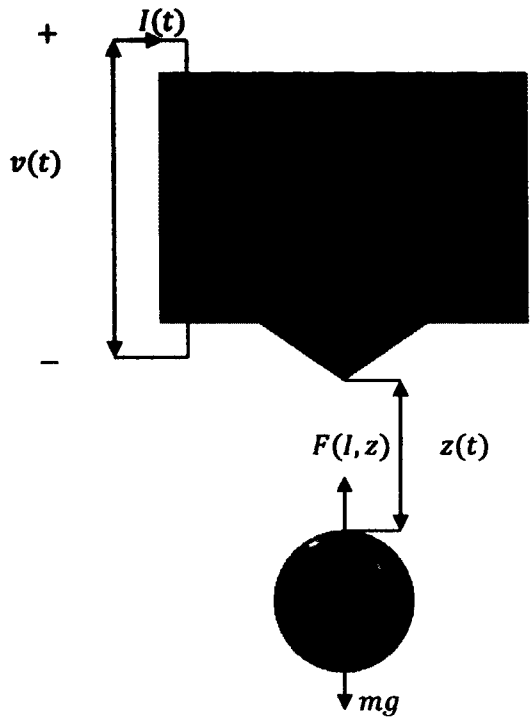

Figure 22: Free body diagram of the system

$$m\ddot{z} = -F(I,z) + mg \qquad (3-3)$$

where $F(I,z)$ is the hybrid magnet attraction force, and g is the gravitational acceleration. This expression ignores the aerodynamic resistance.

Substituting equations $(2-29), (3-1)$ and $(3-2)$ into $(3-3)$, the equation of motion of the suspended object can be written as follows:

$$m\ddot{z} = -\mu_0 A_g N^2 \left[\frac{\frac{H_c l_m}{N} + I(t)}{\frac{A_g \mu_0 l_m}{A_m \mu_m} + z}\right]^2 + mg \qquad (3-4)$$

Dividing by the mass of the suspended object, collecting and renaming the constants, the equation of motion becomes:

$$\ddot{z} = -\frac{K_f}{m}\left[\frac{a_1 + I(t)}{a_2 + z}\right]^2 + g \qquad (3-5)$$

where:

$$a_1 = \frac{H_c l_m}{N} \qquad (3-6)$$

$$a_2 = \frac{A_g \mu_0 l_m}{A_m \mu_m} \qquad (3-7)$$

$$K_f = \frac{\mu_0 A_g N^2}{2} \qquad (3-8)$$

The parameters a_1, a_2 and K_f need to be identified.

3.3.5.2 Electrodynamics Equation

Equation$(2-40)$ is used to identify the electrical circuit of the single axis hybrid maglev ball system as follows:

$$K_a(I_c - I) = RI(t) + \dot{I}(t)\frac{\mu_0 N^2 A_g}{z_{eq}} - I_{eq}(t)\frac{\mu_0 N^2 A_g \dot{z}}{z_{eq}^2} \qquad (2-40)$$

The electrical circuit equation can be rewritten as follows:

$$K_a(I_c - I) = -RI(t) + \dot{I}(t)\frac{K_l}{(a_2 + z)} - \big(a_1 + I(t)\big)\frac{K_l \dot{z}}{(a_2 + z)^2} \qquad (3-9)$$

Here a_1 and a_2 have the same expressions as in equations $(3-6)$ and $(3-7)$, and K_l has a similar expression as K_f in equation $(3-8)$ multiplied by 2.

3.3.5.3 The Auto-Regressive Form Using An Exogenous Input (ARX) Of The Governing Equations

Dealing with models, either for simulation, prediction or design, becomes easier if the number of parameters in the model is definite and preferably small. Definite here means that the used expression is not one of the infinite series, such as Fourier series,

which are used to model dynamical systems when following nonparametric systems identification techniques. Also, it is useful to write the model in a parametric time-domain model representation [4, 15] such as the ARX form.

The measurable states are $\ddot{z}, z, I_c$, I and $\dot{I}$, and g is a constant. The parameters a_1, a_2, K_f, K_a and K_l are to be identified. The (ARX) form, equation $(3-10)$, represented as follows[15]:

$$y = [\phi][\Theta] \qquad (3-10)$$

where y and ϕ are vectors that consisting of the known or measured states and Θ is a vector consisting of the unknown parameters.

3.3.5.3.1 The Auto-Regressive Form Using An Exogenous Input (ARX) For The Equation Of Motion

Rearranging, equation $(3-5)$ becomes:

$$\frac{K_f}{m}\left[\frac{a_1 + I(t)}{a_2 + z}\right]^2 = g - \ddot{z} \qquad (3-11)$$

Taking the square root of both sides:

$$\sqrt{\frac{K_f}{m}}\left[\frac{a_1 + I(t)}{a_2 + z}\right] = \sqrt{g - \ddot{z}} \qquad (3-12)$$

Separating the unknowns:

$$\sqrt{\frac{K_f}{m}}\left(a_1 + I(t)\right) = (a_2 + z)\sqrt{g - \ddot{z}} \qquad (3-13)$$

Rearranging again, the equation of motion becomes:

$$z\sqrt{g - \ddot{z}} = I(t)\sqrt{\frac{K_f}{m}} + a_1\sqrt{\frac{K_f}{m}} - a_2\sqrt{g - \ddot{z}} \qquad (3-14)$$

Equation $(3-14)$ can be written in the ARX form as follows:

$$y = [\varphi_1 \quad \varphi_2 \quad \varphi_3]\begin{bmatrix}\theta_1\\ \theta_2\\ \theta_3\end{bmatrix} \tag{3-15}$$

where

$$y = z.\sqrt{g-\ddot{z}}, \varphi_1 = I, \varphi_2 = 1, \varphi_3 = \sqrt{g-\ddot{z}}, \theta_1 = \sqrt{\frac{K_f}{m}}, \theta_2 = a_1.\sqrt{\frac{K_f}{m}} \text{ and } \theta_3 = -a_2 \tag{3-16}$$

3.3.5.3.2 The Auto-Regressive Form Using An Exogenous Input (ARX) For The Equation Of Electrodynamics

Rearranging, equation $(3-9)$ becomes:

$$K_a(I_c - I) = -RI(t) + K_l\left[\frac{\dot{I}(t)}{(a_2+z)} - \frac{\dot{z}(a_1+I(t))}{(a_2+z)^2}\right] \tag{3-17}$$

Separating the unknown parameters:

$$RI(t) = K_a(I_c - I) - K_l\left[\frac{\dot{I}(t)}{(a_2+z)} - \frac{\dot{z}(a_1+I(t))}{(a_2+z)^2}\right] \tag{3-18}$$

The ARX form of the electrical equation becomes:

$$y = [\varphi_1 \quad \varphi_2]\begin{bmatrix}\theta_1\\ \theta_2\end{bmatrix} \tag{3-19}$$

where

$$y = RI, \quad \varphi_1 = -\dot{I}/z + a_2 + \dot{z}(I+a_1)/(z+a_2)^2, \quad \varphi_2 = I_c - I, \quad \theta_1 = K_l \; and \; \theta_2 = K_a \tag{3-20}$$

3.3.6 Parameter Estimation Using The Least Square Method

The Linear Least Square method is one of the parametric identification methods that belong to the family of Prediction Error Methods (PEM). These methods are based on the minimization of a cost function, which is the sum of the squared prediction errors. Given measurements of inputs and outputs, and given a model structure in the ARX form with unknown parameters, the Linear Least Square method estimates the unknown parameters according to the following equation:

$$\hat{\theta}_{LS} = (\phi^T \phi)^{-1} \phi^T . y \qquad (3-21)$$

where $\hat{\theta}_{LS}$ is a vector consisting of the estimated values for the virtual unknowns, ϕ is a vector consisting of the virtual inputs and y is a vector consisting of the virtual outputs.

A Software tool using MatLab® has been built to estimate the unknown parameters using the linear Least Square method. The software tool is contained in the Appendix. Applying the candidate data and the ARX equations for the dynamic and the electric models of the system to the software tool yields:

$$\hat{\theta}_{LS_D} = \begin{bmatrix} 0.00215 \\ 0.1000 \\ -0.0070 \end{bmatrix} \qquad (3-22)$$

$$\hat{\theta}_{LS_E} = \begin{bmatrix} 0.0065 \\ 11.7858 \end{bmatrix} \qquad (3-23)$$

Applying equations $(3-16)$ and $(3-20)$, the unknown parameters are:

$$\begin{gathered} a_1 = 46.5894 \\ a_2 = 0.0070 \\ K_f = 5.0678e-06 \\ K_a = 11.7858 \\ K_l = 0.0065 \end{gathered} \qquad (3-24)$$

Accordingly, the modeling equations $(3-5)$ and $(3-9)$ become:

$$\ddot{z} = -\frac{5.0678e-06}{m}\left[\frac{46.5894 + I(t)}{0.0070 + z}\right]^2 + g \qquad (3-25)$$

$$11.7858(I_c - I) = -RI(t) + \dot{I}(t)\frac{0.0065}{(0.0070 + z)} - \left(46.5894 + I(t)\right)\frac{0.0065 * \dot{z}}{(0.0070 + z)^2} \qquad (3-26)$$

CHAPTER 4

MODEL VALIDATION

4.1 INTRODUCTION

Identified models always include uncertainties. Therefore, a means to evaluate the correctness or validity of the model is necessary. The validity of the model has to be examined in order to increase our confidence in it. Without proving its validity, the model is worthless [15]. System identification is an iterative process starting with the mathematical structure build-up through parameter estimation and concluding with model validation. If the validation process indicates that the model is not good, then some or all of the other stages should be changed starting from the mathematical model and proceeding through the experiment set-up, along with the input signal selection for the parameter estimation method. In general, a different set of data, other than the identification set, is used to validate the model. The most straightforward way is to compare real and simulation outputs for the same conditions and inputs. If they differ too much, it will be concluded that the model is invalid. This type of validation is called *face validation* [15]. The degree of accuracy is a rather subjective criterion. To prove the validity of the model, validation was established by showing that it is not invalid; thus, the validation process is sometimes called the *invalidation process*. In this chapter, different methods and strategies to validate the model have been employed, most of them are of the face validation type.

4.2 DIRECT APPLICATION OF THE IDENTIFIED EQUATIONS

Equations $(3-25)$ and $(3-26)$ were utilized for the ball position and the output current respectively and the input data, which was used to identify the system, was then applied to those equations to compare the outputs of the identified model with the outputs from the actual system. The results have been plotted in an overlay fashion for comparison, as shown in Figures 23 and 24.

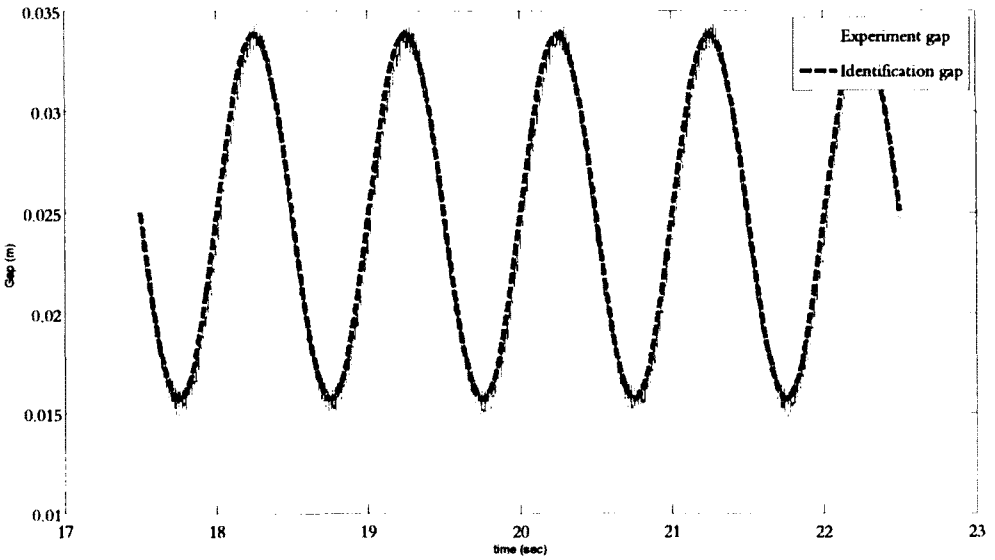

Figure 23: Identification gap output for the real and the identified systems

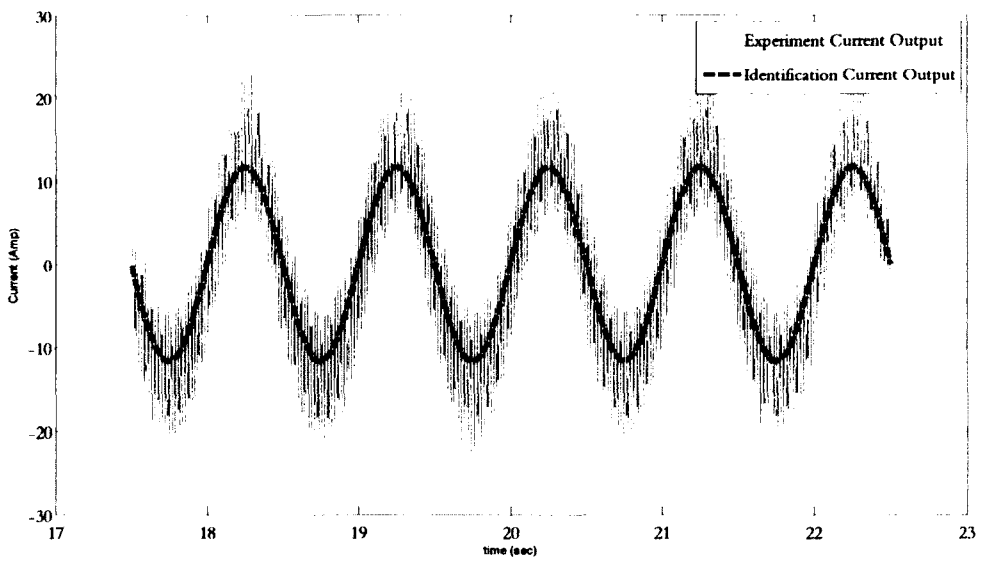

Figure 24: Identification current output for the real and the identified systems

Comparing the direct application of the identified model and the actual system output in Figures 23 and 24, it is very clear that the identified model is valid.

4.3 STATIC FORCE OF THE PERMANENT MAGNET

The levitation force of the permanent magnet with respect to the air gap was estimated experimentally, as discussed in Chapter 3. For greater convenience, the identified model for the hybrid electromagnetic force was applied with respect to the air gap and with zero excitation current to simulate the static force of the permanent magnet. The two attraction forces are represented in Figure 25.

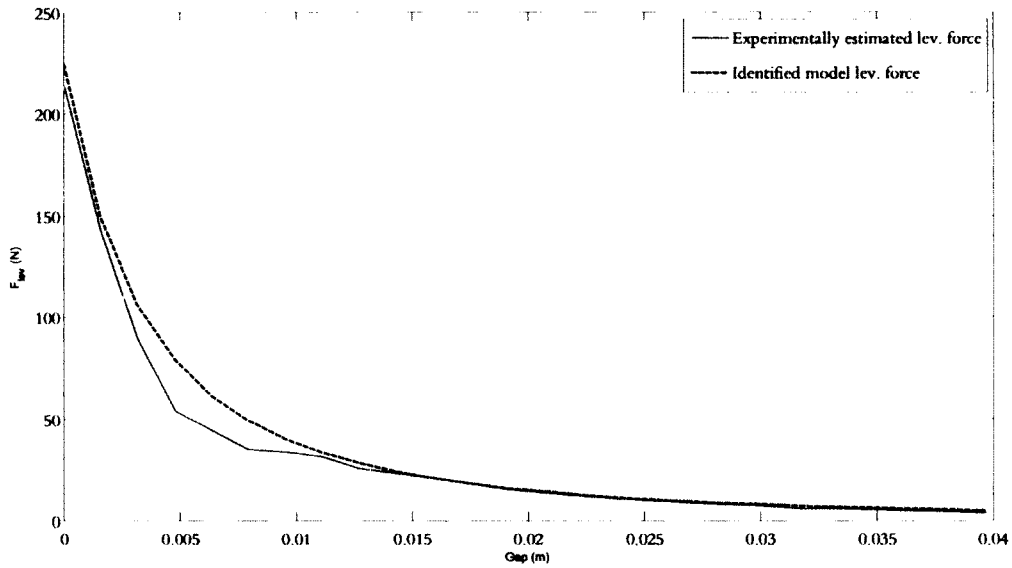

Figure 25: Experimentally estimated and identified model static levitation force for the hybrid magnet vs. air gap

The two curves match closely in both magnitudes and profile shapes compared with the results provided by [8], which proves the validity of the identified model.

4.4 NONLINEAR SIMULATION

A nonlinear model using the MatLab simulation platform (Simulink ®) has been built to mimic the behavior of the hybrid maglev system using the identified model. The Runge-Kutta 4 package for numerical integration has been applied for the integration. The

block diagram for the nonlinear Simulink® model is shown in Figure 26. The model was divided into three subsystems as described in Figure 26:

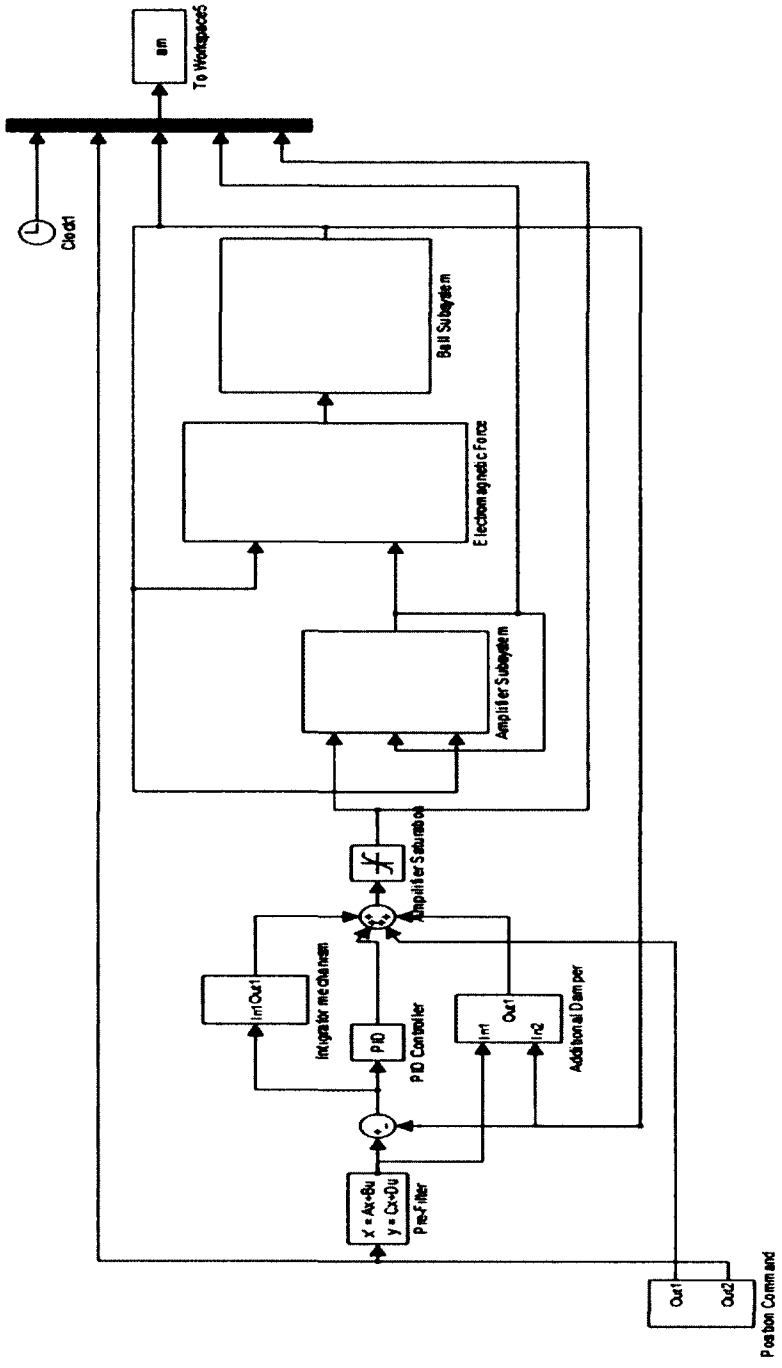

Figure 26: Numerical nonlinear Simulink ® model for the system

4.4.1 Amplifier Subsystem

The amplifier subsystem simulates the electrical circuit, taking the current command, output current and the ball position as inputs to generate the corresponding required current. The block diagram for the amplifier subsystem is shown in Figure 27.

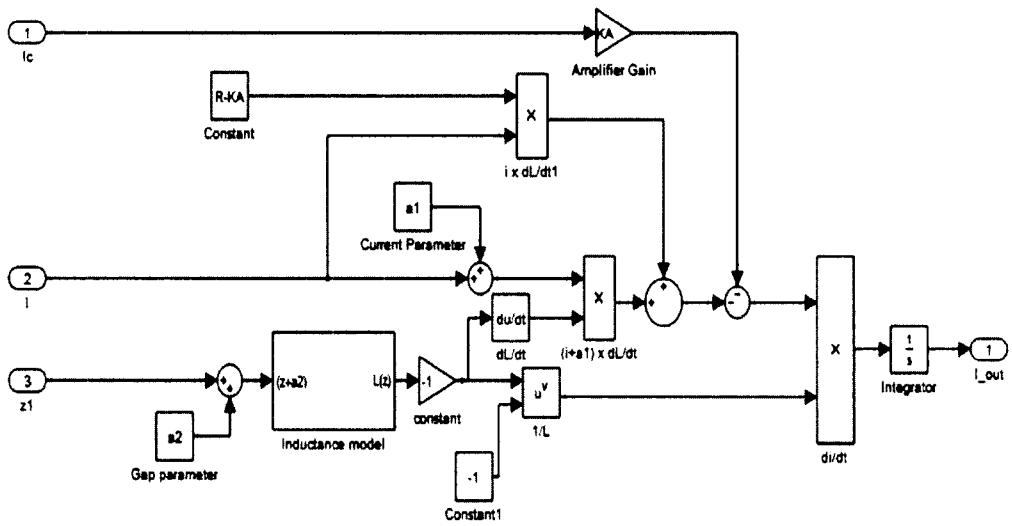

Figure 27: Nonlinear Simulink ® model for the electrical circuit

4.4.1.1 Inductance Model

The inductance subsystem takes the ball position as an input to generate the corresponding inductance. The block diagram for the inductance sub-model is shown in Figure 28.

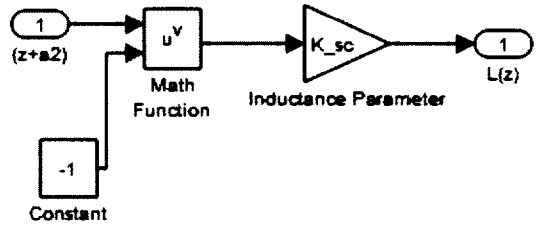

Figure 28: Inductance sub-model

4.4.2 Electromagnetic Force Subsystem

The electromagnetic force subsystem generates the hybrid magnet attraction force, using the current output and the ball position as inputs. The block diagram of the electromagnetic force subsystem is shown in Figure 29.

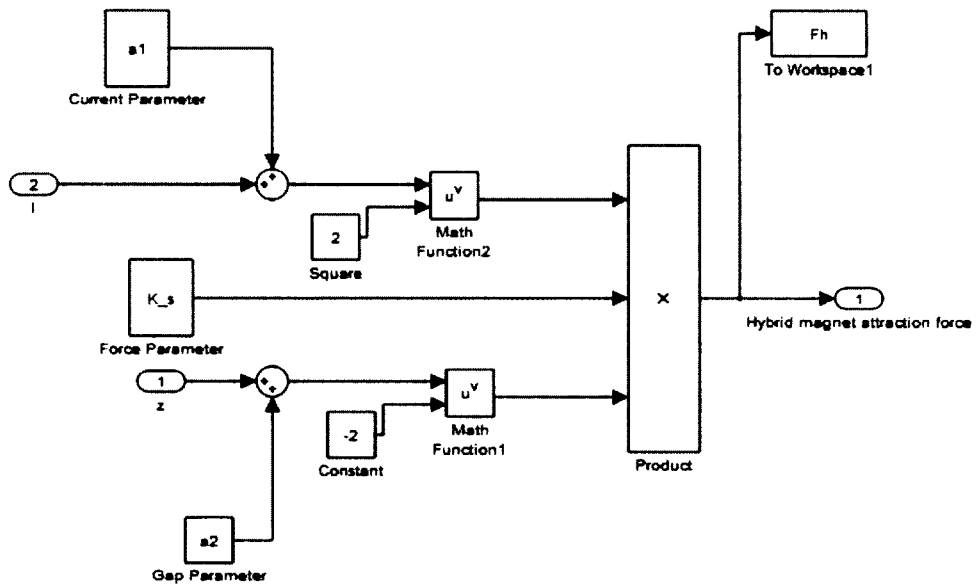

Figure 29: Hybrid electromagnetic force sub-model

4.4.3 Ball Dynamics Subsystem

The ball dynamics subsystem applies Newton's second law, taking the hybrid magnet attraction force as input and producing the ball position as an output by integrating the acceleration twice. The forces that act on the ball are the gravitational force, the hybrid electromagnetic force and the pedestal force. The pedestal force is basically the initial static force required to move the ball from its at-rest state. The block diagram for the ball dynamics subsystem is shown in Figure 30.

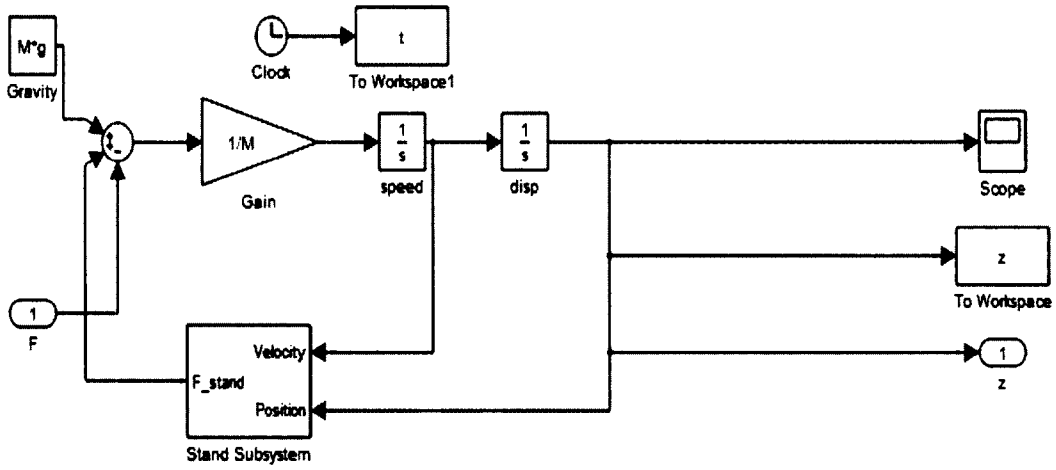

Figure 30: Ball dynamics sub-model

4.4.3.1 Stand Subsystem

The pedestal force was modeled as a spring damper combination that operates only when the ball is in its initial position [13]. The spring and damper coefficients have been adjusted manually, based on the peak output current required to move the ball from its static state. A switching block has been used to discontinue the pedestal mechanism when the ball starts moving. The stand subsystem block diagram is shown in Figure 31.

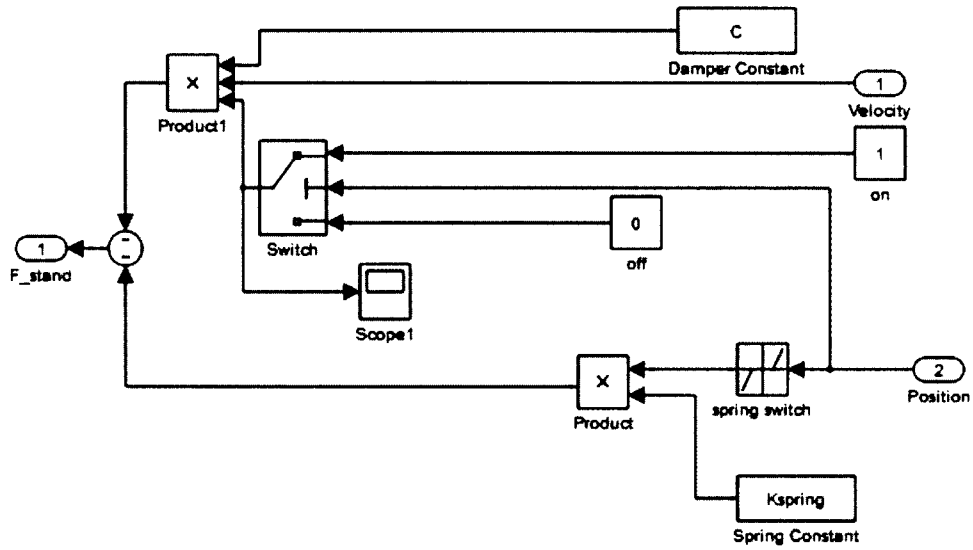

Figure 31: Pedestal force sub-model

4.4.4 Simulation Validation

The nonlinear simulation was run using three PD controller settings, and the results were overlaid with the corresponding outputs of the actual system using the same settings for the controller. For the first two controller settings, two different signals were tested, and for the third setting, only one signal was tested. The results are represented in an overlay fashion as follows:

4.4.4.1 CASE I-Sinusoidal Signal

Using the identification signal, shown in Figure 13, with the associated controller set, $Kp = -2500$ and $K_d = -42.5$, the real-time and simulated histories are shown in Figures 32-34.

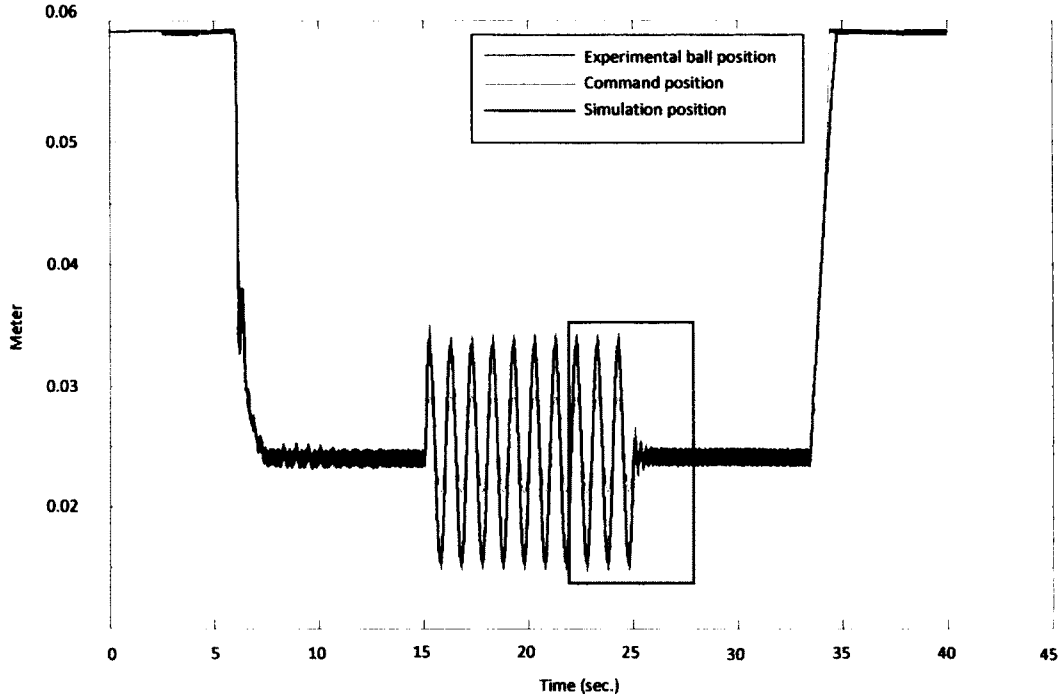

Figure 32: Real-time and simulation outputs for Case I

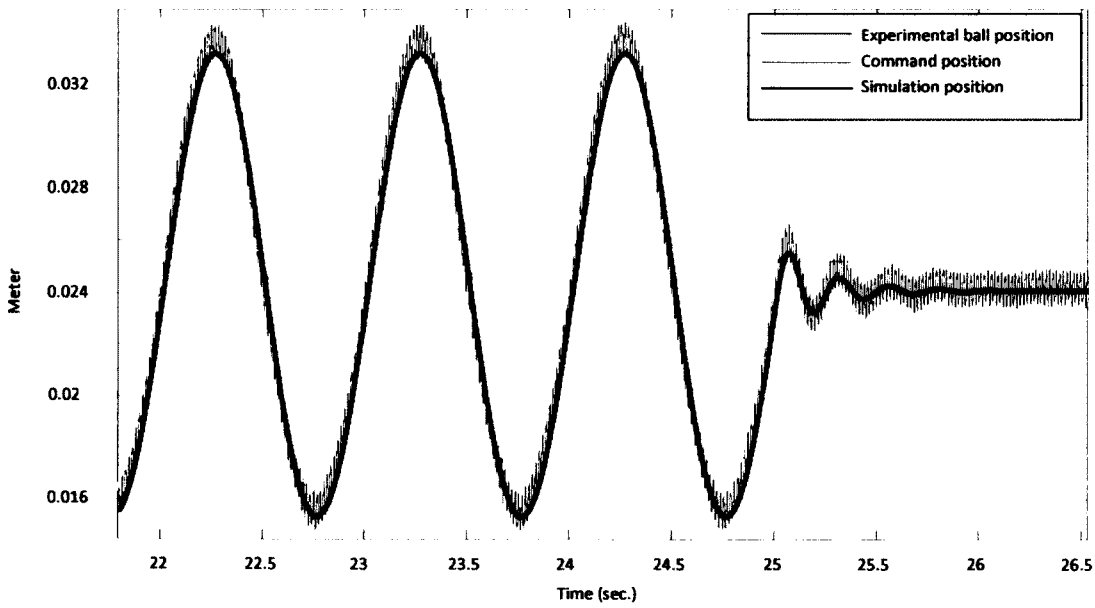

Figure 33: Real-time and simulation outputs for Case I zoomed in at the box shown in Figure 32

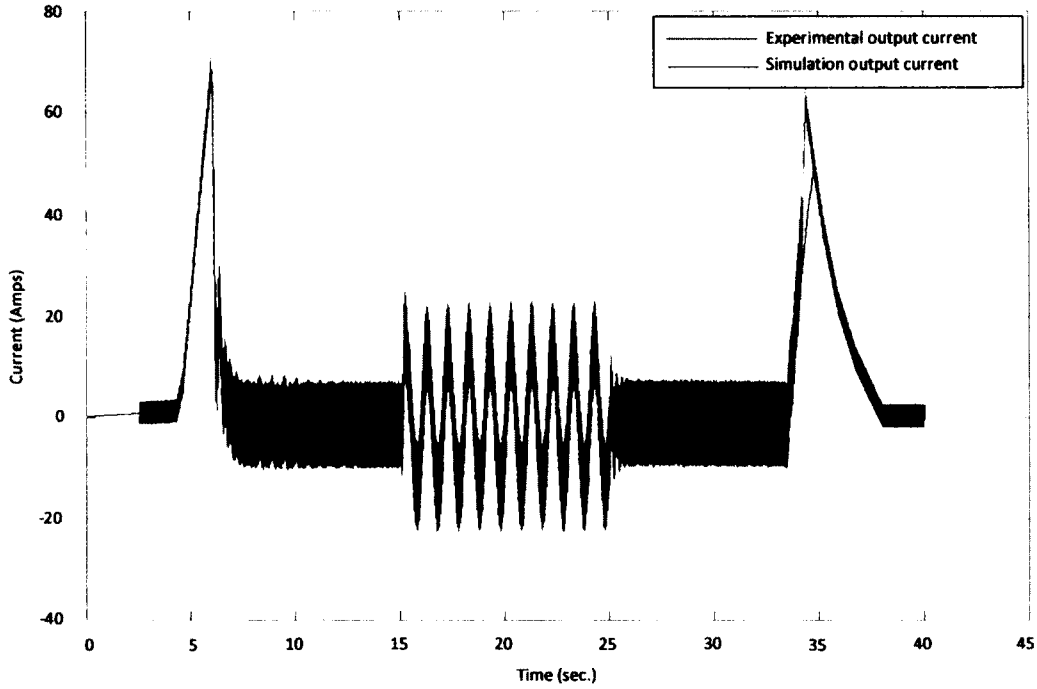

Figure 34: Real-time and simulation current outputs for Case I

4.4.4.2 CASE II-Step Signal

Using a step signal of $(0.005\ m)$ which is considered as an extreme signal for this kind of applications with controller gains $Kp = -2500$ and $d = -42.5$, the real-time and simulated histories are shown in Figures 35-37.

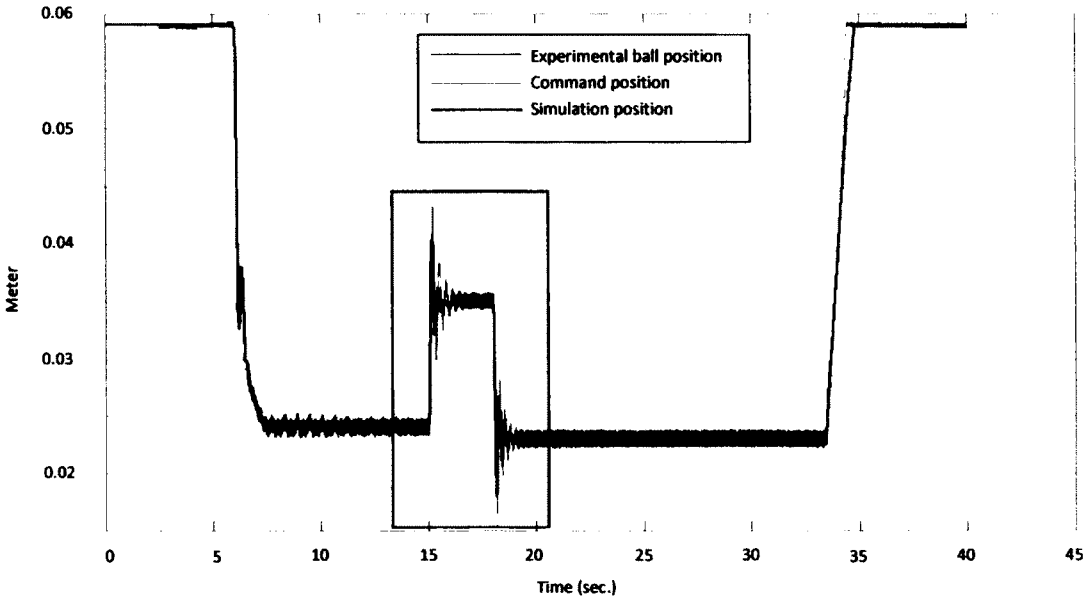

Figure 35: Real-time and simulation outputs for Case II

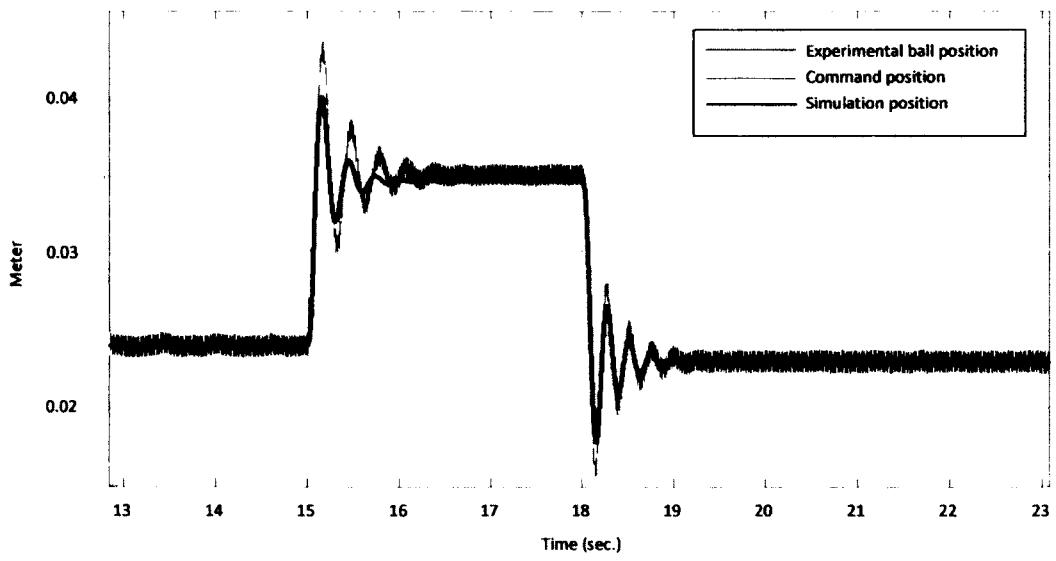

Figure 36: Real-time and simulation outputs for Case II zoomed in at the box shown in Figure 25

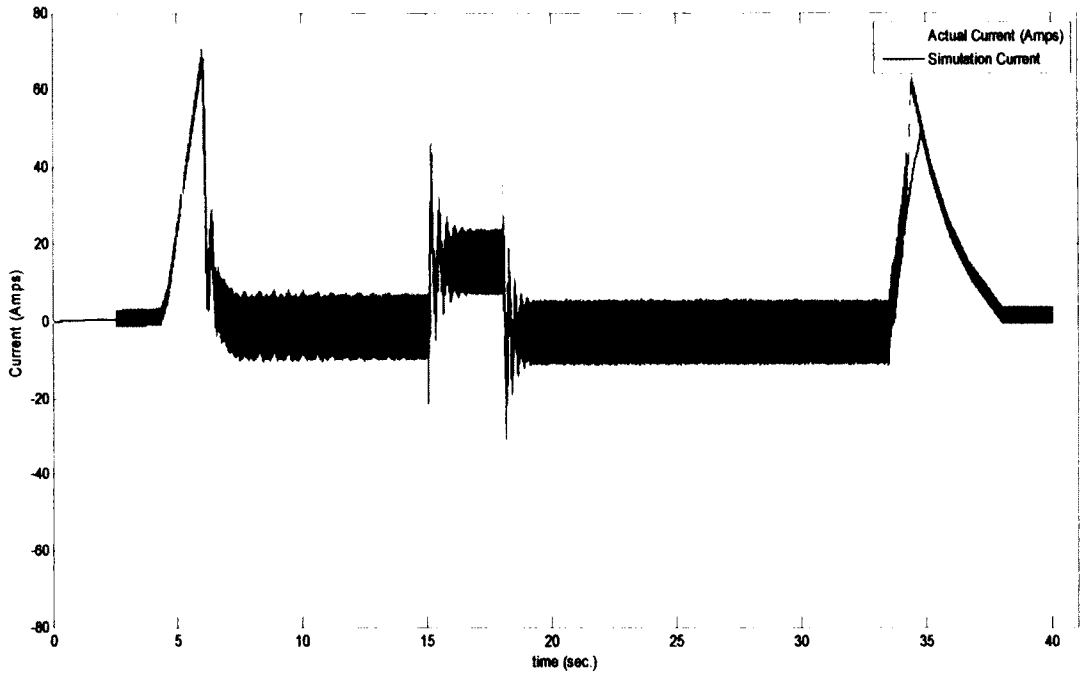

Figure 37: Real-time and simulation current output for Case II

4.4.4.3 CASE III-Sinusoidal Signal

Using a sinusoidal signal with different amplitude, levitation position and controller setting than in Case I. The controller gains were $Kp = -2500$ and $K_d = -51$, the real-time and simulated histories are shown in Figures 38-40.

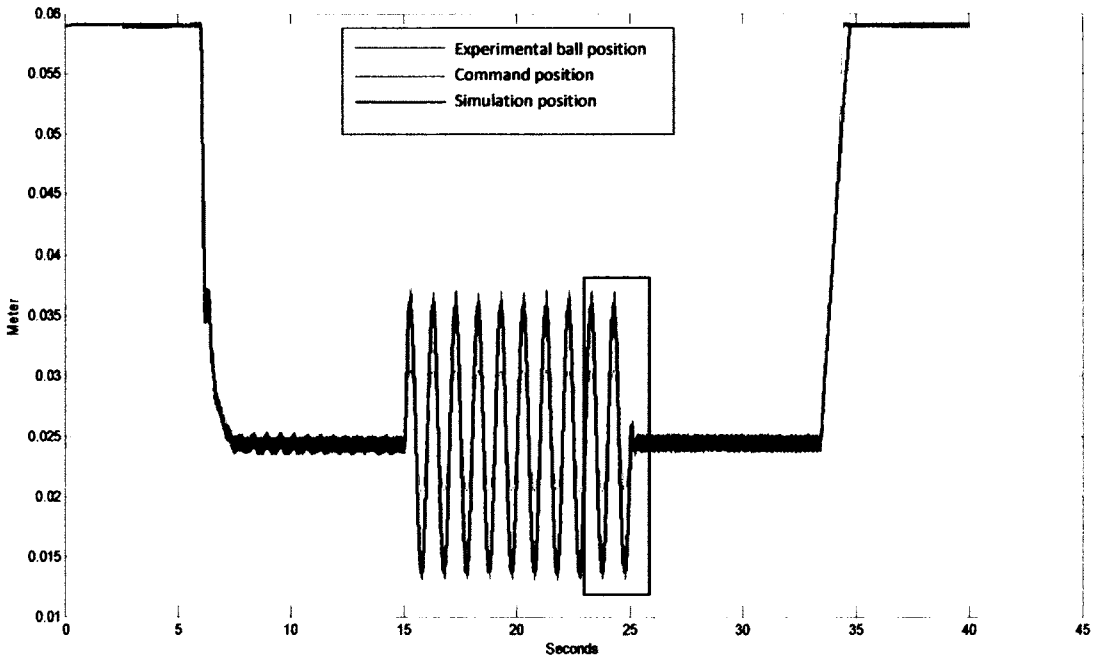

Figure 38: Real-time and simulation outputs for Case III

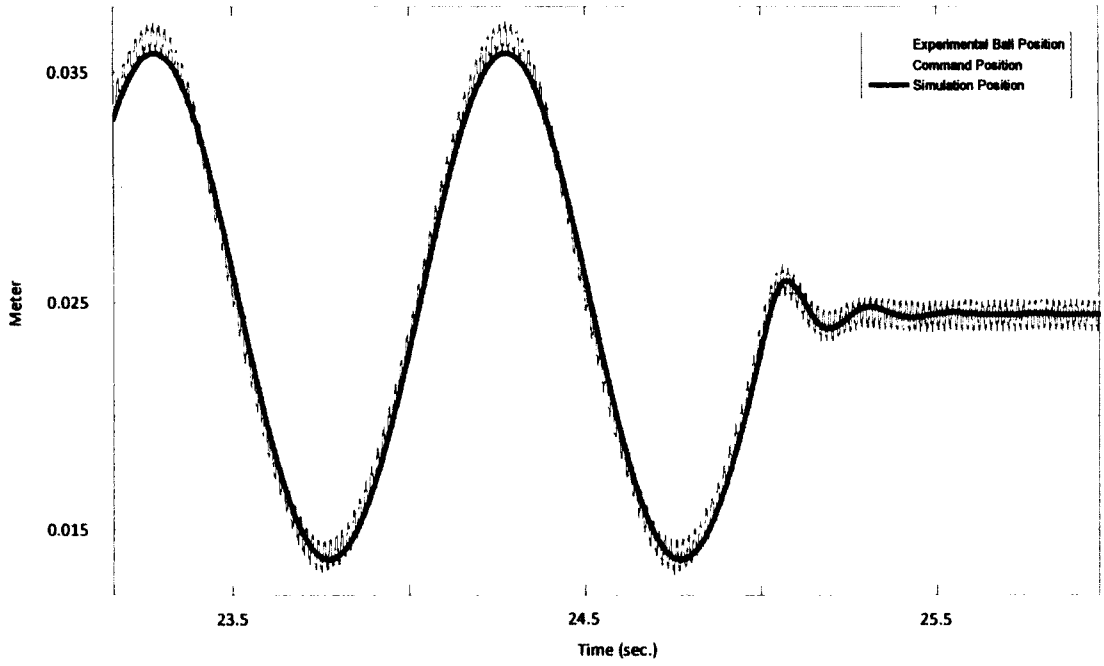

Figure 39: Real-time and simulation outputs Case III zoomed in at the box shown in Figure 38

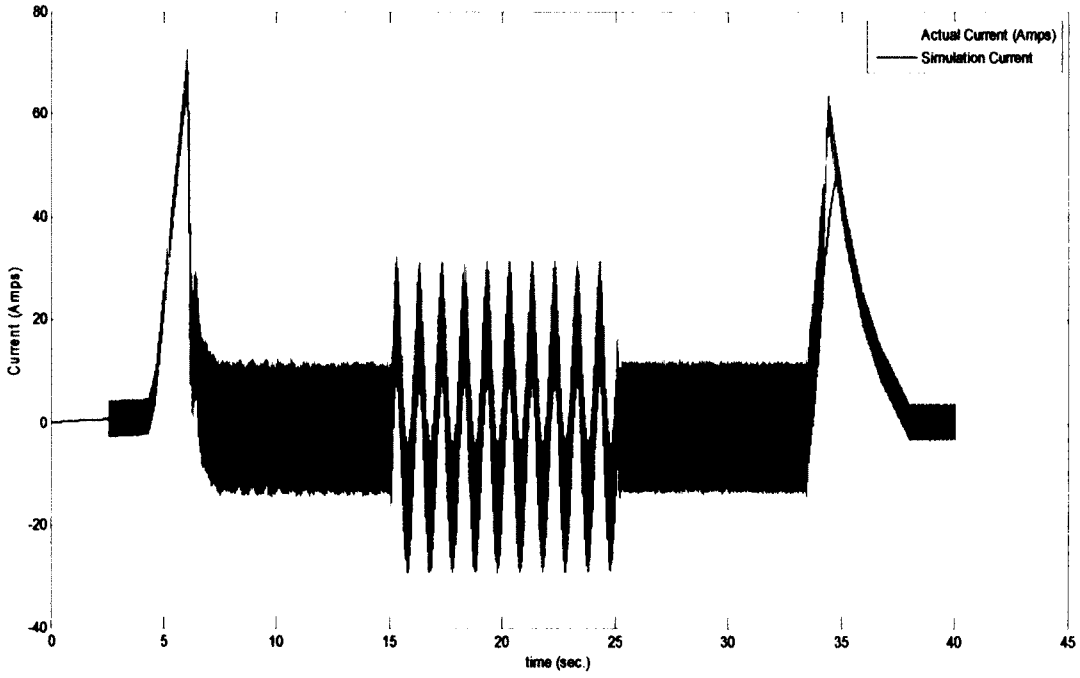

Figure 40: Real-time and simulation current outputs for Case III

4.4.4.4 CASE IV-Step Signal

Using a step signal of $(0.003\,m)$ with same levitation gap as in case III and a controller with $Kp = -2500$ and $d = -51$, the real-time and simulated histories are shown in Figures 41-43.

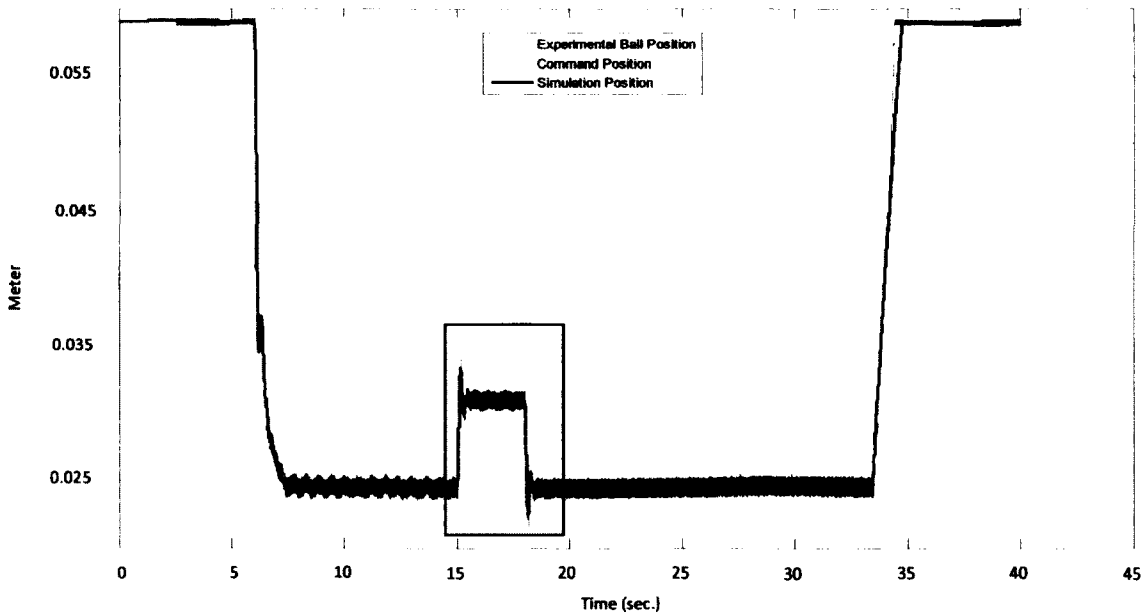

Figure 41: Real-time and simulation outputs for Case IV

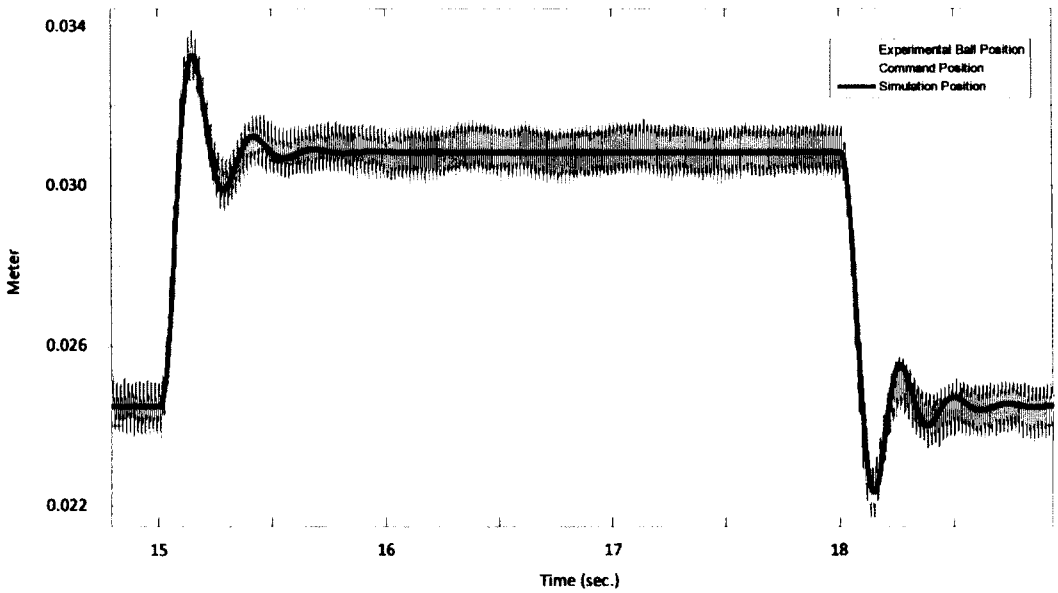

Figure 42: Real-time and simulation outputs for Case IV zoomed in at the box shown in Figure 41

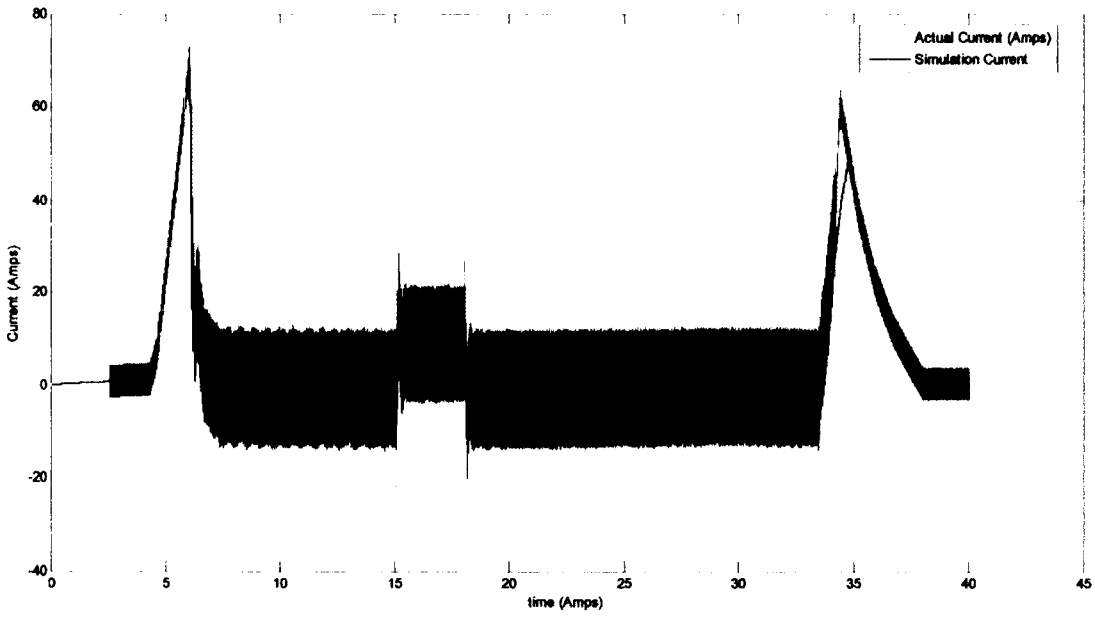

Figure 43: Real-time and simulation current outputs for Case IV

4.4.4.5 CASE V-Sinusoidal Signal

Using a sinusoidal signal with an amplitude of $0.001\ m$, a levitation position of $0.0254\ m$ and the controller gains were $Kp = -2500$ and $K_d = -34$, the real-time and simulated histories are shown in Figures 44-46.

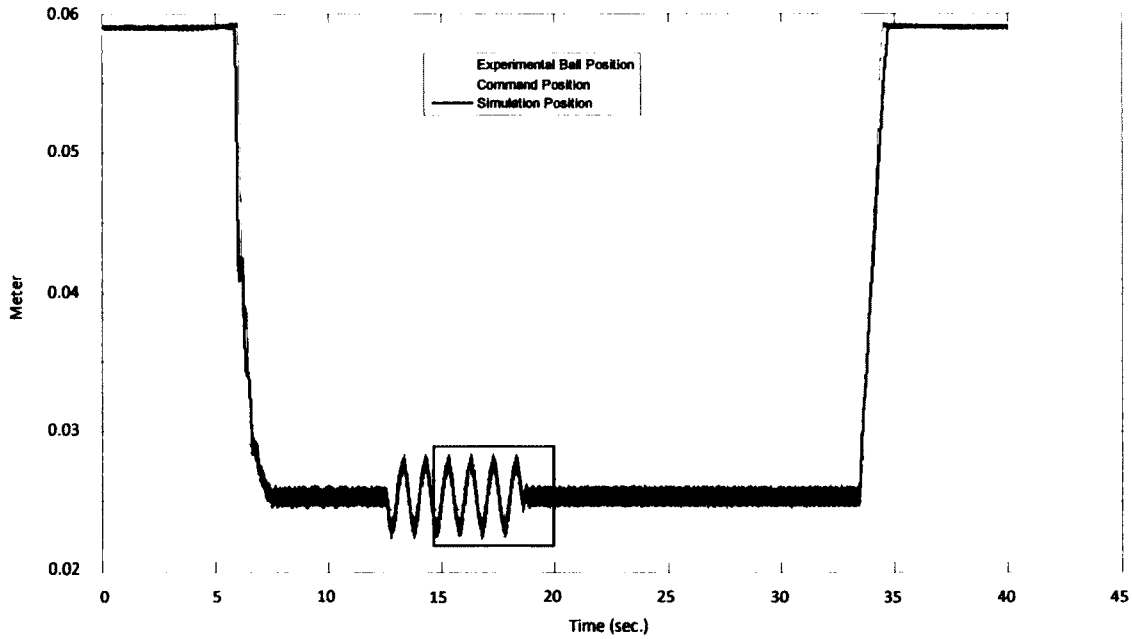

Figure 44: Real-time and simulation outputs for Case V

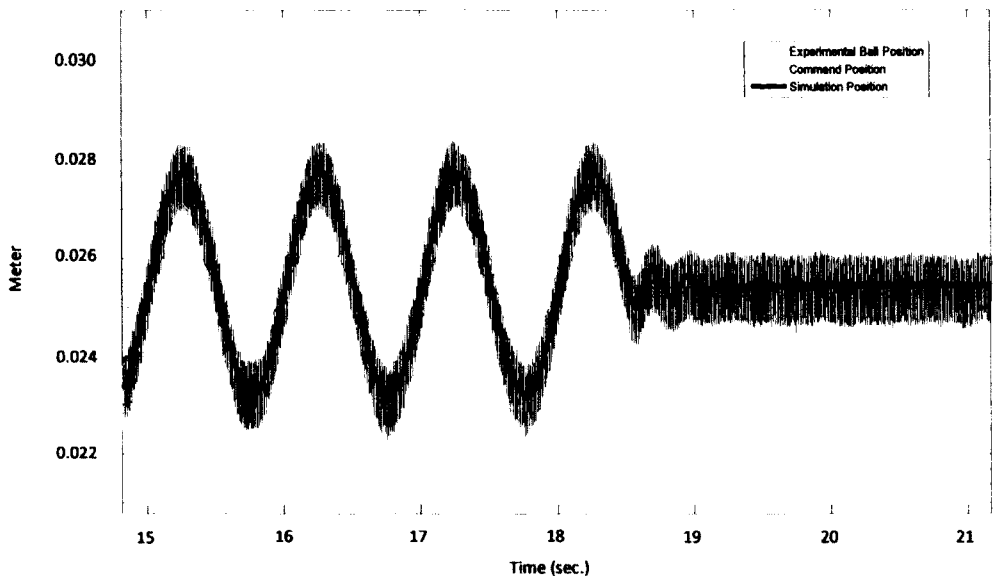

Figure 45: Real-time and simulation outputs for Case V zoomed in at the box shown in Figure 44

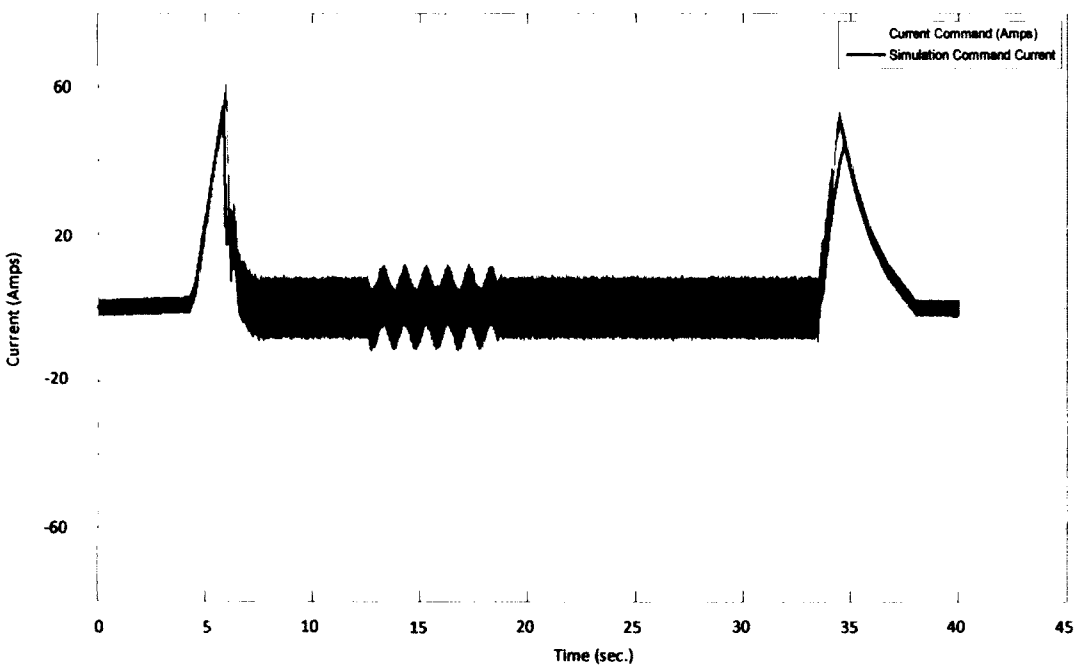

Figure 46: Real-time and simulation command current for Case V

4.4.5 Simulation Results Interpretation

It is clearly seen in Figures 32 through 46 that the identified model describes closely the actual hybrid magnetic suspension system for both dynamic and static states. Some differences appeared in Case II; the reason for the difference is that the output signal exceeded the gap range of the identification. However, the frequency of the simulation output still matched the frequency of the actual system output.

4.5 DEVIATION OF THE THEORETICAL EQUATIONS

The identified model has the same structure as the theoretical model and it has already been shown in this chapter that the identified model closely describes the behavior of the actual system. However, the parameters of the theoretical model can be calculated as follows:

Employing the values of the characteristics of the system in the theoretical equations
$(3-1)$ and $(3-2)$:

$$I_{eq_{th}} = \frac{H_c l_m}{N} + I(t) \qquad (3-1)$$

$$z_{eq_{th}} = \frac{A_g \mu_0 l_m}{A_m \mu_m} + z \qquad (3-2)$$

yields:

$$I_{eq_{th}} = \frac{873.344 * 10^3 * 0.0254}{493} + I(t) = 44.9958 + I(t)$$

$$z_{eq_{th}} = \frac{A_g \mu_0 l_m}{A_m \mu_m} + z(t) = \frac{1 * 0.0254}{1.05} = 0.0242 + z(t) \qquad (4-1)$$

$$K_{i_{th}} = \mu_0 A_g N^2 = 4 * \pi * 10^{-7} * 493^2 * \pi * 0.0762^2 = 0.005571$$

$$K_{f_{th}} = \frac{\mu_0 A_g N^2}{2} = \frac{4}{2} * \pi * 10^{-7} * 493^2 * \pi * 0.0762^2 = 0.002786$$

Comparing the parameters of the identified and the theoretical models, equations $(3-24)$ and $(4-1)$, it is clear that:

$$K_{l_{th}} \approx K_{l_I}$$

$$a_{1_{th}} \approx a_{1_I}$$

where $K_{l_{th}}$ is the theoretical value of the inductance constant, K_{l_I} is the identified value of the inductance constant, $a_{1_{th}}$ is the theoretical value of the equivalent current of permanent magnet, and a_{1_I} is the identified value of the equivalent current of the permanent magnet.

The theoretical values for the other parameters in equation $(2-28)$ were significantly different from the identified values. Accordingly, some further study to seek the reason behind that deviation was conducted.

As shown previously, the magnetic attraction force is directly proportional to the square of the magnetic flux density. Thus, the theoretical and the measured magnetic flux densities with respect to the air gap were plotted together for comparison as shown in Figure 47.

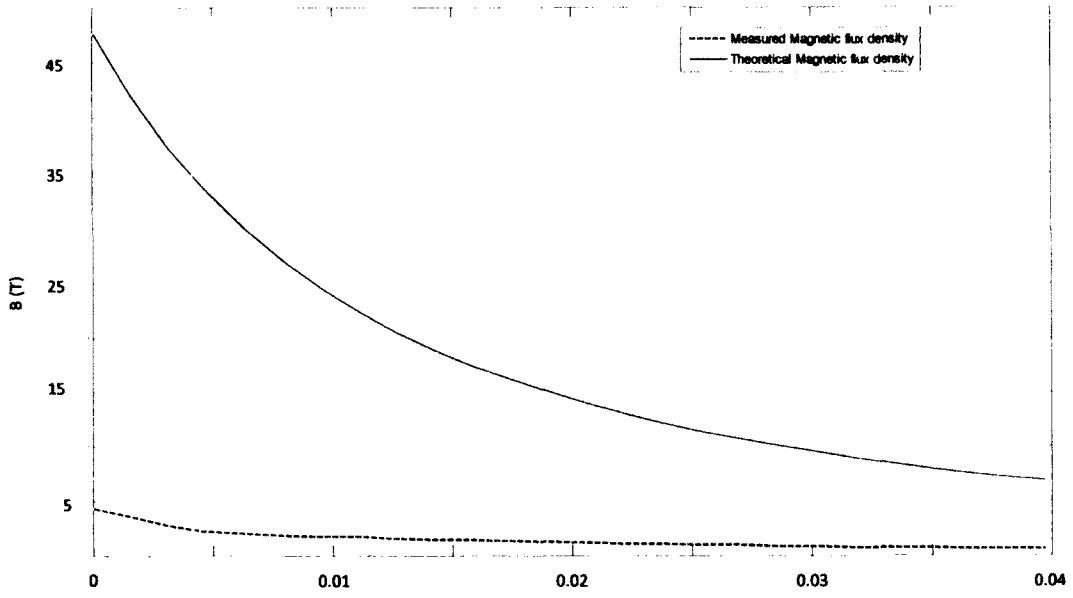

Figure 47: Measured and theoretical magnetic flux density for the hybrid system

It is seen that the magnetic flux density plots neither match the magnitudes nor profile shapes. To explore the reason behind the difference, a Comsol Multiphysics ® simulation was implemented to the hybrid system with zero current and the results are shown in Figures 48, 49 and 50.

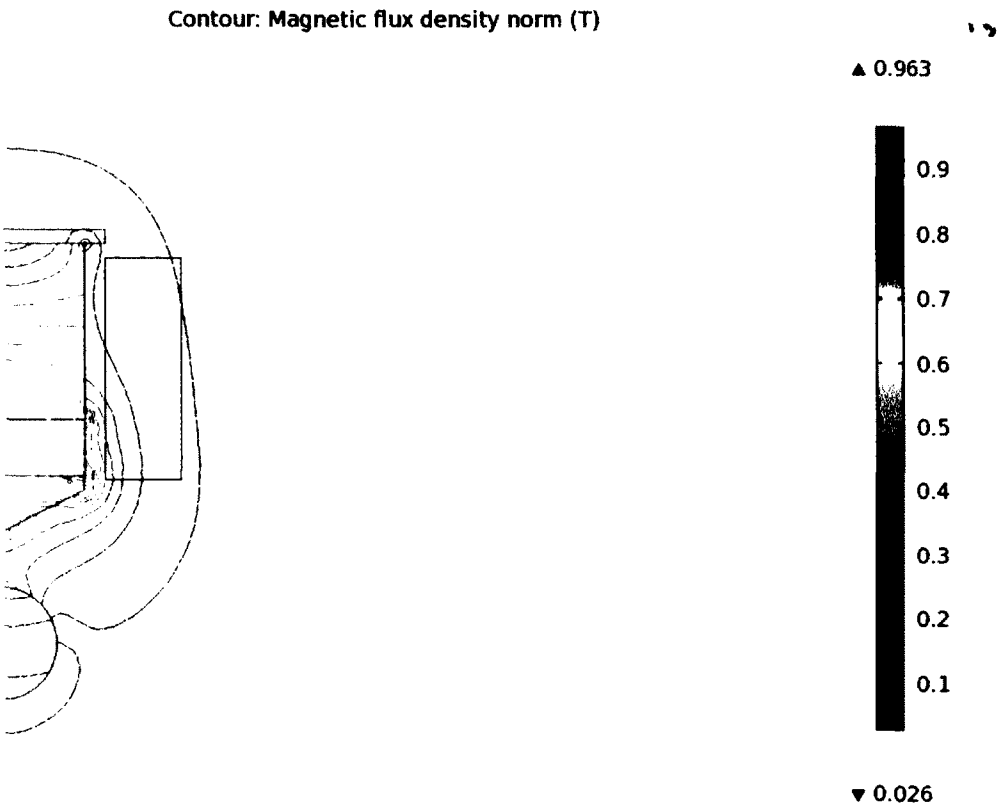

Figure 48: Magnetic flux density contours for the hybrid system

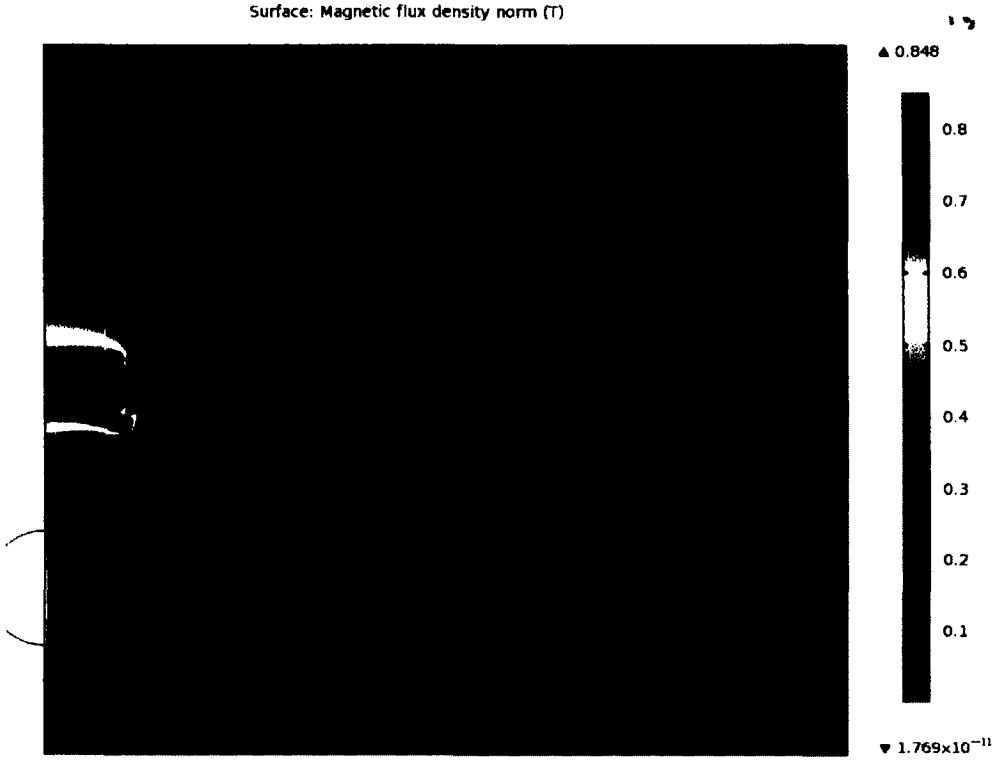

Figure 49: Magnetic flux density norms for the hybrid system

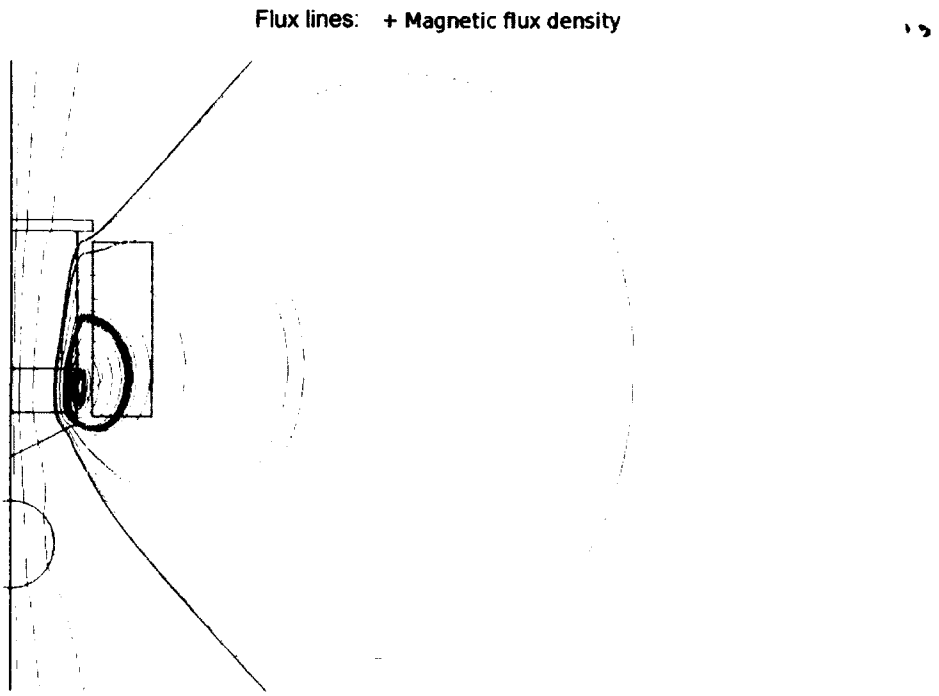

Figure 50: Magnetic flux lines for the hybrid system

Figures 48, 49 and 50 show that not all of the magnetic flux lines pass vertically through the center of the hybrid magnet tip because of the conical shape of the core tip. Accordingly, equation $(2-27)$ can be adjusted to account for the lost flux as follows:

$$B \approx \frac{\mu_0 N \eta_\phi \left(\frac{H_c l_p}{N} + I(t)\right)}{\left(\frac{\eta_g A_g \mu_0 l_p}{A_p \mu_p} + z(t)\right)} \qquad (4-2)$$

where η_ϕ represents the percentage of Φ_T that passes vertically through the hybrid magnet tip, and η_g represents the effective air gap cross-sectional area, i.e. the area that the magnetic flux passes through vertically.

Employing equation $(4-2)$ in equation $(2-28)$, the hybrid magnetic attraction force becomes:

$$F(I,z) = \mu_0 \eta_g A_g N^2 \left[\frac{\eta_\phi \left(\frac{H_c l_m}{N} + I(t)\right)}{\left(\frac{\eta_g A_g \mu_0 l_m}{A_m \mu_m} + z\right)}\right]^2 \qquad (4-3)$$

Now comparing the theoretical and the identified equations, the new parameters of equation $(4-3)$ become:

$$\eta_g = 0.28937$$

$$\eta_\phi = 0.07934$$

In other words, the system can be identified by determining only the values of these two parameters, and that would lead to a more accurate model; as a result of reducing the number of unknown parameters[15].

The identified parameters for the electrical circuit, in equation $(2-40)$, closely approximate the theoretical ones, since the lost flux does not affect the performance of the

electrical circuit; it is affected only by the total generated flux. Furthermore, the area in the inductance expression, equation$(2-40)$, represents the area through which the overall or total magnetic flux passes vertically, i.e. the magnet core cross-sectional area.

CHAPTER 5

LINEARIZATION AND CONTROL

5.1 INTRODUCTION

Modeling and identification are never goals by themselves, but they are tools to facilitate the study of real-life systems, e.g. analysis and control.

In this chapter, the single axis maglev model that was derived in Chapter 2, identified in Chapter 3 and validated in Chapter 4, is used to design a control system for the hybrid maglev ball experiment.

The design process was started by linearizing the model, investigating the dynamics of the system using the Routh stability criterion for three control strategies; and then, the feasible controller was applied to the nonlinear simulation and the hybrid maglev experiment.

5.2 MODEL LINEARIZATION

In the following, the single axis hybrid maglev model was linearized using a Taylor expansion about an equilibrium state, which was considered, in this study, to be the levitation gap.

5.2.1 Dynamic Model Linearization

A Taylor expansion for the dynamic model, represented by equation$(3-5)$, after dropping higher order terms yields:

$$\ddot{z} = -\left[z\frac{\delta F}{\delta z}|_{z_0,I_0} + I\frac{\delta F}{\delta I}|_{z_0,I_0}\right] - \frac{F_0}{m} + g \qquad (5-1)$$

$$F_0 = mg \qquad (5-2)$$

Here, F denotes the hybrid magnet attraction force, m the suspended object mass, z_0 the equilibrium position for the suspended object, and I_0 the excitation current at the

equilibrium height. The last two terms on the right-hand side of equation $(5-1)$ cancel at the equilibrium state.

Substituting equation $(3-5)$ into equation$(5-1)$, the coefficients for the gap (k_z) and the excitation current (k_I) on the linear dynamic model are as follows:

$$k_z = \frac{\delta F}{\delta z}|_{z_0,I_0} = -2K_f\frac{(I_0+I_p)^2}{(z_0+z_p)^3}$$
$$k_I = \frac{\delta F}{\delta I}|_{z_0,I_0} = 2K_f\frac{(I_0+I_p)}{(z_0+z_p)^2} \qquad (5-2)$$

where I_p represents the equivalent current for the permanent magnet, and z_p is the equivalent reluctance due to the presence of the permanent magnet.

Substituting equations $(5-2)$ into $(5-1)$ yields the linear dynamical model:

$$\ddot{z} = \frac{2K_f}{m}\frac{(I_0+I_p)^2}{(z_0+z_p)^3} * z - \frac{2K_f}{m}\frac{(I_0+I_p)}{(z_0+z_p)^2} * I \qquad (5-3)$$

5.2.2 Electrical Model Linearization

The electric current model, represented by equation $(3-17)$, is linearized using Taylor expansion as follows:

Solving equation $(3-17)$ for $\dot{I}$:

$$\dot{I} = \frac{IR}{K_I}(z+z_p) + \frac{(I+I_p)}{(z+z_p)} * \dot{z} + \frac{K_a}{K_I} * (I_c - I)(z+z_p) \qquad (5-4)$$

A Taylor expansion for equation $(5-4)$ about the equilibrium state, after dropping high order terms, yields:

$$\dot{I} = z\frac{\delta\dot{I}}{\delta z}|_{z_0,\dot{z}_0,I_0,I_{c_0}} + \dot{z}\frac{\delta\dot{I}}{\delta\dot{z}}|_{z_0,\dot{z}_0,I_0,I_{c_0}} + I\frac{\delta\dot{I}}{\delta I}|_{z_0,\dot{z}_0,I_0,I_{c_0}} + I_c\frac{\delta\dot{I}}{\delta I_c}|_{z_0,\dot{z}_0,I_0,I_{c_0}} + \dot{I}_0 \qquad (5-5)$$

By definition, all the time derivatives of the states are zero at the equilibrium. As a result:

$$\dot{I}_0 = 0 \tag{5-6}$$

The coefficients of the states in equation $(5-5)$ were found by calculating the first derivatives of equation $(5-4)$ with respect to the individual states evaluated in the equilibrium state, as follows:

$$\begin{gathered} k_{i_z} = \frac{\delta \dot{I}}{\delta z}|_{z_0,\dot{z}_0,I_0,I_{c_0}} = \frac{I_0 R}{K_l} - \frac{I_0 + I_p}{(z_0 + z_p)^2} * \dot{z}_0 + \frac{K_a}{K_l} * (I_{c_0} - I_0) \\ k_{i_{\dot{z}}} = \frac{\delta \dot{I}}{\delta \dot{z}}|_{z_0,\dot{z}_0,I_0,I_{c_0}} = \frac{(I_0 + I_p)}{(z_0 + z_p)} \\ k_{i_i} = \frac{\delta \dot{I}}{\delta I}|_{z_0,\dot{z}_0,I_0,I_{c_0}} = \frac{R}{K_l}(z_0 + z_p) + \frac{\dot{z}_0}{(z_0 + z_p)} - \frac{K_a}{K_l}(z_0 + z_p) \\ k_{i_{i_c}} = \frac{\delta \dot{I}}{\delta I_c}|_{z_0,\dot{z}_0,I_0,I_{c_0}} = \frac{K_a}{K_l}(z_0 + z_p) \end{gathered} \tag{5-7}$$

where $z_0, \dot{z}_0, I_0, I_{c_0}$ denote the equilibrium states for the single axis hybrid maglev model.

Thus, substituting equations $(5-6,7)$ into equation $(5-5)$ provides the linear model for the electrical model:

$$\dot{I} = k_{i_z} * z + k_{i_{\dot{z}}} * \dot{z} + k_{i_i} * I + k_{i_{i_c}} * I_c \tag{5-8}$$

5.2.3 State Space Representation and Transfer Function of The Linear Model

The state space representation of the linear model based on equations $(5-3,8)$ was represented as follows:

$$\begin{aligned} \dot{x} &= Ax + Bu \\ y &= Cx + Du \end{aligned} \tag{5-9}$$

where $\dot{x}$ represents the first time derivative of the states x, u is the system input and y denotes the system outputs. For the linear single axis hybrid maglev $\dot{x}$, x, u and y were chosen as follows:

$$\begin{aligned} \dot{x} &= \begin{bmatrix} \dot{z} \\ \ddot{z} \\ \dot{I} \end{bmatrix} \\ x &= \begin{bmatrix} z \\ \dot{z} \\ I \end{bmatrix} \\ u &= I_c \\ y &= z \end{aligned} \qquad (5-10)$$

The factoring matrices A, B, C and D for the linear model were thus:

$$\begin{aligned} A &= \begin{bmatrix} 0 & 1 & 0 \\ -\frac{k_z}{m} & 0 & -\frac{k_i}{m} \\ k_{i_z} & k_{i_{\dot{z}}} & k_{i_i} \end{bmatrix} \\ B &= \begin{bmatrix} 0 \\ 0 \\ k_{i_{i_c}} \end{bmatrix} \\ C &= [1 \quad 0 \quad 0] \\ D &= [0] \end{aligned} \qquad (5-11)$$

It is clear that the linear model depends upon the equilibrium states. At the equilibrium state or the steady state, the rate of change of all the state variables is zero and the only independent variable that determines the linear model is the equilibrium position of the suspended object (z_o). The steady state position was selected and the other steady state variables were accordingly calculated as follows:

- z_0, is constant (the chosen levitation gap).
- $\dot{z}_0 = 0$.
- Since $\ddot{z}_0 = 0$, then, substituting in equation $(5-3)$ yields:

$$I_0 = \sqrt{\frac{mg}{K_f}}(z_0 + z_p) - I_p \qquad (5-12)$$

- Since $\dot{I}_0 = 0$, then, substituting in equation $(5-4)$ yields:

$$I_{c_0} = I_0\left(\frac{K_a - R}{K_a}\right) \qquad (5-13)$$

Accordingly, the equilibrium constants can be calculated by substituting equations $(5-12,13)$ into equations $(5-2,7)$ as follows:

$$\begin{aligned}
k_z &= \frac{\delta F}{\delta z}|_{z_0,I_0} = -2K_f\frac{(I_0+I_p)^2}{(z_0+z_p)^3} \\
k_i &= \frac{\delta F}{\delta I}|_{z_0,I_0} = 2K_f\frac{(I_0+I_p)}{(z_0+z_p)^2} \\
k_{i_z} &= \frac{\delta \dot{I}}{\delta z}|_{z_0,\dot{z}_0,I_0,I_{c_0}} = \frac{I_0R}{K_l} + \frac{-RI_0}{K_l} = 0 \\
k_{i_{\dot{z}}} &= \frac{\delta \dot{I}}{\delta \dot{z}}|_{z_0,\dot{z}_0,I_0,I_{c_0}} = \frac{(I_0+I_p)}{(z_0+z_p)} \\
k_{i_i} &= \frac{\delta \dot{I}}{\delta I}|_{z_0,\dot{z}_0,I_0,I_{c_0}} = \left(\frac{R}{K_l} - \frac{K_a}{K_l}\right)(z_0+z_p) \\
k_{i_{i_c}} &= \frac{\delta \dot{I}}{\delta I_c}|_{z_0,\dot{z}_0,I_0,I_{c_0}} = \frac{K_a}{K_l}(z_0+z_p)
\end{aligned} \qquad (5-14)$$

Given the linear model and its state space representation, the transfer function can be represented as follows:

$$\frac{z}{I_c} = C(sI - A)^{-1}B + D \qquad (5-15)$$

Substituting equation $(5-11)$ into equation $(5-15)$ yields:

$$\frac{z}{I_c} = \frac{-\frac{k_i}{m} * k_{i_{i_c}}}{s^3 - k_{i_i} * s^2 + \left(\frac{k_i}{m} * k_{i_{\dot{z}}} + \frac{k_z}{m}\right) * s - k_{i_i} * \frac{k_z}{m}} \qquad (5-16)$$

Substituting equations $(5-14)$ into equation $(5-16)$ yields the single axis hybrid maglev transfer function:

$$\frac{z}{I_c} = \frac{-\frac{2K_f}{m}\frac{(I_0 + I_p)}{(z_0 + z_p)^2} * \frac{K_a}{K_l}(z_0 + z_p)}{s^3 + \left[\left(\frac{K_a}{K_l} - \frac{R}{K_l}\right)(z_0 + z_p)\right] * s^2 - \left[\left(\frac{K_a}{K_l} - \frac{R}{K_l}\right)(z_0 + z_p)\right] * \frac{2K_f}{m}\frac{(I_0 + I_p)^2}{(z_0 + z_p)^3}} \quad (5-17)$$

Table 2: Single axis hybrid maglev ball parameters		
Parameter	Description	Value
K_f	Magnetic force constant	$5.0678e-006\ H.m-turn^2$
K_l	Inductance constant	$0.0065\ H.m-turn^2$
K_a	Amplifier gain	11.7858
z_p	Permanent magnet equivalent reluctance	$0.0070\ m$
I_p	Permanent magnet equivalent current	$46.5894\ Amp$
R	Coil resistance	$1.1\ \Omega$
z_0	Selected equilibrium height	$0.0252\ m$

Applying the system parameter values provided in table (5-1) into the equilibrium constants expressions equations $(5-14)$ yields:

$$\begin{gathered} I_0 = 0.3975\ Amp \\ I_{c_0} = 0.3604\ Amp \\ k_z = -670.2484\ N/m \\ k_i = 0.4593\ N/Amp \\ k_{i_z} = 0.0000\ Amp/(m.s) \\ k_{i_z} = 1459.2211\ Amp/m \\ k_{i_i} = -52.9358\ 1/s \\ k_{i_{i_c}} = 58.3850\ 1/s \end{gathered} \quad (5-18)$$

Accordingly, the numerical state space representation and the transfer function for the linear single axis hybrid maglev model are:

$$A = \begin{bmatrix} 0 & 1 & 0 \\ 609.3168 & 0 & -0.4176 \\ 0.0000 & 1459.2211 & -52.9358 \end{bmatrix}$$

$$B = \begin{bmatrix} 0 \\ 0 \\ 58.3850 \end{bmatrix} \qquad (5-19)$$

$$C = [1 \quad 0 \quad 0]$$

$$D = [0]$$

$$\frac{z}{I_c} = \frac{-24.3794}{s^3 + 52.9358 * s^2 - 32254.6763} \qquad (5-20)$$

The dynamic behavior of the linear model of the single axis maglev system can be extracted by exploring the roots of characteristic polynomial, i.e. the denominator of equation $(2-20)$. However, it is more useful to represent the root locus of the linear model because that will provide more insight on the dynamic behavior of the system. The root locus of the linear model of the single axis maglev ball system is shown in Figure 51.

In previous studies, negative compensation was found to be a necessary condition for the stability of the single axis maglev ball using only electromagnet [13]. Therefore, the negative root locus of the system was generated and plotted in Figure 52.

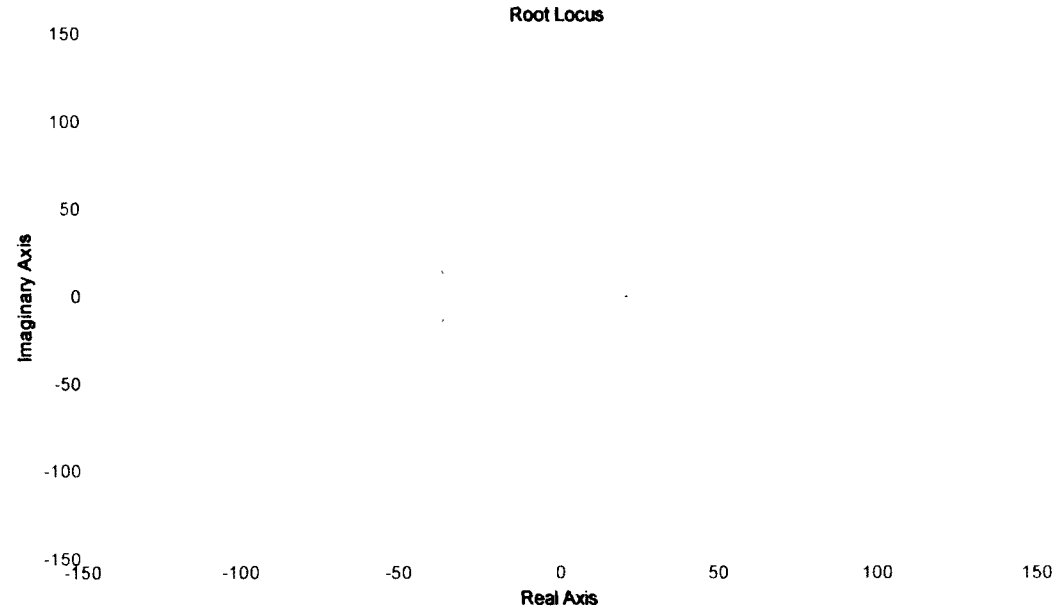

Figure 51: Positive root locus of the hybrid maglev open loop transfer function

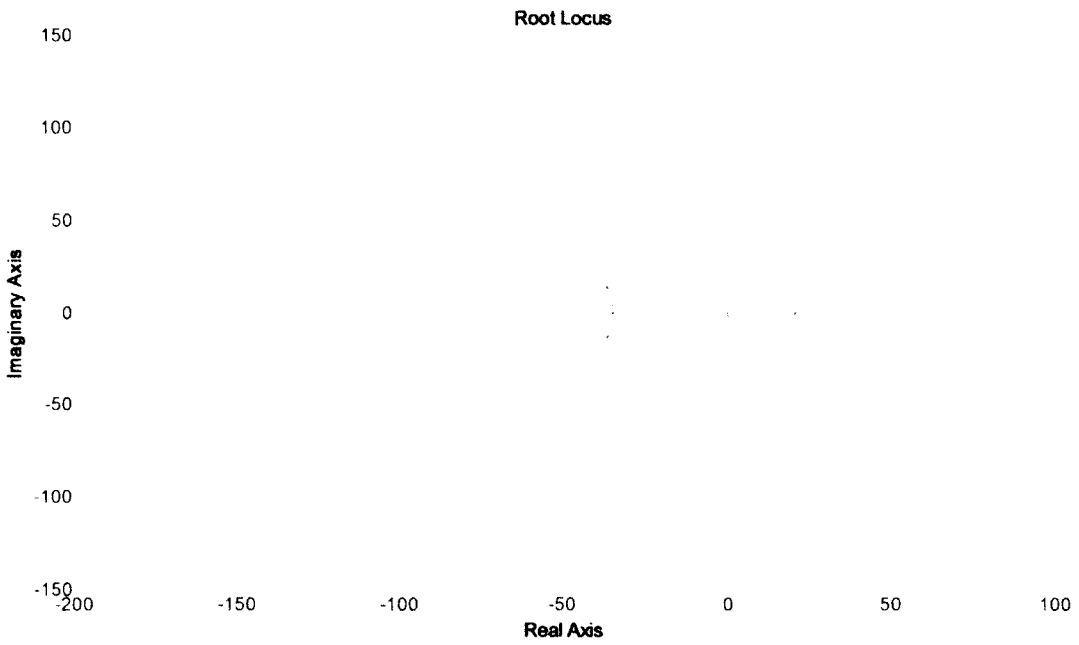

Figure 52: Negative root locus of the hybrid maglev open loop transfer function

Unlike the conventional single axis maglev system (using only electromagnets) [13] which has three real poles, Figures 51 and 52 show that the linear model of the single axis hybrid maglev ball experiment has one real unstable pole and two stable complex conjugate poles. The instability caused by the unstable pole will require feedback compensation to stabilize it since the migration path of the unstable pole always goes towards the right hand side of the s-plane.

5.3 SYSTEM CONTROL

5.3.1 PD Control

It was shown, previously in Chapter 3, that PD controllers can successfully stabilize the system. However, the PD controller was tuned experimentally. In this section, a PD controller was designed based on the linear model and following Routh stability analysis as follows:

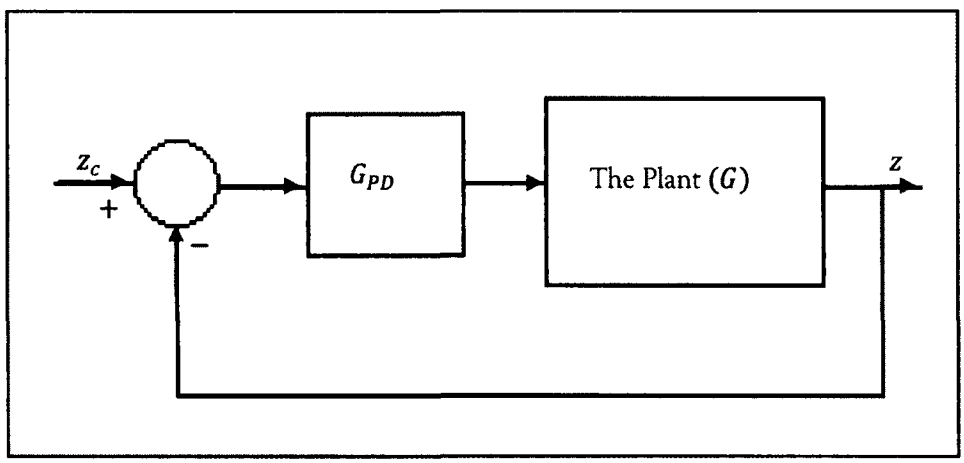

Figure 53: Block diagram of the closed loop plant with PD controller

The closed loop transfer function for a plant with a PD controller, shown in Figure 53, is:

$$\frac{z}{z_c} = \frac{G_{PD}G}{1 + G_{PD}G} \qquad (5-21)$$

where the transfer function of the PD controller is expressed as follows:

$$G_{PD} = K_p + K_d s \qquad (5-22)$$

Expanding and manipulating equation $(5-21)$ yields:

$$\frac{z}{z_c} = \frac{num(G_{PD}) * num(G)}{den(G_{PD}) * den(G) + num(G_{PD}) * num(G)} \qquad (5-23)$$

The closed loop for the linear single axis hybrid maglev ball with PD controller was found by substituting equations $(5-17,22)$ into equation $(5-23)$ as follows:

$$\frac{z}{z_c} = \frac{-(K_p + K_d s) * \frac{k_i}{m} * k_{i_c}}{s^3 - k_{i_i} * s^2 - K_d \frac{k_i}{m} * k_{i_c} s - \left(k_{i_i} * \frac{k_z}{m} + K_p \frac{k_i}{m} * k_{i_c}\right)} \qquad (5-24)$$

Now, applying the Routh stability criterion [16] on the closed loop transfer function expressed by equation $(5-24)$:

$$\begin{array}{ll} s^3 & 1 \qquad\qquad -K_d \frac{k_i}{m} * k_{i_c} \\ s^2 & -k_{i_i} \qquad\qquad -\left(k_{i_i} * \frac{k_z}{m} + K_p \frac{k_i}{m} * k_{i_c}\right) \\ s^1 & \frac{k_{i_i} * K_d \frac{k_i}{m} * k_{i_c} + \left(k_{i_i} * \frac{k_z}{m} + K_p \frac{k_i}{m} * k_{i_c}\right)}{-k_{i_i}} \\ s^0 & -\left(k_{i_i} * \frac{k_z}{m} + K_p \frac{k_i}{m} * k_{i_c}\right) \end{array} \qquad (5-25)$$

For the stability of the system, the following conditions should be satisfied [16]:

$$\begin{gathered} k_{i_i} < 0 \\ K_d < 0 \\ K_p < -\frac{k_{i_i} k_z}{k_i k_{i_c}} \\ K_p > -k_{i_i}\left(K_d + \frac{k_z}{k_i * k_{i_c}}\right) \end{gathered} \qquad (5-26)$$

The first condition in equation $(5-26)$ is already satisfied as equation $(5-18)$ showed. The second condition requires that the derivative gain always be negative to maintain stability. The third and the fourth conditions of equation $(2-26)$ provide the

upper and lower bounds for the proportional gain. Applying equation $(5-18)$ into the two last conditions in equation $(5-26)$ yields:

$$K_p < -\frac{-52.9358 * -670.2484}{0.4593 * 58.3850} < -1323.08$$
$$K_p > 52.9358\left(K_d + \frac{-670.2484}{0.4593 * 58.3850}\right) > 52.9358 * (K_d - 24.9941) \qquad (5-27)$$

A PD controller that satisfies equations $(2-26,27)$ was designed and applied to the linear single axis hybrid maglev model, as shown in the block diagram in Figure 53.

The root locus for the linear system with the controller-equation $(5-24)$ is shown in Figure 54. The step response of the closed loop system with the PD controller was generated as shown in Figure 55.

$$G_{PD_1} = -1800 - 51\,s \qquad (5-28)$$

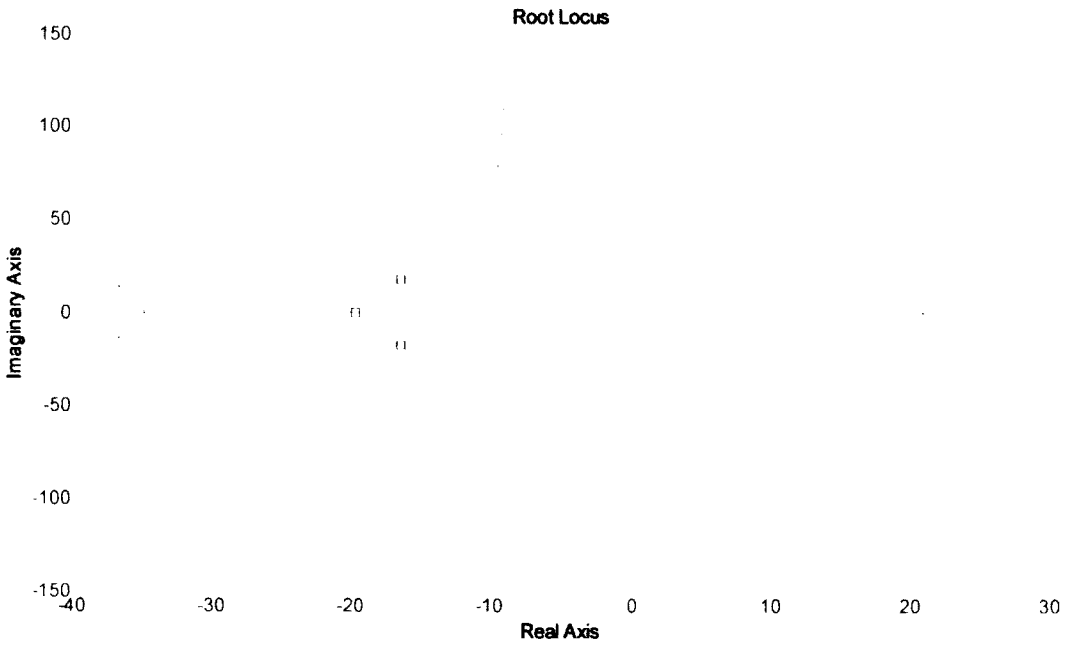

Figure 54: Closed loop system with the designed PD controller root locus

The square symbols in Figure 54 show the positions of the roots of the closed loop system with the designed PD controller. The complex conjugate mode produced a second order response since they had nonzero imaginary components; however, their position in the s-plane produced a well damped mode. All the closed loop system roots were far from the origin which produced a steady state error. Both the steady state error and the overshoot could be reduced by reducing the proportional gain, as clearly shown by the migration path of the augmented closed loop root locus. However, doing so will slow down the response of the closed loop system.

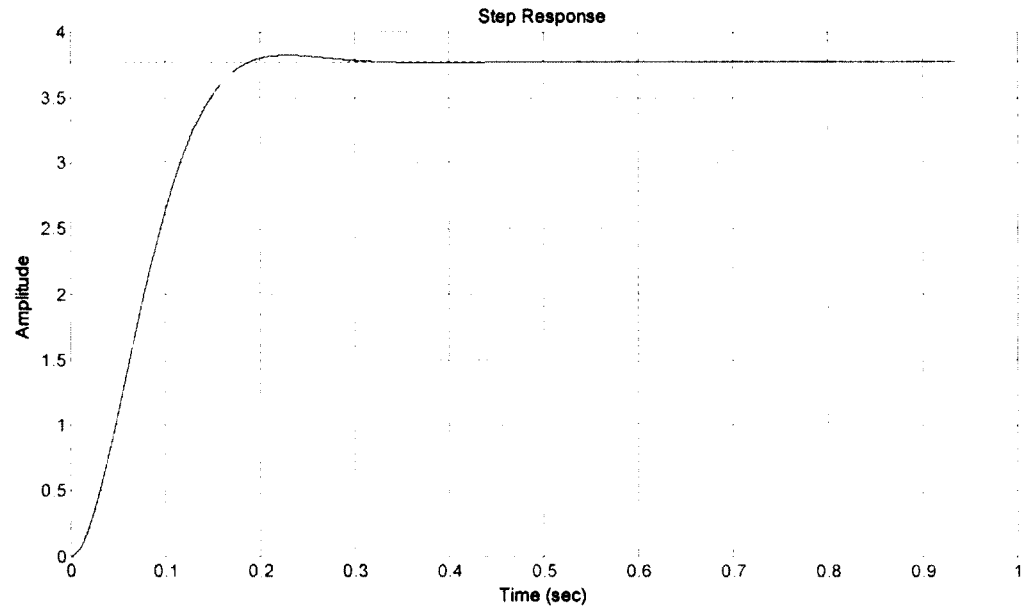

Figure 55: Step response of the closed loop system with the designed PD controller

Figure 55 shows that the PD control of the system produced a very significant steady-state error providing using a unit step input.

It was worthwhile to compare the root locus and the step response of the closed loop linearized system with the experimentally tuned PD controller that was used in the

identification process. The transfer function of the PD controller is given by equation $(5-29)$ below. The root locus and the step response of the closed loop system are shown in Figures 56 and 57.

$$G_{PD_2} = -2500 - 51\,s \qquad (5-29)$$

Notice that the experimentally tuned PD controller, equation $(5-29)$ satisfies conditions $(5-26,27)$ for the system stability.

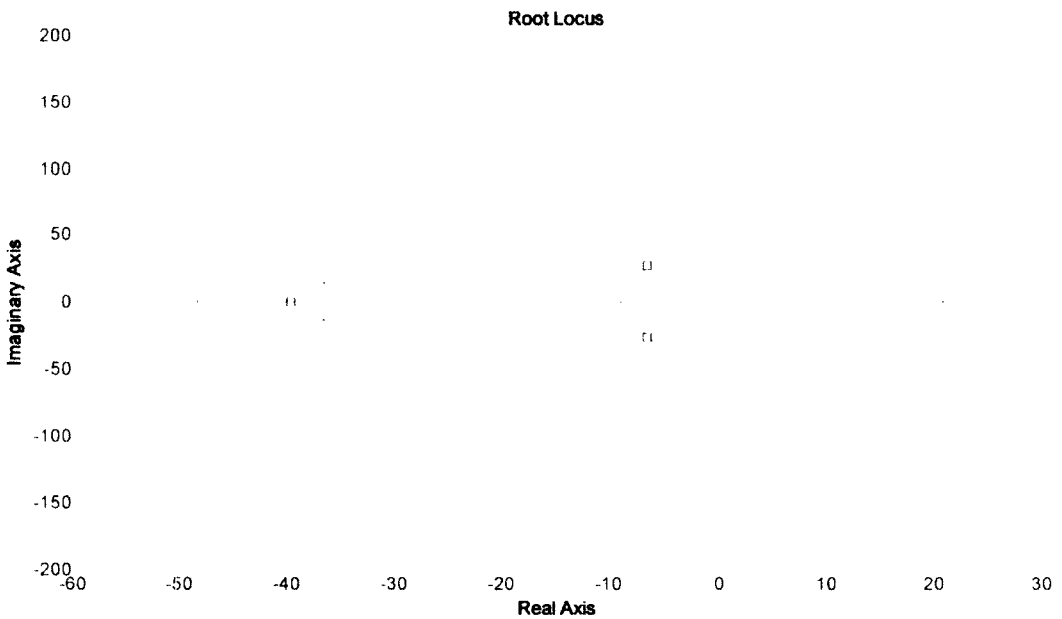

Figure 56: Closed loop system with the experimentally tuned PD controller root locus

The complex conjugate roots were closer to the origin than they were in Figure 54 which led to a smaller steady-state error. However, the damping ratio for this mode decreased which will increase overshoot.

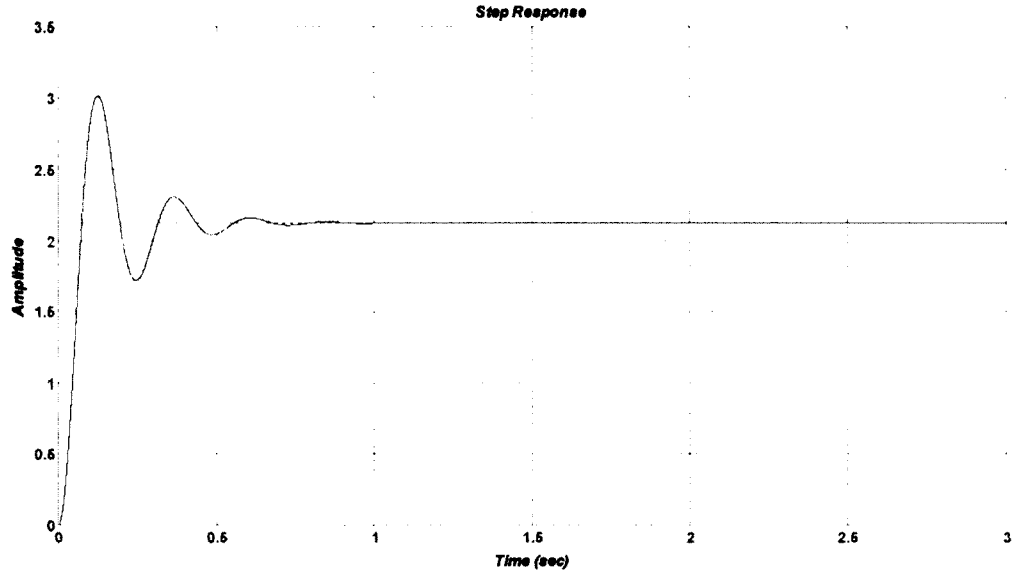

Figure 57: Step response of the closed loop system with the experimentally tuned PD controller

Comparing the step responses of the two PD controllers in Figure 58, it can be seen that the experimentally tuned controller produces relatively faster response with less steady-state error for the step response than the designed PD controller. However, some oscillations with relatively high overshoot appeared. In both cases the steady state error is undesirable.

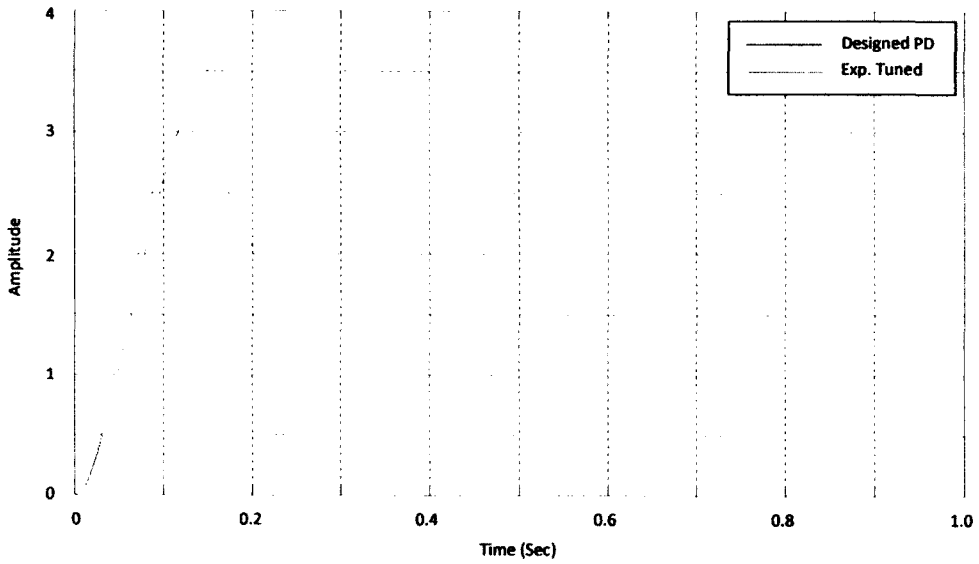

Figure 58: Designed PD vs. experimentally tuned PD closed loop step response

5.3.2 PID Control

It is well known that PID controllers reduce or eliminate steady-state error. As a result, a PID controller was designed for the system to eliminate the steady state error which occurs when using PD control. As was done before, the Routh stability criterion was followed to design the PID controller as follows:

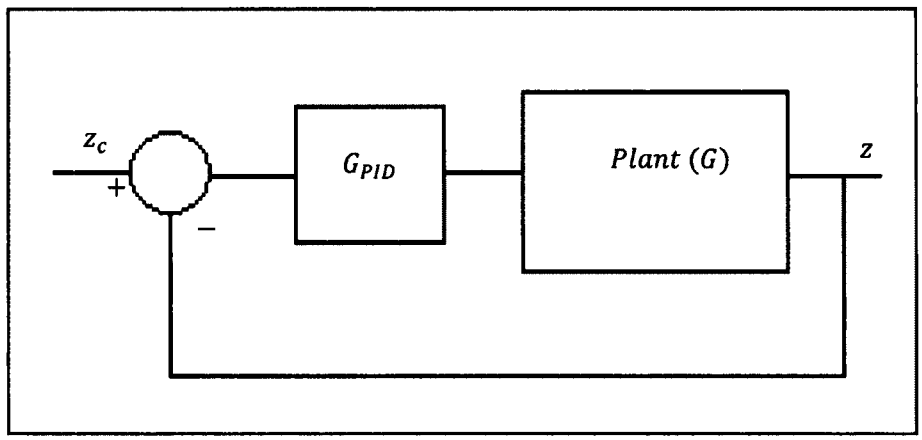

Figure 59: Block diagram of the closed loop plant with PID controller

The PID controller transfer function was written as follows:

$$G_{PID} = K_p + K_d s + \frac{K_I}{s} \qquad (5-29)$$

Applying the PID controller to the system and closing the loop as shown in Figure 59 resulted in the closed loop transfer function:

$$\frac{z}{z_c} = \frac{num(G_{PID}) * num(G)}{den(G_{PID}) * den(G) + num(G_{PID}) * num(G)} \qquad (5-30)$$

The closed loop for the linear single axis hybrid maglev ball with PID controller was found by substituting equations $(5-17,22)$ into equation $(5-30)$ as follows:

$$\frac{z}{z_c} = \frac{-\left(K_p s + K_d s^2 + K_I\right) * \frac{k_i}{m} * k_{i_{i_c}}}{s^4 - k_{i_i} * s^3 - K_d \frac{k_i}{m} * k_{i_{i_c}} s^2 - \left(k_{i_i} * \frac{k_z}{m} + K_p \frac{k_i}{m} * k_{i_{i_c}}\right) * s - K_I * \frac{k_i}{m} * k_{i_{i_c}}} \tag{5-31}$$

Now, applying the Routh stability criterion [16] on the closed loop transfer function:

$$\begin{array}{lll}
s^4 & 1 & -K_d \frac{k_i}{m} * k_{i_{i_c}} \qquad -K_I * \frac{k_i}{m} * k_{i_{i_c}} \\
s^3 & -k_{i_i} & -\left(k_{i_i} * \frac{k_z}{m} + K_p \frac{k_i}{m} * k_{i_{i_c}}\right) \\
s^2 & \frac{k_{i_i} * K_d \frac{k_i}{m} * k_{i_{i_c}} + \left(k_{i_i} * \frac{k_z}{m} + K_p \frac{k_i}{m} * k_{i_{i_c}}\right)}{-k_{i_i}} & -K_I * \frac{k_i}{m} * k_{i_{i_c}} \\
s^1 & -\left(k_{i_i} * \frac{k_z}{m} + K_p \frac{k_i}{m} * k_{i_{i_c}}\right) + \frac{-k_{i_i}^2 * K_I * \frac{k_i}{m} * k_{i_{i_c}}}{k_{i_i} * K_d \frac{k_i}{m} * k_{i_{i_c}} + \left(k_{i_i} * \frac{k_z}{m} + K_p \frac{k_i}{m} * k_{i_{i_c}}\right)} & \\
s^0 & -K_I * \frac{k_i}{m} * k_{i_{i_c}} &
\end{array} \tag{5-32}$$

For stability, the following condition should be satisfied:

$$\begin{gathered}
k_{i_i} < 0 \\
K_d \frac{k_i}{m} * k_{i_{i_c}} < 0 \\
K_I * \frac{k_i}{m} * k_{i_{i_c}} < 0 \\
K_p < \frac{-k_{i_i} * k_z}{k_{i_{i_c}} * k_i} \\
K_I < \frac{m\left[k_{i_i} * K_d \frac{k_i}{m} * k_{i_{i_c}} + \left(k_{i_i} * \frac{k_z}{m} + K_p \frac{k_i}{m} * k_{i_{i_c}}\right)\right]\left(k_{i_i} * \frac{k_z}{m} + K_p \frac{k_i}{m} * k_{i_{i_c}}\right)}{k_i k_{i_{i_c}} k_{i_i}^2}
\end{gathered} \tag{5-33}$$

The first condition in equation $(5-33)$ is already satisfied, the second two conditions show that the differential and integral gains should have negative values in order to maintain the stability of the system. The fourth condition yields:

$$K_p < -\frac{-52.9358 * -670.2484}{0.4593 * 58.3850} < -1323.08 \qquad (5-34)$$

And the last condition in equation $(5-33)$ provides the relationship between the PID controller gains as follows:

$$K_I < \frac{[-52.9358 * K_d + K_p + 1323.08](1323.08 + K_p)}{114.946} \qquad (5-35)$$

A PID controller-equation $(5-36)$ was designed for the system according to the conditions shown in equations $(5-33,34,35)$. Hence, the closed loop root locus for the system with the controller is shown in Figure 60.

The step response of the closed loop system with the PID controller is shown in Figure 61, the input was a unit step.

$$G_{PID} = \frac{-51.59\,s^2 - 1920\,s - 2750}{s} \qquad (5-36)$$

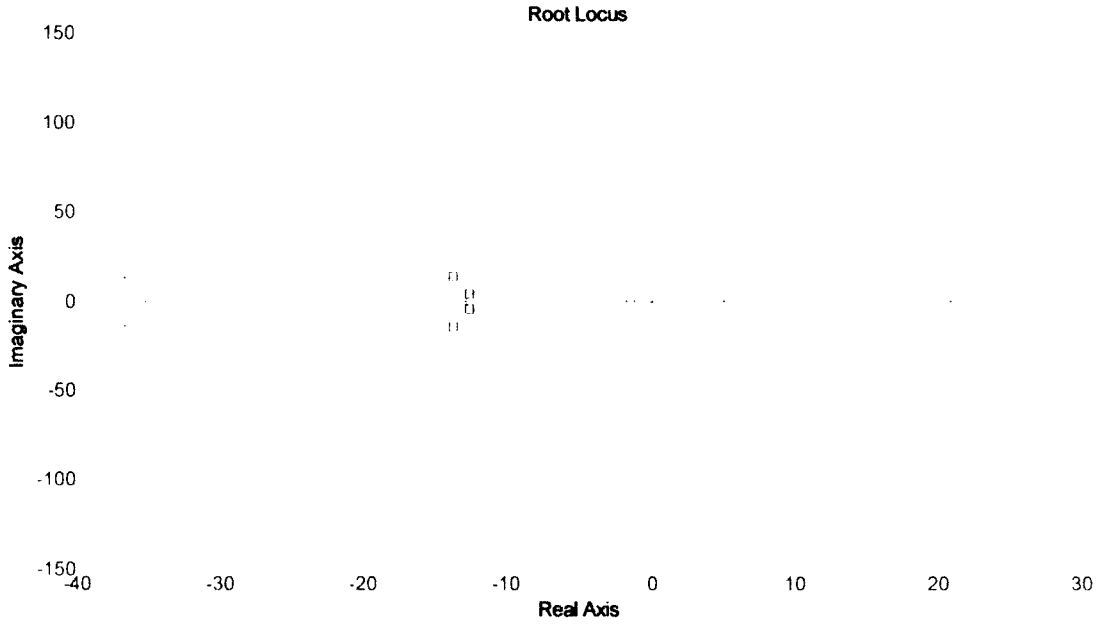

Figure 60: Closed loop system with the designed PID controller root locus

Although Figure 60 shows that the application of the PID controller produced a well augmented closed loop root locus for the system, PID controllers in general may lead to a significant overshoot [16].

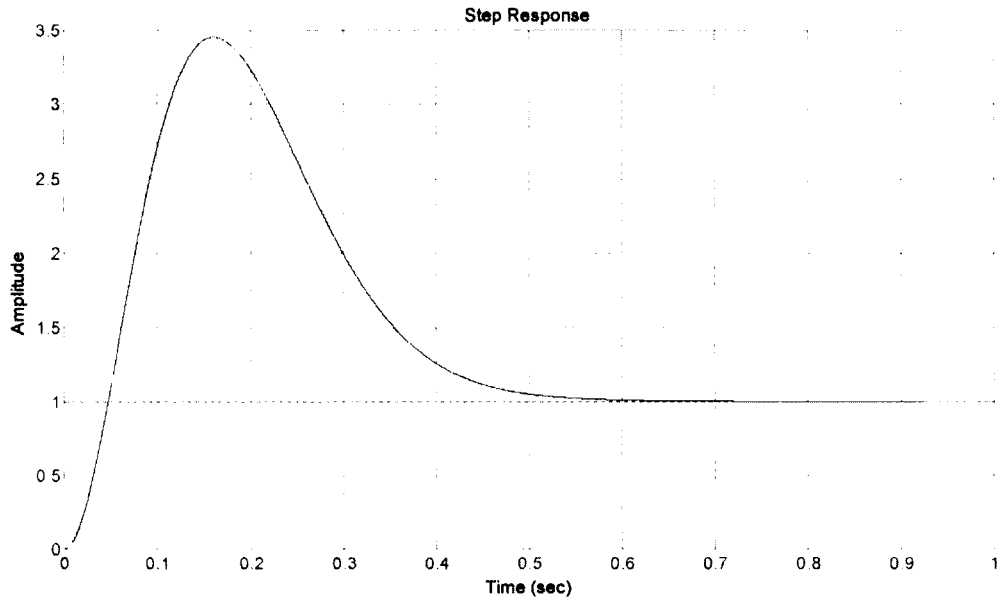

Figure 61: Step response of the closed loop system with the designed PID controller

Figure 61 shows that the application of PID controller to the system caused a significant overshoot, which is undesirable for this application.

5.3.3 PID with Pre-Filter

In order to reduce the overshoot associated with using a PID controller for the single axis hybrid maglev, the pre-filter technique was applied. However, there are other techniques to reduce overshoot associated with using PID, such as the anti-wind-up technique which is frequently used when there is saturation in some part of the system.

The advantages of using the pre-filter technique are that it does not affect the stability of the system and it does not modify the root locus of the system with the compensator. The closed loop system block diagram is shown in Figure 62.

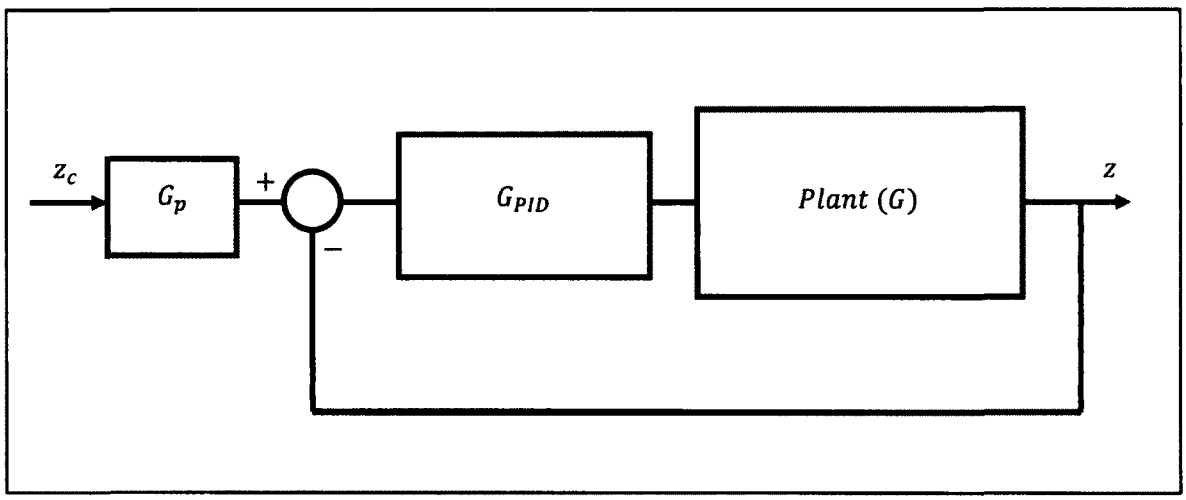

Figure 62: Block diagram of the closed loop plant with PID controller and Pre-filter

The open loop transfer function for the pre-filter and the closed loop system with the compensator was represented:

$$G_{cl} = G_{pf} * G_{cl_{PID}} \qquad (5-37)$$

The designed PID controller has the transfer function represented by equation $(5-38)$. The lag pre-filter used to alleviate the overshoot has the transfer function represented by equation $(5-39)$.

$$G_{PID} = \frac{-48.6\,s\text{^}2 - 1849\,s - 1800}{s} \qquad (5-38)$$

$$G_{pf} = \frac{0.17\,s + 1}{s + 1} \qquad (5-39)$$

The root locus of the closed loop system with the PID, equation $(5-38)$, is shown in Figure 63. And the step response of the modified closed loop system with PID and the pre-filter is shown in Figure 64.

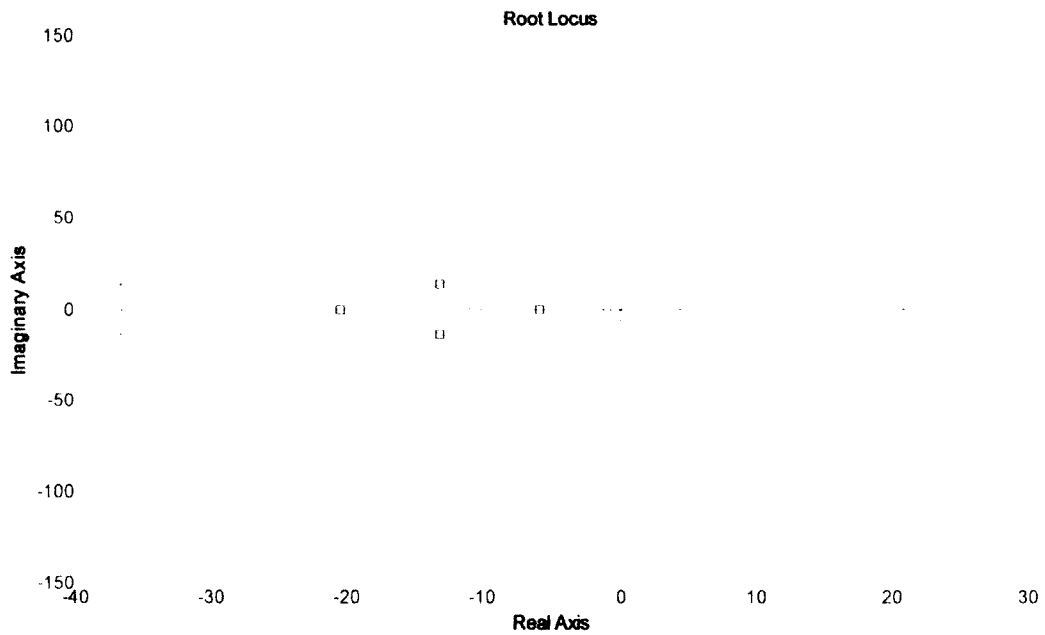

Figure 63: Closed loop system with the designed PID controller root locus

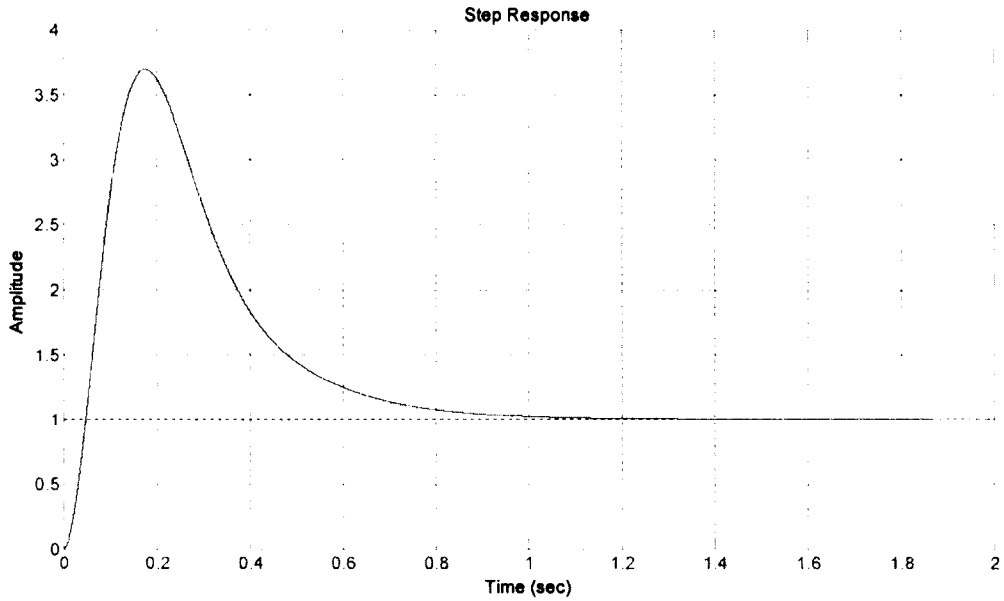

Figure 64: Step response of the closed loop system with the designed PID controller

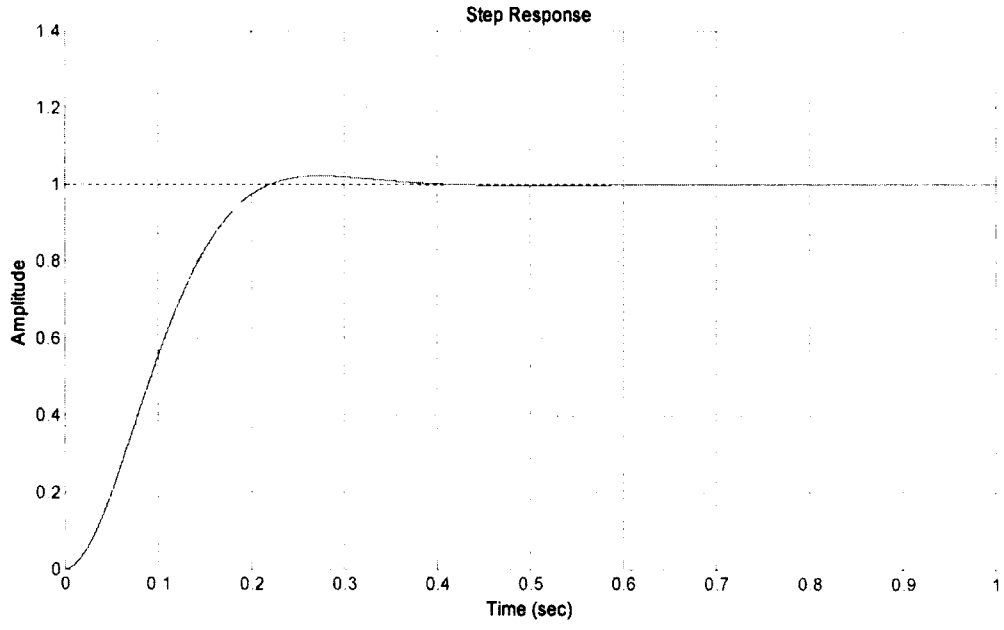

Figure 65: Step response of the closed loop system with the designed PID controller and the pre-filter

It is clearly seen in Figures 64 and 65 that the presence of the pre-filter has decreased overshoot substantially and produced an acceptable step response.

Applying the PID compensator with the pre-filter to both the nonlinear simulation and the experiment produced the time response shown in Figures 66 and 67.

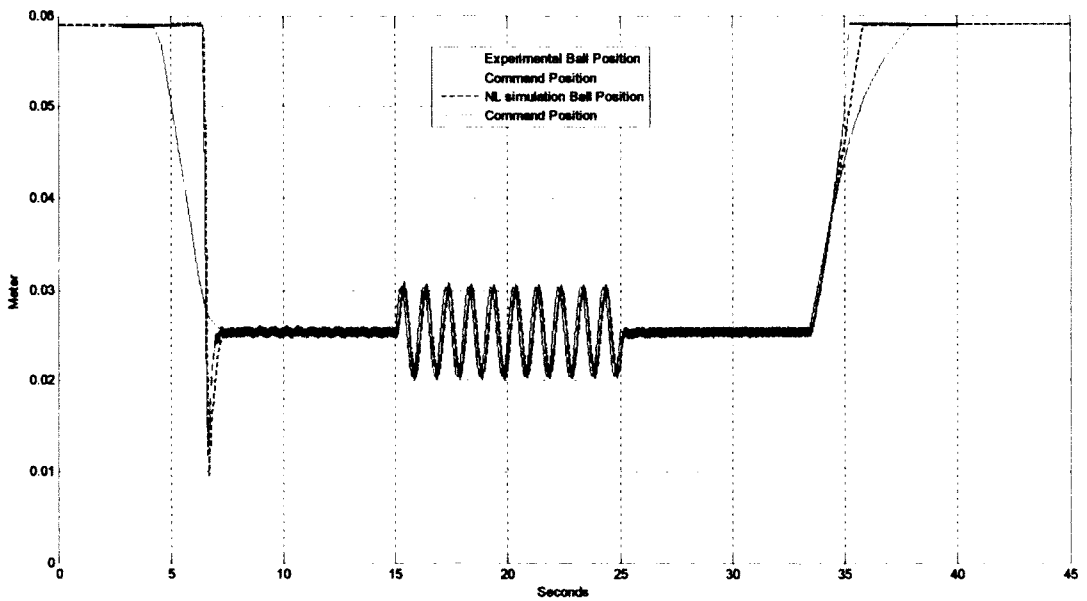

Figure 66: Hybrid maglev ball response using the designed PID and the pre-filter

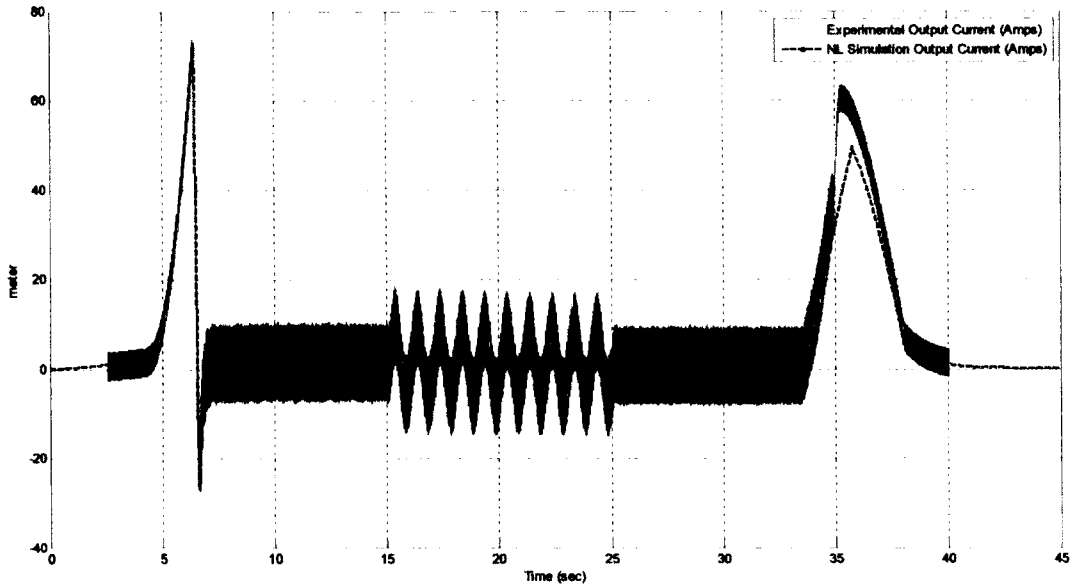

Figure 67: Hybrid maglev ball output current using the designed PID and the pre-filter

The spike that occurred in the time response, as shown in Figures 66 and 67, was due to the large force required to lift the ball from the stand, which was quite a distance away relative to the command gap. In order to avoid this, the integrator was turned off at the beginning of the levitation and the damping was increased. When the suspended object is close to the command gap the integrator turns on and the additional damping decreases gradually until it becomes fully operated by the designed PID controller near the desired gap. With these modifications, the nonlinear simulation and the experiment produced the time responses shown in Figures 68, 69 and 70.

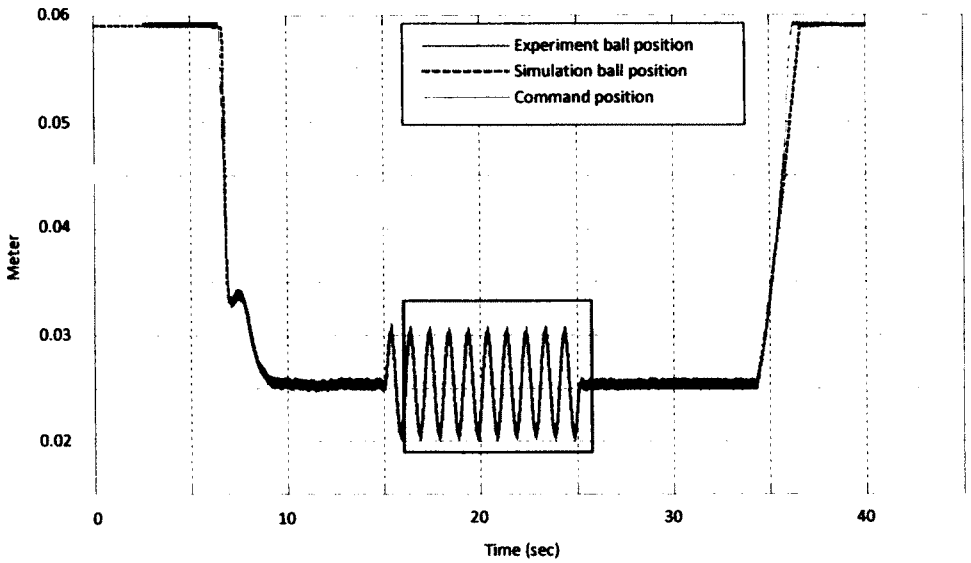

Figure 68: Modified hybrid maglev ball response using the designed PID and the pre-filter

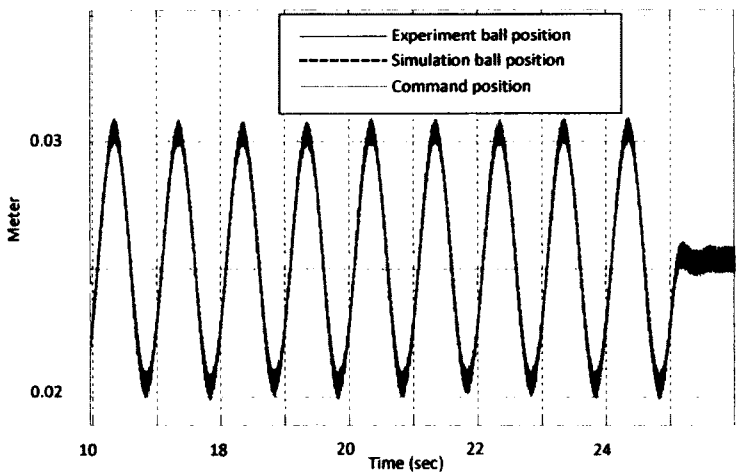

Figure 69: Modified hybrid maglev ball response using the designed PID and the pre-filter zoomed at the box shown in Figure 68

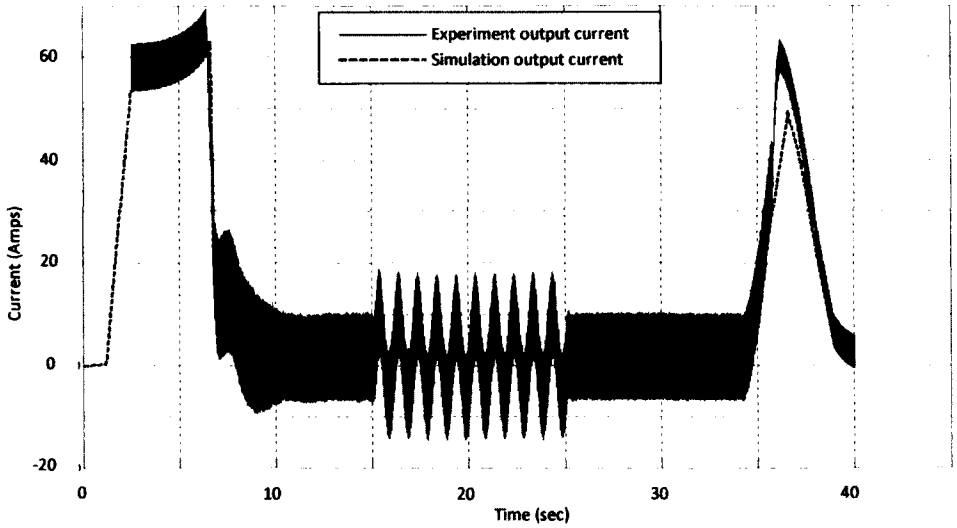

Figure 70: Modified hybrid maglev ball output current using the designed PID and the pre-filter

Figures 68, 69 and 70 show that the system follows the command without a significant steady state error or overshoot in the command gap. A slight offset occurs in the levitation due to the absence of the integrator. However, it is small and far from the command gap. In addition, Figures 68, 69 and 70 support the validity of the derived model and the nonlinear simulation.

CHAPTER 6

CONCLUSIONS AND RECOMMENDATIONS

6.1 INTRODUCTION

In this chapter, conclusions that can be extracted from this thesis are discussed, and some recommendations are stated in terms of what research can be done as a continuation of this work concerning the dynamics of hybrid maglev systems.

6.2 CONCLUSIONS

A dynamic model for a single axis hybrid maglev ball system was developed. This model was derived starting from first principles for electromagnetism. Detailed derivation steps were provided following a systematic and simple approach. The derived model was found to be very similar to the dynamic model for the conventional single axis maglev system, assuming that the permanent magnet was basically an electromagnet with constant current and correcting the air gap reluctance to account for the magnetic reluctance of the permanent magnet.

The theoretically derived equations were then identified to model a single axis hybrid maglev ball experiment. This identification was developed following the parametric identification method to fit the derived theoretical model for a single axis hybrid maglev ball experiment utilizing actual measurements. The Linear Least Square method was followed to estimate the unknown parameters.

Rigorous validity tests were executed for the identified model. A numerical nonlinear simulation was built for the experiment using the MatLab ® simulation platform, Simulink ®. Some test cases were performed for the nonlinear simulation and then compared with the corresponding real-time experimental outputs. This comparison showed that the simulation closely describes the actual system, and as a result, it can be concluded that the derived and identified model is valid.

The deviation of the theoretical model from the actual system was investigated with the aid of Comsol Multiphysics® software. Based on the investigation results, two new parameters were introduced to correct the theoretical model to fit the actual system. Those parameters were analogous to physical process efficiency; the first one represented the efficiency of magnetic flux linkage, and the second denoted the effective air gap cross sectional area. Accordingly, it can be concluded that the system can be identified by estimating the values of those two parameters in order to increase the accuracy of the identified model.

The identified model for the single axis hybrid maglev ball experiment was linearized using Taylor series expansions about a so-called equilibrium gap. The equilibrium gap was selected as the position where the permanent magnet could maintain the suspended object independently, i.e. the zero excitation current levitation. With the linearized model, the state space representation and the transfer function of the experiment were developed. The root locus (Evan's) plots for the linearized model were then employed to analyze the dynamics of the study system, and it was found that the system had a pole on the right side of the complex plane. It can be concluded from these results that the single axis hybrid maglev system is similar to the conventional single axis maglev system since it was highly unstable.

Simple PD, PID and PID with pre-filter controllers were designed for the system, based on the linearized model. The Routh stability criterion was applied for the linearized model with three control scenarios, PD, PID and PID with pre-filtering in order to specify the controller gains that assured system stability. This result showed that all the candidate controllers can stabilize the system. The dynamic expression of the hybrid maglev system is equivalent to the dynamic expression of the conventional system with modified equivalent current and gap. This observation leads to the conclusion that the same controllers that stabilize conventional maglev systems can stabilize hybrid maglev systems. The symbolic expressions for the gains that bound the region of stability are equivalent with (I) and (z) replaced by (I_{eq}) and (z_{eq}). The step response of the linearized model with the designed controllers was explored to determine their viability to the single axis hybrid maglev ball

system. The most suitable controller was then applied to the nonlinear simulation and the actual system. Accordingly, comparing the resulting responses from the simulation and the real time experiment supported the validity of the derived model and the viability of PID controller with pre-filtering for this application. This result leads to the conclusion that the single axis hybrid maglev ball system can be stabilized and accurately achieves the required gap by a simple PID controller with the aid of the pre-filtering technique.

6.3 RECOMMENDATIONS

This research was conducted for a single axis (or one degree of freedom) hybrid maglev system. And it is recommended to extend the study to two degrees of freedom systems i.e. incorporating for lateral motion.

Based on the results of the deviation of theoretical model, it is recommended to perform further analysis using Comsol Multiphysics® for the hybrid magnet used in the experiment to determine a suitable core tip geometry. The desired geometry must maintain the lateral stability and reduce lost magnetic flux. This will consequently lead to lower power consumption.

The effect of the pedestal force was found to have a significant impact on the dynamical behavior of the suspended object. Therefore, the design of the control system for electromagnetic suspension application becomes more challenging when encountering the pedestal force. The reason for that challenge is that this force was not included in the theoretical dynamic model for electromagnetic suspension systems; however, it was modeled as spring-damper forces acting upon the suspended object at the pedestal. Accordingly, it is recommended to conduct further studies for this type of force to include it in the dynamic model for the maglev system in order to avoid unexpected dynamical behaviors in initiating levitation.

The hybrid magnet technique was shown to be feasible in terms of power consumption and dynamic behavior. Therefore, it is recommended that this type of magnet system be applied to the Old Dominion University Maglev vehicle and perform a complete study of the dynamics and control for the hybrid maglev technology on full scale

vehicles. This study is recommended to cover both theoretical and experimental aspects. Furthermore, it is recommended that flexible structures, flux feedback and lateral motion on full scale hybrid maglev vehicles be examined.

REFERENCES

1. Maxwell, J.C., *A Dynamical Theory of the Electromagnetic Field.* Philosophical Transactions of the Royal Society of London, 1865. 155 (ArticleType: research-article / Full publication date: 1865 /): p. 459-512.
2. Rong-Jong, W., L. Jeng-Dao, and L. Chiung-Chou. *Model-Free Control Design for Hybrid Magnetic Levitation System.* in *Fuzzy Systems, 2005. FUZZ '05. The 14th IEEE International Conference on.* 2005.
3. Sinha, P.K., *Electromagnetic Suspension: Dynamics & Control.* Vol. 30. 1987.
4. Zhang, X., H. Cheng, and Y. Li. *Identification of a hybrid maglev system with electromagnets and permanent magnets.* 2011: IEEE.
5. Chang-Hyun, K., et al. *Zero-power control of magnetic levitation vehicles with permanent magnets.* in *Control Automation and Systems (ICCAS), 2010 International Conference on.* 2010.
6. Atherton, D. and A. Eastham, *Limitations of levitation by iron-cored electromagnets.* Magnetics, IEEE Transactions on, 1974. 10(3): p. 410-412.
7. Liming, S. and Z. Haibo. *Feedback linearization control for a hybrid magnet levitation system.* in *Electrical Machines and Systems, 2008. ICEMS 2008. International Conference on.* 2008.
8. Morishita, M., et al., *A new MAGLEV system for magnetically levitated carrier system.* Vehicular Technology, IEEE Transactions on, 1989. 38(4): p. 230-236.
9. Richard Thornton, T.C., Brian Perrealt, Jim Wieler, Steve Levine, *An M3 Maglev System for Old Dominion University.* 2008.
10. Duckworth, H.E., *Electricity and Magnetism.* 1960: Macmillan.
11. Coren, R.L., *Basic engineering electromagnetics: an applied approach.* 1988: Prentice-Hall, Inc.
12. Thompson, M.T., *Practical Issues in the Use of NdFeB Permanent Magnets in Maglev, Motors, Bearings, and Eddy Current Brakes.* Proceedings of the IEEE, 2009. 97(11): p. 1758-1767.
13. Hanasoge, A., A. Omran, and T. Alberts, *Model Validation of a Magnetic Ball Levitation System.* ASME Conference Proceedings, 2008. 2008(43352): p. 17-23.
14. Atherton, D., *Maglev using permanent magnets.* Magnetics, IEEE Transactions on, 1980. 16(1): p. 146-148.
15. Bosch, P.v.d. and A.v.d. Klauw, *Modeling, Identification and Simulation of Dynamical Systems.* 1994.
16. Ogata, K., *Modern control engineering.* 2001: Prentice Hall PTR.
17. Livingston, J.D., *Rising force : the magic of magnetic levitation.* 2011, Cambridge, Mass.: Harvard University Press.

APPENDIX A

MATLAB ® CODE

```
%%%
```

```
di=subs(dpoly1A,x_data1'); %CURRENT TIME DERIVATIVE
z=y_data1'; %RAW EXPERIMENTAL SUSPENDED OBJECT POSITION
zth=subs(poly1Z,x_data1'); %CURVE FITTING GAP RESPONSE
dz=subs(dpoly1z,x_data1'); %SUSPENDED OBJECT VELOCITY
ddz=subs(ddpoly1z,x_data1'); %SUSPENDE OBJECT ACCELERATION

%%%
```

```
end
%VALIDATION FIGURES
figure (1)
%EQUATION OF MOTION VALIDATION
plot(x_data1,z,'k',x_data1,zver,'r')
legend('Experiment gap','Identification Gap')
xlabel('time (sec)')
ylabel('Gap (m)')

figure (2)
%ELECTRICAL CIRCUIT EQUATION VALIDATION
plot(x_data1,I,'k',x_data1,Iver,'r')
legend('Experiment Current Output','Identification Current Output')
xlabel('time (sec)')
ylabel('Current (Amp)')
```

APPENDIX B

STOKES' THEOREM

A generalization of the curl of a vector, as shown in the following equation, can be obtained by relaxing the limit that $dS \to 0$.

$$(curl\ of\ V)_z = \lim_{dS \to 0} \frac{\oint \boldsymbol{V}.\tau dl}{dS} = \left(\frac{\partial V_y}{\partial x} - \frac{\partial V_x}{\partial y}\right) \qquad (B-1)$$

Multiplying by dS yields:

$$\oint_{around\ dS} \boldsymbol{V}.\tau dl = (\boldsymbol{\nabla} \times \mathbf{V})_{\perp dS} dS = (\boldsymbol{\nabla} \times \mathbf{V}).\boldsymbol{n} dS \qquad (B-2)$$

Where $\boldsymbol{n}$ is the unit vector normal to the element of surface about which the contour integral is taken. Figure 70 has a large surface S bounded by the curve C and shows the element areas of which it is composed.

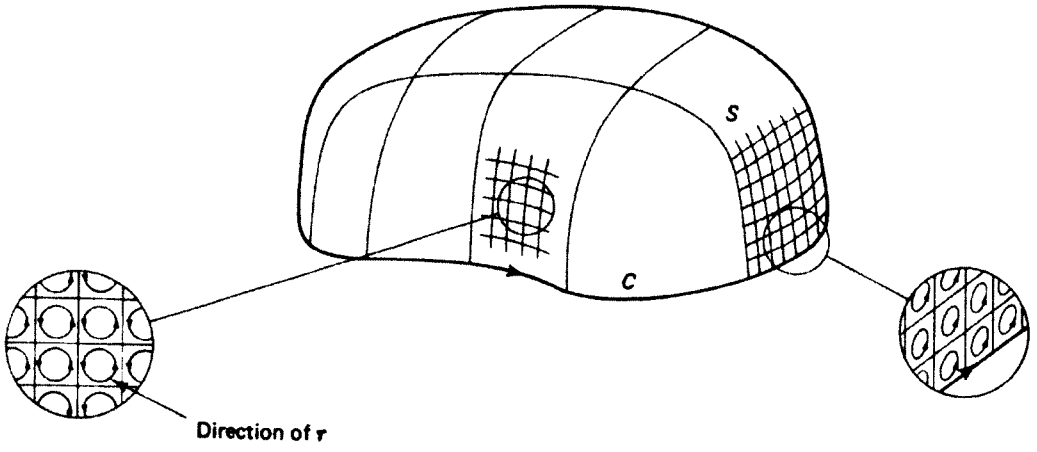

Figure 71: Stokes' theorem

Let us carry the contour integral on the left-hand side of equation $(B-2)$ about the perimeters of all these small areas and then add the results. The inserts to the figure show that the $\boldsymbol{\tau}$ are oppositely directed on the common sides of adjacent regions. As a result, the individual path integrals give opposite contributions on their common sides and cancel when they are added. The exceptions to this cancellation are on the perimeter curve, where the integrals are found on only one side. Therefore, after adding the integrals around all the infinitesimal areas, we are left with only the contributions on C, the perimeter of S. Also, adding the surface contributions on the right-hand side of equation $(B-2)$ yields the integral over the entire surface bounded by C. We then have

$$\oint \boldsymbol{V}.\boldsymbol{\tau} dl = (\boldsymbol{\nabla} \times \mathbf{V}).\boldsymbol{n} dS \qquad (B-3)$$

Where it is understood that the contour integral over the bounding curve C and the surface integral is over the entire surface bounded by C. It is important to realize that it has not been necessary to specify the surface S, which has the curve C as its boundary. Equation $(B-3)$ is remarkable in that surface S can be any surface terminated by C. equation $(B-3)$ is *Stokes' theorem*.

VITA

AHMED ELHUSSEIN ELTAYEB MEKKY

Contact No: +1-757-701-5806
Email: 7aseen@gmail.com

7731 Harrison RD, Apt 1
Norfolk, Virginia 23505, USA

SUMMARY OF QUALIFICATION AND TRAININGS

- B.Sc Honors-First Class-in Mechanical Engineering 2007, University Of Khartoum, Khartoum, Sudan.
- Enrolled in MSc program with Old Dominion University, Aerospace Department on 08-25-2010, Norfolk, VA, USA.
- Research/Teaching Assistant in the Department of Mechanical and Aerospace Engineering, Old Dominion University from August 2010 to present.
- Teaching assistant in the Faculty of Engineering, University of Khartoum-Mechanical Engineering department from July 2008 to present, Khartoum, Sudan.
- Worked as a teaching assistant in the following courses:
  (1) Mechanical Engineering Design I, II and III. (2) Engineering Drawing I and II.
  (3) Dynamics of Mechanical Systems (Vibrations). (4) Machine Elements.
  (5) Mechanical Engineering Laboratories I, II and III. (6) Applied Analog and Digital Control.
- Educational Preparation Course in the period between 03-30-09 to 05-07-09 with the Staff Development Centre, University of Khartoum, Khartoum, Sudan.
- Training period with Almohandis Workshop on Diesel Fuel Injection Systems repair and adjustment, Khartoum, Sudan.
- Training period from 01-12-08 to 03-12-08 with FOUR-tech maintenance Company on diesel generators maintenance and service, Khartoum, Sudan.
- Training period from 04-01-08 to 07-29-08 with RAM Energy, Contracts & Legal Section, Khartoum, Sudan.
- Worked with the National Electricity Corporation, Sudan as a generation engineer for the period between October-09 and August-11.

PRIZES AND AWARDS

- SHELL Co. Prize for the second best performance during the final year in the Mechanical Engineering Department, University of Khartoum for the academic year 2006-2007.
- Golden Key International Honor Society membership, 2011.

LANGUAGES

- Arabic, native language.
- English.

PUBLICATIONS

- Alberts T., Mekky A., "Modeling, Identification, Validation and Control of A Hybrid Maglev Ball", **Dynamic Systems and Control Conf., ASME,** 2012.

OTHER SKILLS

General computer use, Microsoft Office, AutoCAD, Solid-Works, MatLab, Simulink®, Comsol Multiphysics ® (beginner), Self-Learning.